

Jordan Journal of Mechanical and Industrial Engineering (JJMIE)

JJMIE is a high-quality scientific journal devoted to fields of Mechanical and Industrial Engineering. It is published by The Jordanian Ministry of Higher Education and Scientific Research in corporation with the Hashemite University.

EDITORIAL BOARD

Editor-in-Chief

Prof. Mousa S. Mohsen

Editorial board

Prof. Bilal A. Akash
Hashemite University

Prof. Adnan Z. Al-Kilany
University of Jordan

Prof. Ayman A. Al-Maaitah
Mutah University

Prof. Moh'd A. Al-Nimr
Jordan University of Science and Technology

Prof. Ali A. Badran
University of Jordan

Prof. Naseem M. Sawaqed
Mutah University

THE INTERNATIONAL ADVISORY BOARD

Abu-Qudais, Mohammad
Jordan University of Science & Technology, Jordan

Abu-Mulaweh, Hosni
Purdue University at Fort Wayne, USA

Afaneh Abdul-Hafiz
Robert Bosch Corporation, USA

Afonso, Maria Dina
Institute Superior Tecnico, Portugal

Badiru, Adedji B.
The University of Tennessee, USA

Bejan, Adrian
Duke University, USA

Chalhoub, Nabil G.
Wayne State University, USA

Cho, Kyu-Kab
Pusan National University, South Korea

Dincer, Ibrahim
University of Ontario Institute of Technology,
Canada

Douglas, Roy
Queen's University, U. K

El Bassam, Nasir
International Research Center for Renewable
Energy, Germany

Haik, Yousef
United Arab Emirates University, UAE

Jaber, Jamal
Al- Balqa Applied University, Jordan

Jubran, Bassam
Ryerson University, Canada

Kakac, Sadik
University of Miami, USA

Khalil, Essam-Eddin
Cairo University, Egypt

Mutoh, Yoshiharu
Nagaoka University of Technology, Japan

Pant, Durbin
Iowa State University, USA

Riffat, Saffa
The University of Nottingham, U. K

Saghir, Ziad
Ryerson University, Canada

Sarkar, MD. Abdur Rashid
Bangladesh University of Engineering &
Technology, Bangladesh

Signer, Dennis
Wichita State University, USA

Sopian, Kamaruzzaman
University Kebangsaan Malaysia, Malaysia

Tzou, Gow-Yi
Yung-Ta Institute of Technology and Commerce,
Taiwan

EDITORIAL BOARD SUPPORT TEAM

Language Editor

Dr. Zeinab Abu Samak

Publishing Layout

Eng. Sultan M. Amr

Editorial Secretary

Khuloud Al-Zyoud

SUBMISSION ADDRESS:

Prof. Mousa S. Mohsen, Editor-in-Chief
Jordan Journal of Mechanical & Industrial Engineering,
Hashemite University,
PO Box 330127, Zarqa, 13133 , Jordan

E-mail: jjmie@hu.edu.jo



Hashemite Kingdom of Jordan



Hashemite University

Jordan Journal of Mechanical and Industrial Engineering

JJMIE

An International Peer-Reviewed Scientific Journal

<http://jjmie.hu.edu.jo/>

ISSN 1995-6665

Jordan Journal of Mechanical and Industrial Engineering (JJMIE)

JJMIE is a high-quality scientific journal devoted to fields of Mechanical and Industrial Engineering. It is published by The Jordanian Ministry of Higher Education and Scientific Research in corporation with the Hashemite University.

Introduction: The Editorial Board is very committed to build the Journal as one of the leading international journals in mechanical and industrial engineering sciences in the next few years. With the support of the Ministry of Higher Education and Scientific Research and Jordanian Universities, it is expected that a heavy resource to be channeled into the Journal to establish its international reputation. The Journal's reputation will be enhanced from arrangements with several organizers of international conferences in publishing selected best papers of the conference proceedings.

Aims and Scope: Jordan Journal of Mechanical and Industrial Engineering (JJMIE) is a refereed international journal to be of interest and use to all those concerned with research in various fields of, or closely related to, mechanical and industrial engineering disciplines. Jordan Journal of Mechanical and Industrial Engineering aims to provide a highly readable and valuable addition to the literature which will serve as an indispensable reference tool for years to come. The coverage of the journal includes all new theoretical and experimental findings in the fields of mechanical and industrial engineering or any closely related fields. The journal also encourages the submission of critical review articles covering advances in recent research of such fields as well as technical notes.

Guide for Authors

Manuscript Submission

High-quality submissions to this new journal are welcome now and manuscripts may be either submitted online or mail.

Online: For online submission upload one copy of the full paper including graphics and all figures at the online submission site, accessed via E-mail: jjmie@hu.edu.jo. The manuscript must be written in MS Word Format. All correspondence, including notification of the Editor's decision and requests for revision, takes place by e-mail and via the Author's homepage, removing the need for a hard-copy paper trail.

By Mail: Manuscripts (1 original and 3 copies) accompanied by a covering letter may be sent to the Editor-in-Chief. However, a copy of the original manuscript, including original figures, and the electronic files should be sent to the Editor-in-Chief. Authors should also submit electronic files on disk (one disk for text material and a separate disk for graphics), retaining a backup copy for reference and safety.

Note that contributions may be either submitted online or sent by mail. Please do NOT submit via both routes. This will cause confusion and may lead to delay in article publication. Online submission is preferred.

Submission address and contact:

Prof. **Mousa S. Mohsen**, Editor-in-Chief
Jordan Journal of Mechanical & Industrial Engineering,
Hashemite University,
PO Box 330127, Zarqa, 13133 , Jordan
E-mail: jjmie@hu.edu.jo

Types of contributions: Original research papers

Corresponding author: Clearly indicate who is responsible for correspondence at all stages of refereeing and publication, including post-publication. Ensure that telephone and fax numbers (with country and area code) are provided in addition to the e-mail address and the complete postal address. Full postal addresses must be given for all co-authors.

Original material: Submission of an article implies that the work described has not been published previously (except in the form of an abstract or as part of a published lecture or academic thesis), that it is not under consideration for publication elsewhere, that its publication is approved by all authors and that, if accepted, it will not be published elsewhere in the same form, in English or in any other language, without the written consent of the Publisher. Authors found to be deliberately contravening the submission guidelines on originality and exclusivity shall not be considered for future publication in this journal.

Supplying Final Accepted Text on Disk: If online submission is not possible: Once the paper has been accepted by the editor, an electronic version of the text should be submitted together with the final hardcopy of the manuscript. The electronic version must match the hardcopy exactly. We accept MS Word format only. Always keep a backup copy of the electronic file for reference and safety. Label the disk with your name. Electronic files can be stored on CD.

Notification: Authors will be notified of the acceptance of their paper by the editor. The Publisher will also send a notification of receipt of the paper in production.

Copyright: All authors must sign the Transfer of Copyright agreement before the article can be published. This transfer agreement enables Jordan Journal of Mechanical and Industrial Engineering to protect the copyrighted material for the authors, but does not relinquish the authors' proprietary rights. The copyright transfer covers the exclusive rights to reproduce and distribute the article, including reprints, photographic reproductions, microfilm or any other reproductions of similar nature and translations.

PDF Proofs: One set of page proofs in PDF format will be sent by e-mail to the corresponding author, to be checked for

typesetting/editing. The corrections should be returned within 48 hours. No changes in, or additions to, the accepted (and subsequently edited) manuscript will be allowed at this stage. Proofreading is solely the author's responsibility. Any queries should be answered in full. Please correct factual errors only, or errors introduced by typesetting. Please note that once your paper has been proofed we publish the identical paper online as in print.

Author Benefits

Page charge: Publication in this journal is free of charge.

Free off-prints: Three journal issues of which the article appears in along with twenty-five off-prints will be supplied free of charge to the corresponding author. Corresponding authors will be given the choice to buy extra off-prints before printing of the article.

Manuscript Preparation:

General: Editors reserve the right to adjust style to certain standards of uniformity. Original manuscripts are discarded after publication unless the Publisher is asked to return original material after use. If online submission is not possible, an electronic copy of the manuscript on disk should accompany the final accepted hardcopy version. Please use MS Word for the text of your manuscript.

Structure: Follow this order when typing manuscripts: Title, Authors, Affiliations, Abstract, Keywords, Introduction, Main text, Conclusions, Acknowledgements, Appendix, References, Figure Captions, Figures and then Tables. For submission in hardcopy, do not import figures into the text - see Illustrations. For online submission, please supply figures imported into the text AND also separately as original graphics files. Collate acknowledgements in a separate section at the end of the article and do not include them on the title page, as a footnote to the title or otherwise.

Text Layout: Use double spacing and wide (3 cm) margins. Ensure that each new paragraph is clearly indicated. Present tables and figure legends on separate pages at the end of the manuscript. If possible, consult a recent issue of the journal to become familiar with layout and conventions. All footnotes (except for table and corresponding author footnotes) should be identified with superscript Arabic numbers. To conserve space, authors are requested to mark the less important parts of the paper (such as records of experimental results) for printing in smaller type. For long papers (more than 4000 words) sections which could be deleted without destroying either the sense or the continuity of the paper should be indicated as a guide for the editor. Nomenclature should conform to that most frequently used in the scientific field concerned. Number all pages consecutively; use 12 or 10 pt font size and standard fonts. If submitting in hardcopy, print the entire manuscript on one side of the paper only.

Corresponding author: Clearly indicate who is responsible for correspondence at all stages of refereeing and publication, including post-publication. The corresponding author should be identified with an asterisk and footnote. Ensure that telephone and fax numbers (with country and area code) are provided in addition to the e-mail address and the complete postal address. Full postal addresses must be given for all co-authors. Please consult a recent journal paper for style if possible.

Abstract: A self-contained abstract outlining in a single paragraph the aims, scope and conclusions of the paper must be supplied.

Keywords: Immediately after the abstract, provide a maximum of six keywords (avoid, for example, 'and', 'of'). Be sparing with abbreviations: only abbreviations firmly established in the field may be eligible.

Symbols: All Greek letters and unusual symbols should be identified by name in the margin, the first time they are used.

Units: Follow internationally accepted rules and conventions: use the international system of units (SI). If other quantities are mentioned, give their equivalent in SI.

Maths: Number consecutively any equations that have to be displayed separately from the text (if referred to explicitly in the text).

References: All publications cited in the text should be presented in a list of references following the text of the manuscript.

Text: Indicate references by number(s) in square brackets in line with the text. The actual authors can be referred to, but the reference number(s) must always be given.

List: Number the references (numbers in square brackets) in the list in the order in which they appear in the text.

Examples:

Reference to a journal publication:

- [1] M.S. Mohsen, B.A. Akash, "Evaluation of domestic solar water heating system in Jordan using analytic hierarchy process". Energy Conversion & Management, Vol. 38, No. 9, 1997, 1815-1822.

Reference to a book:

- [2] Strunk Jr W, White EB. The elements of style. 3rd ed. New York: Macmillan; 1979.

Reference to a conference proceeding:

- [3] B. Akash, S. Odeh, S. Nijmeh, "Modeling of solar-assisted double-tube evaporator heat pump system under local climate conditions". 5th Jordanian International Mechanical Engineering Conference, Amman, Jordan, 2004.

Reference to a chapter in an edited book:

- [4] Mettam GR, Adams LB. How to prepare an electronic version of your article. In: Jones BS, Smith RZ, editors. Introduction to the electronic age, New York: E-Publishing Inc; 1999, p. 281-304

Free Online Color: If, together with your accepted article, you submit usable color and black/white figures then the journal will ensure that these figures will appear in color on the journal website electronic version.

Tables: Tables should be numbered consecutively and given suitable captions and each table should begin on a new page. No vertical rules should be used. Tables should not unnecessarily duplicate results presented elsewhere in the manuscript (for example, in graphs). Footnotes to tables should be typed below the table and should be referred to by superscript lowercase letters.

PAGES

PAPERS

- | | |
|-----------|---|
| 123 – 130 | Agent Based Fuzzy ARTMAP Neural Network For Classifying the Power Plant Performance
<i>Qasim M. Doos, Zouhair Al-Daoud, Suhair M. Al-Thraa</i> |
| 131 – 136 | Motion Planning for a Robot Arm by Using Genetic Algorithm
<i>Bahaa Ibraheem Kazem, Ali Ibrahim Mahdi, Ali Talib Oudah</i> |
| 137 – 142 | Experimental Investigation of Swirl-Stabilized Syngas Flames by Transverse Fuel Injection
<i>A. Bouziane, A. Olivani, A. Khalfi, F. Cozzi, A. Coghe</i> |
| 143 – 150 | Analysis of Longitudinal Aerodynamic Characteristics of an Aircraft Model with and Without Winglet
<i>Altab Hossain, Prithvi Raj Arora, Ataur Rahman, Abdul Aziz Jaafar, A.K.M. Parvez Iqbal</i> |
| 151 – 156 | Prediction of Friction Stir Welding Characteristic Using Neural Network
<i>Y. K. Yousif, K. M. Daws, B. I. Kazem</i> |
| 157 – 162 | Mathematical Modeling for Pump Controlled System of Hydraulic Drive Unit of Single Bucket Excavator Digging Mechanism
<i>Juma Yousuf Alaydi</i> |
| 163 – 168 | Experimental Investigation of Heat Transfer Enhancement in Radiating Pin Fin
<i>Ganesh Murali J., Subrahmanyam S. Katte</i> |
-

Agent Based Fuzzy ARTMAP Neural Network for Classifying the Power Plant Performance

Qasim M. Doos, Zouhair Al-Daoud *, Suhair M. Al-Thraa

Department of Mechanical Engineering, University of Baghdad, Baghdad, Iraq

Abstract

In this paper, we present a "Fuzzy ARTMAP" neural network model on a power station in Al-Daura Refinery for the multi-agent process as a classifying system to improve the process real-time performance. The proposed model is a combination of the Adaptive Resonance Theory (ART) neural network and fuzzy logic control, a supervised model having high on-line classifying accuracy learning mechanism with superior performance. The model has been applied for each agent autonomously according to agent's behaviour and standard level (S.L.) control. Results have shown that the "Fuzzy ARTMAP" neural network is able to precisely learn to classify the data fusion from the multi-agent process to three classes: class (S) when the data fusion are within the (S.L.), class (H) when the data fusion are higher than the (S.L.) and class (L) when the data fusion are under the (S.L.). Also, the "Fuzzy ARTMAP" is able to learn the rules and the parameters accurately with low cost, high performance and less effort.

© 2008 Jordan Journal of Mechanical and Industrial Engineering. All rights reserved

Keywords: Adaptive Resonance Theory; Neural Network; Fuzzy Logic Control; Fuzzy ARTMAP; Power Plant Performance

1. Introduction

Recently, the agent technology has been considered as an important approach for developing the intelligent systems that shows promises for improving their performance under real-time distributed environment. The agent technology is the fundamental cell of the distributed intelligence that provides many different solutions to commonly known problems faced in many fields. Hence, its artificial intelligence (AI) can be built by using all (AI) implementation technology currently known and it can compute regardless of its current location. However, the primary feature of agent technology is the agent's ability to communicate with each other. This enables the agents to unite their efforts to become a collective of working individuals who are aware of each other's goals. The neural network (NN) is one of the popular (AI) techniques, widely used in many applications. [1].

The ARTMAP is a class of neural network architecture that performs incremental supervised learning recognition to the input vectors. The first ARTMAP system was used to classify inputs by the set of features (also called pattern or vector) they possess of a binary values representing the presence of absence of each possible feature [2]. A new system, more general is called the fuzzy ARTMAP was developed to classify the inputs by a fuzzy set of features,

or patterns of fuzzy memberships values between 0 or 1 indicating the extent to which each feature is presented[3-4].

A verity of fuzzy ARTMAP on a cluster of workstations learns the required tasks fast and has the capability for on-line learning was implemented. It has the ability to provide the learning structure that allows explaining the answers that the neural network produces [5].

In this paper, a Fuzzy ARTMAP neural network model is proposed to classify the process performance of the multi-agent's behaviors in Al- Daura Refinery power station.

2. The Agent Definition

"The term agent can be defined as "anything that can be viewed as perceiving its environment through sensors & acting upon that environment through effectors"[6]. Alternatively, are software entities that carry out some set of operations on behalf of a user or another program with some of independence or autonomy and in so doing, employ some knowledge or representation of the user's goals or desires? "[7].

* Corresponding author. e-mail: ziaa04@yahoo.com

3. The Multi-Agent Systems

Multi-agent system can be used not only in distributed environment but in centralized system as well. For instance, having multiple agent could speed up systems operation by providing means for parallel computing. Particularly situations where the system design are highly modular, meaning that separate tasks are clearly divided and could be delegated to agents. The parallelism of the multi-agent systems can help to deal with limitations imposed by time-bounded reasoning requirements [6]. Generally, the term multi-agent system covers all types of systems composed of multiple autonomous components showing the following characteristics: [1].

- Each agent has incomplete capabilities to solve a problem and the data is decentralized.
- There is no global system control and the computation is asynchronous.

Figure (1) illustrates that each agent is part of the environment and modeled as a separate entity. There may be any number of agents, with different degree of heterogeneity and with or without the ability to communicate directly.

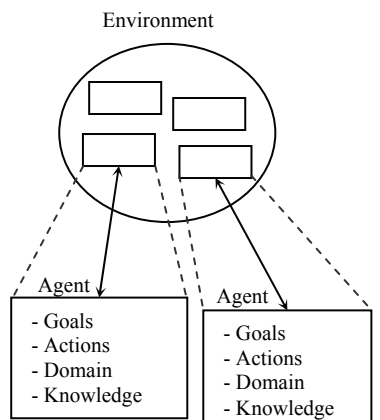


Figure 1: A General Multi-Agent framework [1].

4. The Fuzzy logic control

The basic idea behind Fuzzy Logic Control (FLC) is to incorporate the "expert experience" of a human operator in the design of the controller in controlling a process whose input-output relationship is described by a collection of fuzzy control rules (e.g., IF-THEN rule) involving linguistic variables rather than a complicated dynamic model. This utilization of linguistic variables, fuzzy control rules, and approximate reasoning provides a means to incorporate human expert experience in designing the controller [7]. In figure (2), a fuzzy controller is shown embedded in a closed-loop control system. The plant output is denoted by $y(t)$, its input is denoted by $u(t)$, and the reference input to the fuzzy controller is denoted by $r(t)$.

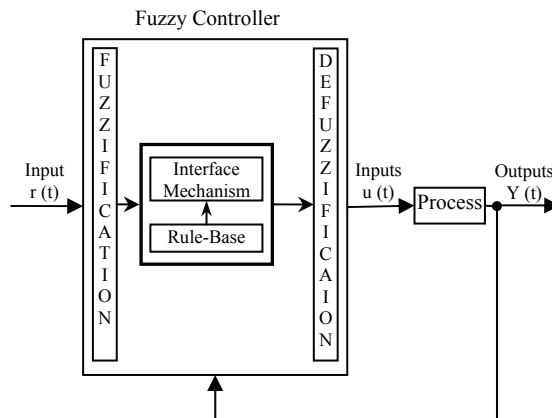


Figure 2: Fuzzy controller architecture [7].

5. The (ARTMAP) Neural Network

The ARTMAP stands for the Adaptive Resonance Theory with mapping. An ARTMAP network consists of two side-by-side ART models as shown in figure (3), the first ART is ARTA, which processes the input to detect categories of inputs. The second ART is ARTB, which examines the set of known outputs for output categories. The expectation or winning pattern from each ART is compared in a Mapping Field for a match.

The network processes the input and selects the appropriate category in the layer F_2^A based on the setting of the vigilance parameter ρ_A . The pattern associated with the winning F_2^A category is presented to the Mapping Field, which is labeled on the diagram as Inter-ART Associative Memory. Similarly, the paired output vector associated with the input vector is applied to the input of the ARTB network (right). The ART network then determines an appropriate output category for the ARTB input. The pattern associated with the winning F_2^B category is also presented to the Mapping Field. The two patterns are then compared with each other in the Mapping Field and held up against the Inter-ART vigilance parameter. If the match between the ARTA and ARTB output vector is suitable, then the weights between the layer F_2^A and the Mapping Field are adjusted to match the pattern presented by layer F_2^B . Simultaneously, the ARTA network resonates and learn its input pattern.

When the patterns at the Mapping Field do not meet the vigilance criterion, an Inter-ART reset is issued. During the Inter-ART reset, the vigilance parameter of the ARTA network is raised just far enough so that the winning neuron of ARTA no longer wins the competition. This causes the ARTA network to seek or create a new category in layer F_2^A . This particular feedback ensures that a new category is selected for data that does not fit the current pattern set. By dynamically adjusting the ARTA vigilance, the ARTMAP network ensures that there will be just enough categories created to cover all possible input-output pairs [10].

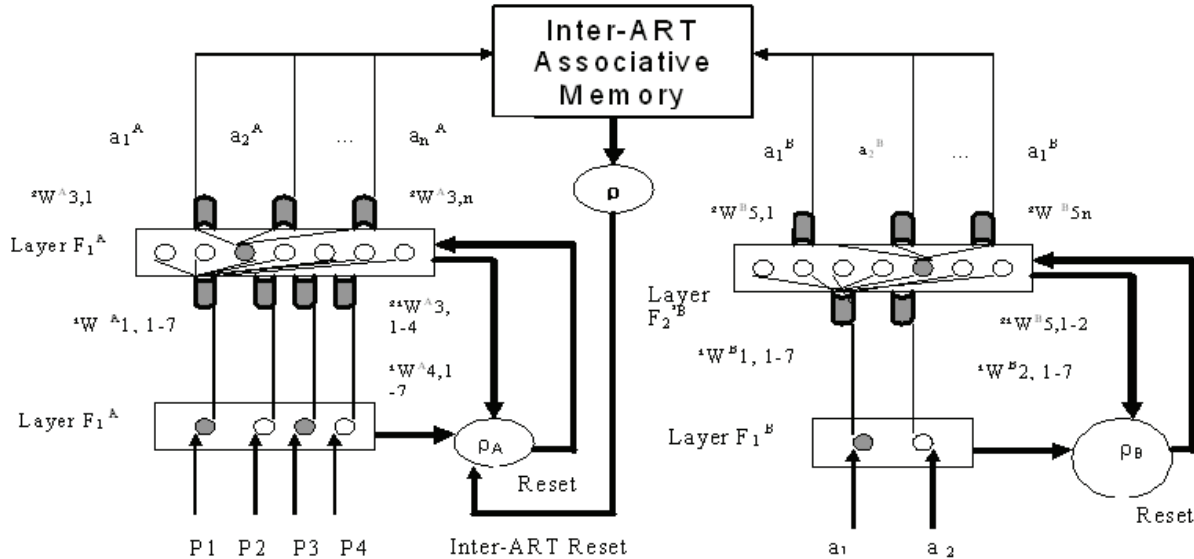


Figure 3: Block diagram of ART architecture [10].

6. Al-Daura Refinery Multi-agent Process

In general, the boiler is a device for generating steam, which can be used for the production of power or for the heating purpose. The thermal power station boiler usually consists of different equipments working together with the aim of converting chemical energy of fuel in to heat energy in the steam, which is generated at certain pressure and temperature. The energy stored in the steam is converted to kinetic energy in the turbine then in to electrical energy in the power generator .For this reason, it is obviously clear that the performance of the boiler will directly affect the whole power system. Therefore, it is logical to seek better conditions for improving the performance of the power plant station.

In Al-Daura Refinery, the boiler shown in figure (4) has been selected as a prototype for this research. The boiler has a performance of 310 KW; its continuous operating rate for steam is 142 ton/hr at a temperature and pressure of 260 °C and 20 bar at full load. The feed water is fed in to the boiler by the feed water pumps to the economizer tubes. In the economizer, the water absorbs heat from the flue gases leaving the boiler and its temperature increases to a certain value, which is below the saturation temperature corresponding to the drum pressure. From the economizer, water flows in to the drum from which the water flows to the water walls through the down comer in a natural circulation mode. In this circulation, a great amount of heat will transfer to the water so that boiling takes place, and the motion of fluid is setting up resulting from the density difference caused by the temperature difference in the fluid. As the water from the bottom of the water walls flows upward, the process of heat transfer takes place, and at the top of the water walls, a certain percentage of the water may be vaporized. When the water-steam mixture flows back to the drum, condensation and vaporization take place simultaneously.

The water, which separates from the water-steam mixture, will mix with the water at the bottom of the drum. This water has a temperature slightly below the saturation temperature and flow in the down comer with the water coming from the economizer for the next circulation. The separated steam leaves the drum and enters the super heater section.

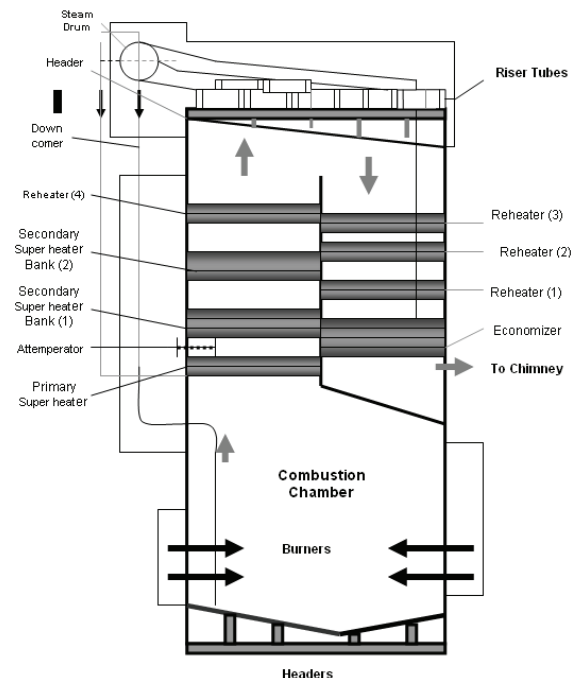


Figure 4: The Boiler System.

In the super heater section, the steam passes through various tube banks. These tubes are mounted in the horizontal position and some are vertical .This super heater is divided to primary super heaters and secondary super heaters, each consists of two bank tubes .There is a spray attemperator between the outlet of the second bank of the

primary super heaters and the inlet of the secondary super heater. The attemperator is used only for controlling the temperature of the steam flowing to the high-pressure turbines. The exhausted steam from the high-pressure turbine is reheated in the four reheaters mounted in the convection section in order to raise its temperature to be used in the driving of the intermediate pressure turbine [11].

To extend life and managing operations and control activities of the power generation unit, information and network technologies have to play an important role to ensure the safety functioning and controlling the unit operations. The data and knowledge basis will be used for the analytical methods as inputs-outputs database in the construction of the agent – based genie project. Table (1) illustrates the multi agent process of the boiler hardware.

Table 1: illustrates the Boiler control system items.

No. Items	Units	Tags (Agents)	Standard Level
1. Steam Drum Level	mm	LRCA-1355	+50 to +200
2. Boiler Feed Water Flow	Ton/hr	FRC-1357	70 to 110
3. Boiler Feed Water Pressure	Bar	PI-1360	33 to 40
4. Boiler Feed Water Temperature	°C	TR-1352	115 to 125
5. Boiler Feed Water Level	mm	LIC-1351	+100 to +200
6. Main Steam Flow	Ton/hr	FR-1356	50 to 110
7. Main Steam Temperature	°C	TRCA-1353	260 to 280
8. Main Steam Pressure	Bar	PICA-1361	19 to 20
9. Fuel Oil Pressure	Bar	PIA-1356	6.8 to 15
10. Fuel Oil Flow	m ³ /hr	FRC-1351	3 to 7.5
11. Oil/Steam Diff. Pressure	Bar	PDICA-1354	1.5 to 3
12. Fuel Oil Temperature	°C	TAR-1351	90 to 110
13. Low Pressure Steam	Ton/hr	PI-1351	1 to 3

7. The Implementation Methodology

7.1. The Agent Configuration Management

The behavioral agents combine to give an overall configuration management system for the complete product lifecycle. This system has been developed to support earlier work on change propagation in an integrated design environment where the behavioral agents define the rules for co-operation and change management also it has the knowledge about the design entities and their relationships. The first aspect of the configuration management scheme is the labeling of the design model and hence the process of change is represented within our labeling scheme as referring to Table 2. The agents are labeled as shown in Table 2

7.2. The Behavioral Agents

The behavioral of agents is the representation of each design discipline in the agent structure, which contains the rules about the co-operation and negotiation with other agents and uses these to control the final output. Its goal is the global consistency of data and the ability to reflect the change in all the models of a disparate design process. The rules for controlling these agents depend on the

relationships between them. Figure 5 describe the relationship between these agents.

Table 2: The Labeled Agents.

No.	Agents	Label	No.	Agents	Label
1.	LRCA-1355	A	8.	PICA-1361	H
2.	FRC-1357	B	9.	PIA-1356	I
3.	PI-1360	C	10.	FRC-1351	J
4.	TR-1352	D	11.	PDICA-1354	K
5.	LIC-1351	E	12.	TAR-1351	M
6.	FR-1356	F	13.	PI-1351	Q
7.	TRCA-1353	G			

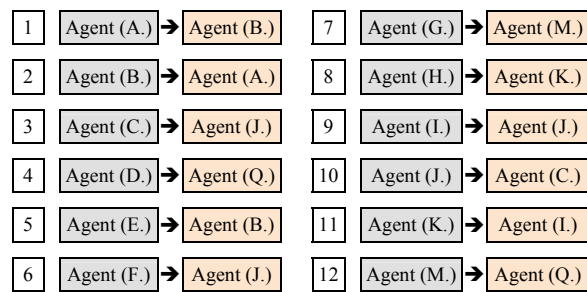


Figure 5: The Relationship between the Agents

8. The Fuzzy "ARTMAP" Algorithm

The Fuzzy ARTMAP Algorithm is used for each agent in the boiler for classifying. This algorithm is summarized as follows:

Step 0: Let m be the number of input units, n be the number of output units, M be the number of units on F_2^a , and N be the number of the units on F_2^b . Initially, all the adaptive weights W_j^a , W_k^b and W_{jk}^{ab} are set equal to 1.

$$W_{j1}^a(0) = \dots = W_{j2m}^a = 1 \quad (1)$$

$$W_{k1}^b(0) = \dots = W_{j2n}^b = 1 \quad (2)$$

$$W_{jk}^{ab}(0) = 1 \quad (3)$$

Where j=1,..., M and k=1, ..., N

Initialize all category nodes of ART modules, ART_a & ART_b then set the parameters: The choice parameter $\alpha > 0$. The learning rate parameter $\beta \in [0, 1]$. The vigilance parameters ρ_a , ρ_b , $\rho_{ab} \in [0, 1]$. Set the ART_a vigilance parameters, ρ_a , to the baseline vigilance, ρ_a .

Step 1: Present a binary or analogue vector a and the corresponding class vector b . The vector a is input to the model ART_a and the vector b is input to the model ART_b . All input values of vector a must be with the range [0, 1]. If not, the inputs to the ART_a are analogue, then the input vector a should be normalized. The component coding is also required to preserve amplitude information, then the component coded for input vector A is input to the field F_1^a . While the component coded for input vector B is input to the field F_1^b .

$$A = (a, a^c) = (a_1, \dots, a_m, a_1^c, \dots, a_m^c) \quad (4)$$

$$B = (b, b^c) = (b_1, \dots, b_m, b_1^c, \dots, b_m^c) \quad (5)$$

Step 2: For each input vector \mathbf{A} and \mathbf{B} , the j^{th} node in the layer, F_2^a , and k^{th} node in the layer, F_2^b , are given by:

$$T_j(A) = \frac{|A \wedge W_j^a|}{\alpha + |W_j^a|} \quad (6)$$

$$T_j(B) = \frac{|B \wedge W_k^b|}{\alpha + |W_k^b|} \quad (7)$$

Where the fuzzy MIN operator \wedge is defined to be $(x \wedge y)_i = (x_i, y_i)$, α is a choice parameter, and the norm $|\cdot|$ is defined to be: $|x| = \sum |x_i|$ for any vector x and y .

Step 3: Use a winner-take-all rule to select the winner. This yields the maximum weighted sum. The winner of ART_a and ART_b are indeed by j and k respectively where:

$$J = \max \{T_j(A); j=1, \dots, M\} \quad (8)$$

$$K = \max \{T_k(B); k=1, \dots, N\} \quad (9)$$

If more than one node is maximal on each module, the node with the smallest index is chosen to break the tie.

Step 4: Check the vigilance criteria. If nodes j and k satisfy the conditions.

$$\frac{|A \wedge W_j^a|}{|A|} \geq \rho_a \quad (10)$$

$$\frac{|B \wedge W_k^b|}{|B|} \geq \rho_b \quad (11)$$

The nodes j and k are chosen to represent the input pattern \mathbf{A} and \mathbf{B} , and proceed to **Step 5**. After the categories represented by nodes j and k are selected for learning, they become committed. If they violate the above condition, then node j and k are reset and move back to step 3. Search for another node in the F_2^a and F_2^b that satisfies vigilance criterion respectively.

Step 5: Check to see whether the match-tracking criterion is satisfied .If

$$\frac{|y^b \wedge W_j^{ab}|}{|y^b|} \geq \rho_{ab} \quad (12)$$

Then we have achieved the desired mapping and continue to **step 6** for LTM (Long Term Memory) learning. If

$$\frac{|y^b \wedge W_j^{ab}|}{|y^b|} < \rho_{ab} \quad (13)$$

Then the mapping between J and K is not the desired one. In this case, the vigilance parameter ρ_a is increased

until it is slightly larger than $|A \wedge W_j^a| / |A|$; this leads to an immediate reset of node J in ART_a and a move to Step 3 with the new vigilance parameter for the selection of another node in F_2^a that will achieve the desired mapping.

Step 6: The weights W_j^a and W_k^b are updated by the equations.

$$W_j(t) = \beta (A \wedge W_j(t-1)) + (1-\beta) W_j(t-1) \quad (14)$$

$$W_k(t) = \beta (B \wedge W_k(t-1)) + (1-\beta) W_k(t-1) \quad (15)$$

Where the learning rate β is chosen in the range [0, 1]. In the fast learning mode, β is set to 1. The weights W_j^a , $j \neq J$ and W_k^b , $k \neq K$ of non-winning nodes are not updated. For efficient coding of noisy input sets, fast-commit and slow recording, which is to set $\beta < 1$ after the category committed, is normally being used. The Map Field weights with fast learning are determined by:

$$W_{jk}^{ab}(t) = 1 \text{ if } j = J, K = k \quad (16)$$

$$W_{jk}^{ab}(t) = 0 \text{ if } j = J, K \neq k \quad (17)$$

$$W_{jk}^{ab}(t) = W_{jk}^{ab}(t-1) \text{ otherwise} \quad (18)$$

Step 7 Go to **Step 1** and present a next pattern pair.

Tables 3 illustrate the fuzzy ARTMAP parameters used for the simulation. To perform useful functions in these environment agents, the agents must be both pro-active and reactive. To be pro-active it must be able to choose actions directed towards achieving specific goals or specific tasks. To be reactive it must be able to respond in a timely manner to unexpected changes in the environment.

Table 3: The Fuzzy ARTMAP parameters

Parameters	Description
$C = 0.001$	Match tracking parameter (increase ART _a vigilance).
$\alpha = 0.001$	Choice parameter for search order of fuzzy ART modules.
$\beta_a = 0.001$	Fuzzy ART _a learning rate.
$\beta_b = 1.0$	Fuzzy ART _b learning rate.
$\beta_{ab} = 1.0$	Map field learning rate.
$\rho_a = 0.0$	Baseline Fuzzy ART _a vigilance.
$\rho_b = 1.0$	Baseline Fuzzy ART _b vigilance
$\rho_{ab} = 1.0$	Map field vigilance

The exploration of the network variations begin by varying the baseline vigilance. The selection of the proposed Fuzzy ARTMAP decision thresholds for the output class is divided to three classes as the following:

- A) (L) class:** which means that the data received from the environment is less than the standard level.
- B) (H) class:** which means that the data received from the environment is higher than the standard level.
- C) (S) class:** which means that the data received from the environment is at the standard level (the desired situation) then it will switch out to the environment and will not enter to the LCS systems. Figure (6) shows the architecture of the fuzzy ARTMAP for each agent.

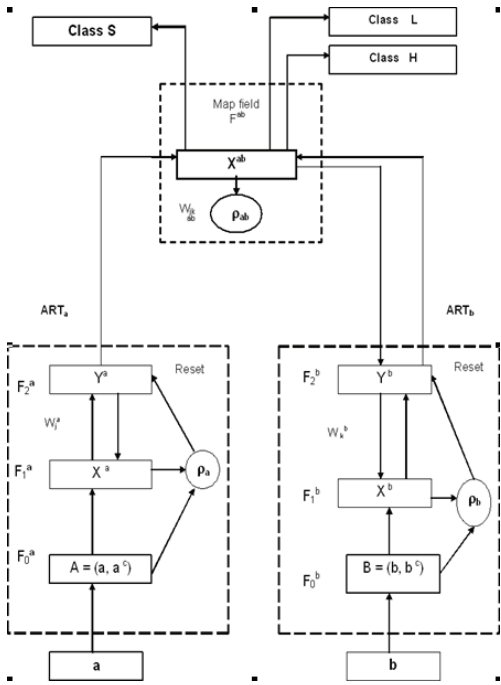


Figure 6: The Fuzzy ARTMAP Architecture

9. The Model Implementation

The proposed software model for the multi-agent process is designed to train the fuzzy ARTMAP neural network for each agent separately depending on each specification and according to its procedures, the training data must be prepared previously. The data were extracted from the position every one hour according to the boiler practical situation for ten days from 1-9-2005 to 10-9-2005. Figure (7) shows the software framework of the model. Table (4) shows a sample of the running model.

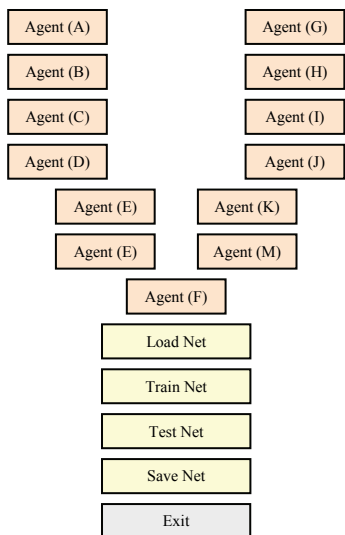


Figure 7: The Fuzzy ARTMAP Software Model

Table (4): A Sample of Agent (A) running

Agent (A)	Level						
0.744396	S	0.858539	S	156.3232	S	180.2932	S
0.062749	S	0.421835	S	13.17725	S	88.58543	S
0.63739	S	0.179003	S	133.8519	S	37.59062	S
0.390038	S	0.50259	S	81.90791	S	105.5439	S
0.254596	L	0.081625	L	53.4651	S	17.14123	L
0.239384	S	0.673162	S	50.27063	S	141.3641	S
0.647367	S	0.789433	S	135.9472	S	165.781	S
0.495934	S	0.088526	S	104.1462	S	18.5905	S
0.711368	S	0.933985	S	149.3873	S	196.1369	S
0.694442	S	0.852391	S	145.8327	S	179.0021	S
0.504162	S	0.291228	S	105.8739	S	61.15791	S
0.270286	S	0.828359	S	56.76009	S	173.9553	S
0.851376	S	0.858949	S	178.7889	S	180.3792	S
0.027961	L	0.29293	L	5.87174	L	61.51524	L
0.245269	S	0.769304	S	51.50646	S	161.5537	S
0.270299	S	0.454756	S	56.76278	S	95.49866	S
0.386139	S	0.509952	S	81.08924	S	107.0898	S
0.455443	S	0.31024	S	95.643	S	65.15031	S
0.208302	S	0.655997	S	43.74339	S	137.7595	S
0.574673	S	0.115217	S	120.6812	S	24.19567	S
0.219899	S	0.594284	S	46.17871	S	124.7995	S
0.713845	S	0.599868	S	149.9075	S	125.9722	S
0.639814	S	0.32645	S	134.361	S	68.55455	S
0.374743	L	0.006961	L	78.69595	L	1.461829	L
0.933769	S	0.221965	S	196.0914	S	46.61265	S
0.802363	S	0.165468	S	168.4963	S	34.74826	S
0.099974	L	0.166485	L	20.99444	L	34.9618	L
0.872549	S	0.679405	S	183.2354	S	142.675	S
0.247839	S	0.928698	S	52.04625	S	195.0267	S
0.053878	S	0.687809	S	11.31435	S	144.44	S
0.340041	S	0.685062	S	71.40856	S	143.8629	S
0.849493	S	0.911357	S	178.3935	S	191.3849	S
0.40166	S	0.739697	S	84.34867	S	155.3364	S
0.076722	L	0.06972	L	16.11169	L	14.64119	L
0.373449	S	0.146526	S	78.42431	S	30.77039	S
0.490832	S	0.016048	S	103.0747	S	3.370002	S
0.656086	S	0.739813	S	137.778	S	155.3608	S
0.085137	S	0.796391	S	17.87885	S	167.2422	S
0.736338	S	0.370583	S	154.6309	S	77.82237	S
0.788468	S	0.029144	S	165.5782	S	6.120259	S
0.325551	S	0.705109	S	68.36575	S	148.0729	S
0.263995	S	0.229709	S	55.43899	S	48.23896	S
0.153648	S	0.824593	S	32.26615	S	173.1646	S
0.511195	S	0.21376	S	107.351	S	44.88963	S
0.439011	S	0.707089	S	92.19228	S	148.4888	S
0.116731	L	0.091639	L	24.51352	L	19.24409	L

10. Conclusions

The "Fuzzy ARTMAP" neural network has an on-line fast learning mechanism and has the superior performance for classifying, with very low computing costs for learning strategy. The experiments emphasize that the boiler performance has been classified to three classes: class (S) when the data fusion is within the standard level (S.L.),

class (H) when the data fusion are higher than the standard level (S.L.) and class (L) when the data fusion are under the standard level (S.L.). This finding emphasizes that the dynamic fuzzy neural network has a potential for mapping the error and detecting the class's deviation with less efforts and low cost. The effectiveness of using the dynamic fuzzy ARTMAP is confirmed by the simulation results in which three typical levels has been present

References

- [1] J. Huhtinen, "The system architecture requirement specification." Genie Project Internal Report 2 (2000).
- [2] G.A.Carpenter, S.Grossberg, and J.H.Reynolds, "ARTMAP: Supervised real-time learning and classification of no stationary data by a self-Organizing neural network", Neural network, , 1991, Vol.4, 565–588.
- [3] G.A.Carpenter, and S.Grossberg "A massively parallel architecture for a self-organizing neural pattern recognition machine ,,"Computer Vision, Graphics and Image Processing,1987, Vol. 37, 54-115
- [4] G.A.Carpenter, and S.Grossberg,Pattern recognition by self-organizing neural network, Camberidge:, MA, The M.I.T Press, 1991.
- [5] Castro et al, "The experiments with the ART neural networks implementation on a Beowulf cluster ,," ARTMAP project, 2004.
- [6] H., Park, J., Tenenbaum. and R., Dove "Agile Infrastructure for Manufacturing: A Vision for Transforming the U.S. Manufacturing Base", Defense Manufacturing Conference, 1993.
- [7] The IBM," Intelligent Agent Resource Manager" Open Blueprint, G325-6592-0,
URL:<http://www.activist.gp1.ibm.com;81/whitepaper/ptc2.htm>, 1996. .
- [8] Qiao B. and Zhu J. Agent-based Intelligent Manufacturing system for the 21 century. 2000.
- [9] K. M., Passino and S., Yurkovich, Fuzzy Control, Menlo Park, CA, Addison Wesley, 1998.
- [10] Regan T., Sinnock H. and Davis A., Distributed Energy Neural Network Integration System, National Renewable Energy Laboratory (NREL), Golden, Colorado ,(2003).
- [11] "Operation Maintenance Manual "Boiler and Auxiliaries, Hyundai Engineering and Construction Co., LTD. 1976.

Motion Planning for a Robot Arm by Using Genetic Algorithm

Bahaa Ibraheem Kazem *, Ali Ibrahim Mahdi, Ali Talib Oudah

Mechatronics Engineering Dept., Al-Khawarizmi College of Engineering, University of Baghdad, Baghdad, Iraq

Abstract

This paper proposes genetic algorithm (GA) to optimize the point-to-point trajectory planning for a 3-link (redundant) robot arm. The objective function for the proposed GA is to minimizing traveling time and space, while not exceeding a maximum pre-defined torque, without collision with any obstacle in the robot workspace. Quadrinomial and quintic polynomials are used to describe the segments that connect initial, intermediate, and final point at joint-space. Direct kinematics has been used for avoiding the singular configurations of the robot arm.

© 2008 Jordan Journal of Mechanical and Industrial Engineering. All rights reserved

Keywords: robot motion planning; genetic algorithm; obstacle avoidance

1. Introduction

In the last decade, genetic algorithms (GAs) have been applied in large number of fields such as in control, parameter, and system identification, robotics, planning and scheduling, image processing, pattern recognition, speech recognition. This paper addresses the area of robotics, namely the point-to-point trajectory planning for mechanical manipulators. At start, some of conventional methods have been used for trajectory planning.

For generating smooth trajectory planning for specified path, Z. Zoller and P. Zentay [1] focused on the problem of the trajectory planning and dealt with constant kinetic energy motion planning. The authors used Euclidean space to provide the equation of dynamic of robot motion with constant kinetic energy. This method produced trajectory characteristics smoother and better than which did obtained from time optimal method. Nevertheless, it can be implemented only for pre-specified path.

Zhe Tang et al. [2] proposed a third-order spline interpolation based trajectory-planning method to plan a smooth biped swing leg trajectory by reducing the instant velocity change, which occurs at the time of collision of the biped swing leg with the ground. The authors demonstrate that the impact effects can be avoided at the time of the swing foot's heel touching with the ground.

About on line trajectory planning, Chwa et al. [3] proposed "Missile Guidance Algorithm" to generate on-line trajectory planning of robot arms of the interception of a fast maneuvering object. The authors employed the guidance law throughout the tracking phase, and dynamic constraints such as torque and velocity constraints and

satisfied the matching condition of the position and velocity at the time of the interception altogether. This was carried out by introducing body axis (as well as joint and inertia axis) as trajectory planning coordinates and separating the trajectory-planning problem into direction planning and speed planning of robot arm.

Various methods for trajectory planning schemes based on GAs have been proposed. P. Garg and M. Kumar [4] use GA techniques for robot arm to identify the optimal trajectory based on minimum joint torque requirements. The authors use polynomial of 4th degree in time for trajectory representation to joint space variables.

Pires and Machado [5] propose a path planning method based on a GA while adopting the direct kinematics and the inverse dynamics. The optimal trajectory is the one that minimize the path length, the ripple in the time evolution and the energy requirements, without any collision with the obstacle in the workspace.

Pires et al. [6] optimized robot structure while optimizing the required manipulating trajectories using GA. The objective is to minimize the space/time ripple in the trajectory without colliding with any obstacles in the workspace, while optimizing the mechanical structure.

S. G. Yue et al. [7] focused on the problem of point-to-point trajectory planning of flexible redundant robot manipulator (FRM) in joint space. The proposed trajectory to minimize vibration of FRMs is based on GA. The authors use quadrinomial and quintic polynomials to describe the segment, which connects the initial, intermediate, and final points in joint space.

Pires et al [8] use genetic algorithm to optimize a planar robot manipulator trajectory. The GA objective is to minimize the trajectory space/time ripple without

* Corresponding author. e-mail: drbahaa@gmail.com

exceeding the maximum pre-defined torque. The authors use direct kinematics to avoid the singularities.

In this line of through, this paper, propose a point-to-point trajectory planning method based on GA while adopting the direct kinematics and the inverse dynamics. The optimum trajectory is the one that minimize both traveling time and traveling space, while not exceeding the maximum pre-defined torque, without collision with any obstacle in the workspace.

Bearing these ideas in mind, this paper is organized as following. Section 2 presents the robot motion planning strategy. Section 3 introduces GA motion planning scheme. Section 4 presents operators in genetic algorithm. Section 5 presents evolution criteria. Based this formulation, section 6 presents the case studies and simulation, the results are also discussed in this section. Finally, section 7 outlines the main conclusions.

2. Motion Planning Strategy

The supposed point-to-point trajectory is connected by several segments with continuous acceleration at the intermediate via point as shown in figure 1. The intermediate points can be given as particular points that should be passed through.

For a robot, the number of degrees of freedom of a manipulator is n and the number of end-effectors degree of freedom is m . If one wishes to be able to specify the position, velocity, and acceleration at the beginning and the end of a path segment, a quadrinomial and a quintic polynomial can be used. Let us assume that there is m_p intermediate via points between the initial and final points.

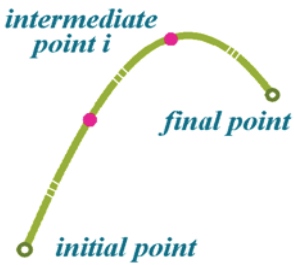


Figure 1: Intermediate points on the point-to-point trajectory

Between the initial points to m_p intermediate via points, a quadrinomial is used to describe these segments as [7]:

$$\theta_{i,i+1}(t) = a_{i0} + a_{i1}t_i + a_{i2}t_i^2 + a_{i3}t_i^3 + a_{i4}t_i^4, \quad (i=0, \dots, m_p-1) \quad (1)$$

Where (a_{i0}, \dots, a_{i4}) are constants, and the constraint are given as:

$$\theta_i = a_{i0} \quad (2)$$

$$\theta_{i+1} = a_{i0} + a_{i1}T_i + a_{i2}T_i^2 + a_{i4}T_i^4 \quad (3)$$

$$\dot{\theta}_i = a_{i1} \quad (4)$$

$$\dot{\theta}_{i+1} = a_{i1} + 2a_{i2}T_i + 3a_{i3}T_i^2 + 4a_{i4}T_i^3 \quad (5)$$

$$\ddot{\theta}_i = 2a_{i2} \quad (6)$$

Where T_i is the execution time from point i to point $i+1$. The five unknowns can be solved as:

$$a_{i0} = \theta_i \quad (7)$$

$$a_{i1} = \dot{\theta}_i \quad (8)$$

$$a_{i2} = \ddot{\theta}_i / 2 \quad (9)$$

$$a_{i3} = (4\theta_{i+1} - \dot{\theta}_{i+1}T_i - 4\theta_i - 3\ddot{\theta}_iT_i^2) / T_i^3 \quad (10)$$

$$a_{i4} = (\dot{\theta}_{i+1}T_i - 3\theta_{i+1} + 3\theta_i + 2\dot{\theta}_iT_i + \ddot{\theta}_iT_i^2 / 2) / T_i^4 \quad (11)$$

The intermediate point $(i+1)$'s acceleration can be obtained as:

$$\ddot{\theta}_{i+1} = 2a_{i2} + 6a_{i3}T_i + 12a_{i4}T_i^2 \quad (12)$$

The segment between the number m_p of intermediate points and the final point can be described by quintic polynomial as:

$$\theta_{i,i+1}(t) = b_{i0} + b_{i1}t_i + b_{i2}t_i^2 + b_{i3}t_i^3 + b_{i4}t_i^4 + b_{i5}t_i^5, \quad (i=mp) \quad (13)$$

Where the constants are given as:

$$\theta_i = b_{i0} \quad (14)$$

$$\theta_{i+1} = b_{i0} + b_{i1}T_i + b_{i2}T_i^2 + b_{i3}T_i^3 + b_{i4}T_i^4 + b_{i5}T_i^5 \quad (15)$$

$$\dot{\theta}_i = b_{i1} \quad (16)$$

$$\dot{\theta}_{i+1} = b_{i1} + 2b_{i2}T_i + 3b_{i3}T_i^2 + 4b_{i4}T_i^3 + 5b_{i5}T_i^4 \quad (17)$$

$$\ddot{\theta}_i = 2b_{i2} \quad (18)$$

$$\ddot{\theta}_{i+1} = 2b_{i2} + 6b_{i3}T_i + 12b_{i4}T_i^2 + 20b_{i5}T_i^3 \quad (19)$$

In addition, these constraints specify a linear set of six equations with six unknowns whose solution is:

$$b_{i0} = \theta_i \quad (20)$$

$$b_{i1} = \dot{\theta}_i \quad (21)$$

$$b_{i2} = \ddot{\theta}_i / 2 \quad (22)$$

$$b_{i3} = (20\theta_{i+1} - 20\theta_i - (8\dot{\theta}_{i+1} + 12\dot{\theta}_i)T_i - (3\ddot{\theta}_i - \ddot{\theta}_{i+1})T_i^2) / 2T_i^3 \quad (23)$$

$$b_{i5} = (12\theta_{i+1} - 12\theta_i - (6\dot{\theta}_{i+1} + 6\dot{\theta}_i)T_i - (\ddot{\theta}_i - \ddot{\theta}_{i+1})T_i^2) / 2T_i^5 \quad (24)$$

As formulated above, the total parameters to be determined are the joint angles of each intermediate via point ($n \times m_p$ parameters), the joint angular velocities of each intermediate point ($n \times m_p$ parameters), the execution time for each segment (m_p+1 parameters), and the posture of the final configuration ($n-m$).

Therefore, for 3-link robot case, it used $m_p=1$, $n=3$ and one degree of freedom of redundancy for the final point, there are nine parameters to be determined.

It should be point out that joint angular acceleration at each intermediate point could be obtained via equation (12). If all the intermediate points are connected by quintic polynomial, there will be eight parameters to be determined. This would be more time-consuming, which is why we choose both quadrinomial and quintic polynomial to generate the segments.

3. The GA Motion Planning Scheme

The GA planning scheme renders an optimized trajectory having minimum space, minimum time, while

not exceeding a maximum pre-defined torque, without colliding with any obstacle in the workspace. The motion planning adopts direct kinematics to avoid singularity problems. The trajectory parameters are encoded directly, using real codification, as strings (chromosomes) to be used by GA.

For 3R, redundant robot there are nine parameters should be optimized as shown in the following chromosome:

$$[q_1, q_2, q_3, q_g, \dot{q}_1, \dot{q}_2, \dot{q}_3, t_1, t_2] \quad (25)$$

Where q_i and \dot{q}_i are intermediate joint angle and velocity for i th joint respectively, q_g is the global angle of the final configuration of the end-effectors which equals the sum of joint angles of the manipulator [16], t_1 is execution time from initial to intermediate via point, and t_2 is execution time from intermediate to final point.

4. Operators in genetic algorithm

The initial population of strings is generated at random and the search is then carried out among this population. The evolution of the population elements is non-generational, meaning that the new replace the worst elements. The main different operators adopted in the GA are reproduction, crossover, and mutation.

In what concerns the reproduction operator, the successive generations of new strings are generated based on their fitness values. In this case, a 5-tournament is used to select the strings for reproduction.

With a given probability P_c , the crossover operator adopted the single point technique and, therefore, the crossover point is only allowed between genes or, in other words, the crossover operator cannot disrupt genes.

The mutation operator replaces one gene value x_i with another one generated randomly with a specified range by a given probability P_m . figure 2 shows the flow chart of the above steps of GA.

5. Evolution Criteria

Four indices are used to qualify the evolving trajectory robotic manipulators free workspace. All indices are translated into penalty functions to be minimized. Each index is computed individually and is integrated in the fitness function evaluation. The fitness function f_f adopted for evaluating the candidate trajectories is defined as:

$$f_f = \beta_1 f_{ot} + \beta_2 f_q + \beta_3 f_c + \beta_4 f_T \quad (26)$$

The optimization goal consists in finding a set of design parameters that minimize f_f according to the priorities given by the weighting factors β_i ($i = 1,.., 4$), where each different set of weighting factors must results in a different solution.

The f_{ot} index represents the amount of excessive driving, in relation to the maximum torque $\tau_{i \max}$, that is demanded for the i th joint motor for the trajectory under

consideration using the equation (28) which is called the cost function [9].

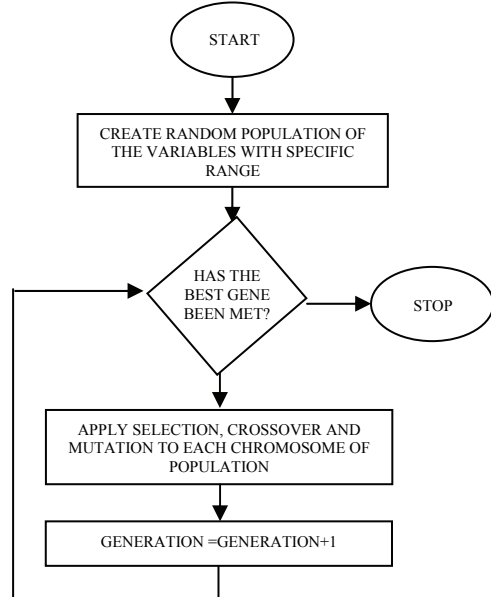


Figure 2: flow chart of GA

$$f_{ot} = \sum_{j=1}^b \sum_{i=1}^a f_i^j \quad (27)$$

$$f_i^j = \begin{cases} 0 & |\tau_i^j| < \tau_{i \max} \\ |\tau_i^j| - \tau_{i \max} & \text{otherwise} \end{cases} \quad (28)$$

Where a is number of robot links, and b is number of joint positions from the initial to final configuration.

The dynamic equations of the 3R manipulator can be easily obtained from the iterative Newton-Euler dynamics algorithm [8]. For simplicity, all mass exist as a point mass at the distal end of each link as shown in figure 3.

The index f_q represents the total joint traveling distance of the manipulator as criteria:

$$f_q = \sum_{i=1}^a \sum_{j=2}^b |q_{ij} - q_{ij-1}| \quad (29)$$

The index f_c represents total Cartesian trajectory length, as criteria:

$$f_c = \sum_{j=2}^b d(p_j, p_{j-1}) \quad (30)$$

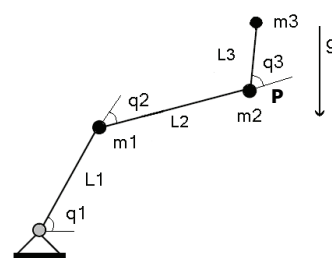


Figure 3: The 3R robot

Where p_j is the robot j th intermediate arm Cartesian position and $d(.,.)$ is a function that gives the distance between the two arguments. The index t_T represents the total consumed time for robot motion, as criteria:

$$t_T = t_1 + t_2 \quad (31)$$

Where t_1 and t_2 are the execution time from start to intermediate configuration, and from intermediate to target configuration, respectively.

For obstacle existence workspace, obstacle avoidance objective function f_{ob} has been combined with free space fitness function to form over all fitness function f , as shown below:

$$f = f_f / f_{ob} \quad (32)$$

By f_{ob} , the robot manipulator has the ability to avoid the obstacle collision during its movement from point to point in side the workspace. f_{ob} can be depicted as [11]: all links of configurations, which formed, by the joint positions between the initial and final robot configurations do not intersect obstacle region. The fitness value is $f_{ob}=1$.

Therefore,, the objective function of collision avoidance f_{ob} can be written as equation (33).

$$f_{ob} = \begin{cases} 1 & \sum_{j=1}^b \sum_{i=1}^a (\text{link}_{ij} \cap \text{obstacle}) = 0 \\ 0 & \text{otherwise} \end{cases} \quad (33)$$

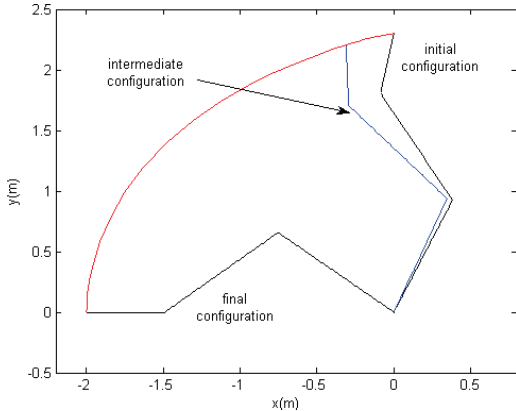


Figure 4: Cartesian path for the end effectors of the robot in free workspace

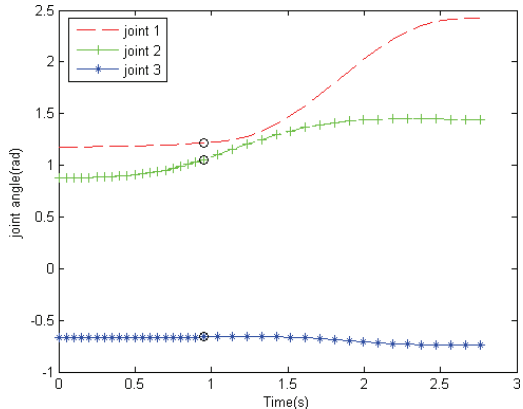


Figure 5: Joint angle versus time in free workspace

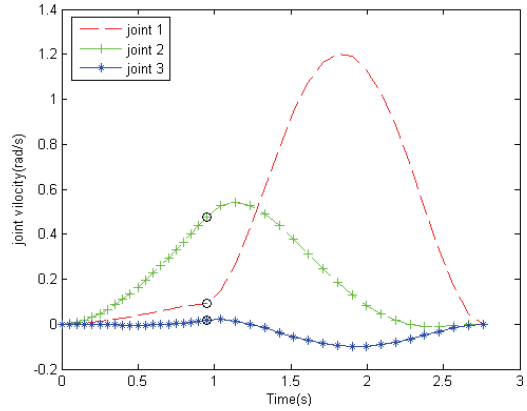


Figure 6: Joints velocity versus time in free workspace

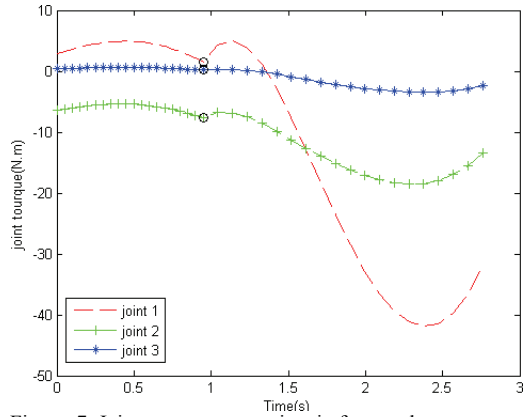


Figure 7: Joints torque versus time in free workspace

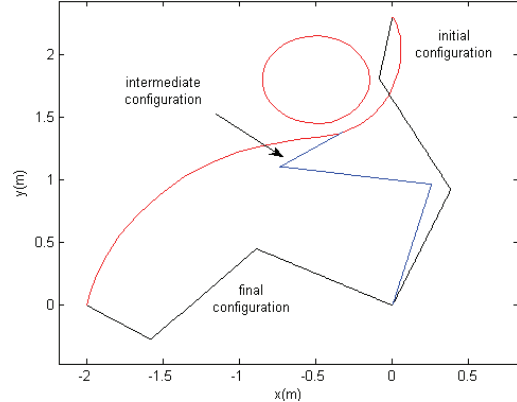


Figure 8: Cartesian path for the end effectors of the robot with obstacle existence

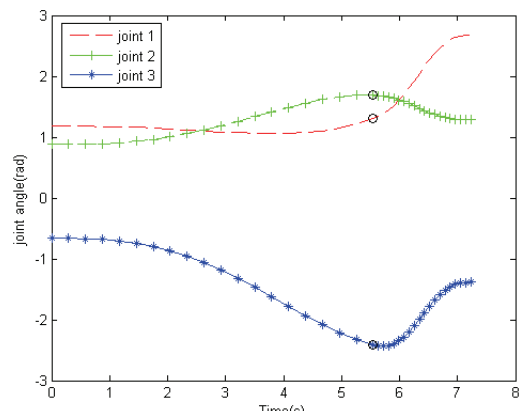


Figure 9: Joint angle versus time with obstacle avoidance

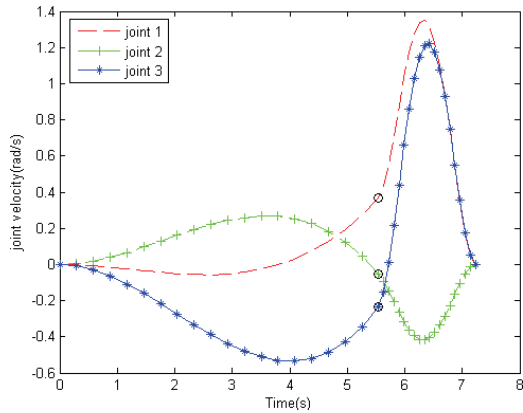


Figure 10: Joint velocity versus time with obstacle avoidance

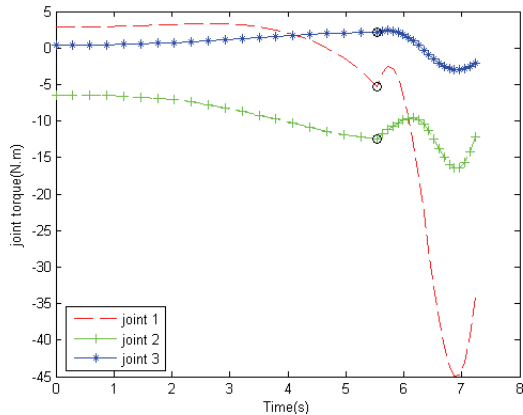


Figure 11: Joint torque versus time with obstacle avoidance

6. Simulation Results

This section presents the results of robot case study. This case consists on moving 3R robot arm form starting point ($x=0$ m, $y=2.3$ m, $q_g=80^\circ$) to final point ($x=-2$ m, $y=0$ m). The robot links have length of ($l_1=1$ m, $l_2=1$ m and $l_3=0.5$ m) and mass of ($m_1=1$ kg, $m_2=1$ kg and $m_3=0.5$ kg) the maximum allowed torques for joint 1, 2 and 3 of $\tau_{1\max}=45$ Nm, $\tau_{2\max}=20$ Nm and $\tau_{3\max}=5$ Nm, respectively. The joints velocity and acceleration of the initial and final configuration are assumed zeros. More over all robot joints are free rotate 2π . In the following case studies, the obstacle has circular shape with radius 0.35 m.

GA adopts a crossover probability $P_c=0.8$ per chromosome, a mutation probability $P_m=0.05$ per locus, a population of 200 elements for intermediate joints angle, joint velocity and traveling time of the arm, a string size $ss=9$ robot respectively, a 5-tournament selection scheme with elitism, and maximum generation $mg=80$. The weight factors set of fitness function is $[\beta_1, \beta_2, \beta_3, \beta_4]=[1, 2, 2, 1]$. At the initial generation of population, GA generates the chromosome elements with specified range, as following:

$$-\pi \leq q_i \leq +\pi \text{ rad } (i=1,2,3) \quad (34)$$

$$-\pi \leq q_g \leq +\pi \text{ rad} \quad (35)$$

$$-\pi/4 \leq \dot{q}_i \leq +\pi/4 \text{ rad/sec } (i=1,2,3) \quad (36)$$

$$0.1 \leq t_i \leq 8 \text{ sec } (i=1,2) \quad (37)$$

From figure 4 to figure 7, show the optimization results free workspace. When an obstacle found in the workspace

with coordinates($x=-0.5$, $y=1.8$), the optimized results are shown in figures 8 to 11.

Figure 4 shows the shorter Cartesian path. However, the straight line from the initial to final point is the shortest one, but is far from the best one according to the GA optimization result. Whereas figure 8 shows the ability of GA to decide, the parameters that generate the shorter Cartesian path with obstacle presence in the workspace with regard the other specified objective functions.

At each generation, GA chooses an adequate q_g . By final point coordinates and q_g , the joint angles of the final configuration can be evaluated by inverse kinematics of planar 3-link articulated robot [16]. As shown, the final tool orientation in figure 4 and 8 has been chosen according to the specified objective functions, therefore GA able to solve the kinematics redundancy in the absence and presence the obstacle in the workspace.

The black spots in figures 5 and 9 and figures 6 and 10 represent the optimized intermediate joint angle and joint velocity, respectively. The black spot in figures 7 and 9 represent the joint torque at the optimized joint angle and velocity. As shown in figures 7 and 9 the torque that calculated along the joint space trajectory in the case of free workspace is less than which results from case of obstacle existence workspace. However, in both cases, the joint torque does not exceed the maximum pre-defined torque. Since direct kinematics has proposed, tool-configuration matrix not used [12]. Therefore, singularity has been not concerned.

Table 1 shows the value of total traveling time, total joint traveling distance and Cartesian trajectory length by equations (31), (29) and (30) respectively, for both free and obstacle existence workspace.

Table 1: Optimization results

Result value	Free workspace	Obstacle existence workspace
Total traveling time (sec)	2.76	7.23
Total joint traveling distance (rad)	1.91	5.78
Total Cartesian trajectory length (m)	3.28	3.42

As noted from figure 12, the values of the total traveling time, total joint traveling distance and total Cartesian trajectory length of the obstacle existence are more than which are resulted from free work space. The amount of the increment makes the robot to be able to maneuver during its motion for avoiding the collision with the obstacle.

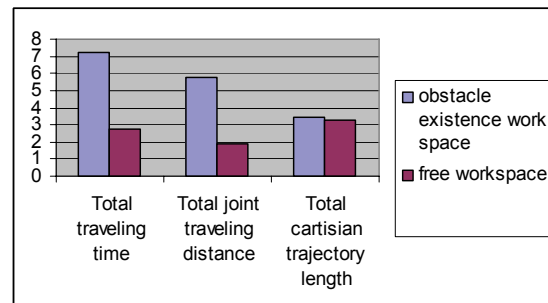


Figure 12: Results comparison between free and obstacle existence workspace

7. Conclusions

In the previous sections, the problem of the point-to-point trajectory planning was studied in detail. Trajectory planning method based on GA with specific objective functions was presented. Kinematics redundancy for the final configuration was considered as planning variable in the presented method. Case study of 3R planar robot showed that the method is effective, especially for avoiding the obstacle collision with the other objective functions. Since the proposed motion planning is based on the joint space, the total traveling time depends only on the joint traveling distance. The joint torque of the robot did not exceed its maximum pre-defined torque in both free and obstacle existence workspace case. Since GA uses the direct kinematics, the singularities do not constitute a problem. GA showed that it is able to achieve multi objective optimization efficiently. Finally, kinematics redundancy can be solved within GA according to the specified objective functions.

References

- [1] Zoltan Zoller, & Peter Zentan " Constant Kinetic Energy Robot Trajectory Planning ", PERIDICA POLYTECHNICA SER. MECH. ENG., Vol. 43, No.2, 213 – 228, 1999.
- [2] Zhe Tang, Changjiu Zhou, Zenqi Sun," Trajectory Planning For Smooth Transition Of A Biped Robot," IEEE International Conference on Robotic & Automation, Vol. 2, 2455-2460, Sept. 14 -19, 2003.
- [3] Dong Kyoung Chwa, Jungo Kang, Kihong Im, Jin Young Choi, " Robot Arm Trajectory Planning Using Missile Guidance Algorithm," SICE Annual Conference, vol. 2, pp. 2056-2061, August 4-6, 2003.
- [4] Devendra P. Garg, & Manish Kumar, "Optimization Techniques Applied To Multiple Manipulators for Path Planning and Torque Minimization", Engineering Applications of Artificial Intelligence, Volume 15, Number 3, June 2002 , pp. 241-252(12).
- [5] E.J. Solteiro Pires & J.A. Tenreiro Machado, " A Ga Perspective Of The Energy Requirement For Manipulators Maneuvering In A Workspace With Obstacles", Cec 2000- Congress On Evolutionary Computation , pp. 1110- 1116, 16-19 July 2000, Santiago, California, USA.
- [6] E.J. Solteiro Pires, Tenreiro Machado JA & De Moura Oliveira CR, "An Evolutionary Approach to Robot Structure and Trajectory Optimization", 10th IEEE-International Conference on Advanced Robotics, ICAR'01, pp. 333-338, 22-25 August, 2001, Budapest, Bulgaria.
- [7] S.G. Yue, D. Henrich, X. L. Xu, & S.K. Toss, "Point-to-Point Trajectory Planning of Flexible Redundant Robot Manipulators Using Genetic Algorithms", Journal of Robotica, vol 20, pp 269-280, 2002.
- [8] E.J. Solteriro Pires, J.A. Tenreiro Machado & P.B. Moura Oliveira, "Fractional Order Dynamic In A Genetic Algorithm", The 11th International Conference On Advanced Robotics, Colombia, Portugal, pp. 264 -269 June 30- July 3, 2003.
- [9] D. E. Goldberg, "Genetic Algorithm in Search, Optimization, and Machine Learning," Addison-Wiley, 1989.
- [10] Craig, J.J "Introduction to Robotics: Mechanics and Control", Addison- Wesley, 1989.
- [11] Dv Xin, Cher Hua -Hua, Gv Wei – Kang, "Neural Network And Genetic Algorithm Based Global Path Planning In A Static Environment", Journal Of Zhejiang University Science, Vol. 6A No. 6, 2005, 549- 554.
- [12] Schilling J., "Fundamentals of Robotics Analysis and Control," Prentice Hall, 1990.
- [13] Hartmut Pohlheim, "Geatbx Tutorial Genetic and Evolutionary Algorithm Toolbox for Use with Matlab," Version 3.5a, July 2004. Available at www.Geatbx.Com/
- [14] Fu, K.S., Gonzalez, R.C., and Lee, C.S.G "Robotics: Control, Sensing, Vision and Intelligence", McGraw Hill, 1987.
- [15] Asada and Slotine, "Robot Analysis and Control," John Wiley & Sons, Inc., 1976.
- [16] Lung-Wen T. "Robot Analysis, the Mechanism of Serial and Parallel Manipulators" John Wiley & Sons, Inc., 1999.

Experimental Investigation of Swirl-Stabilized Syngas Flames by Transverse Fuel Injection

A. Bouziane ^{a*}, A. Olivani ^b, A. Khalfi ^a, F. Cozzi ^b, A. Coghe ^b

^a Département de Génie Mécanique, Laboratoire de Matériaux et Systèmes Réactifs, Rue de Sétif, 19, 22000 Sidi bel abbés, Algérie.

^b Dipartimento di Energetica, Politecnico di Milano, via La Masa, 34, 20156 Milano, Italy

Abstract

Syngas offers a considerable opportunity for clean use of coal in power generation applications with potential decreasing of pollutant emissions. However, there are gaps in the fundamental understanding of syngas combustion characteristics and emissions. This paper reports an experimental preliminary investigation on the effects of different parameters inward the structure and emission characteristics of syngas non-premixed flames generated on an enclosed lean premixed swirl-stabilized combustor (input thermal power less to 20 kW) and equivalence ratio from 0.09 to 0.53 very lean flame giving interest to the behaviour of the syngas flame. The syngas fuel composition is a fixed mixture as 80 % H₂, 4 % CH₄, 10 % CO₂, 4 % CO and 2 % N₂. A qualitative analysis is carried out in let flame visualization by taking some direct photography to have more information about the flame. Measurements on NOx, CO emissions at the exhaust are undertaken by conventional gas analyzers. A comparison is made between syngas, GN (methane) and GN+ H₂ flame emissions. Results show that the burner operates under very lean condition (below $\Phi = 0.1$), NOx and CO emissions increase by decreasing the global equivalence ratio, and lower CO emission as compared to burning NG.

© 2008 Jordan Journal of Mechanical and Industrial Engineering. All rights reserved

Keywords: Swirl-stabilized flames; syngas; NOx; Turbulent combustion; Hydrogen;

Nomenclature

ext	: outer
min	: minute
NG	: Natural Gas
NI	: Normal liter
Re	: Reynolds number
r	: radius
S	: swirl number
U	: axial velocity
W	: tangential velocity, respectively,
ρ	: density
ϕ	: Global equivalence ratio
$U_{\text{air}}/d_{\text{burner}}$: Strain parameter,
\div	: varying

1. Introduction

The environment concern has prompted researchers towards a new consideration of alternative fuel sources for energy production such as extracted from the biomass. Syngas or synthetic gas formed through the gasification

process is expected to play an important role in future energy production. It represents a viable energy source, particularly for stationary power generation (IGCC systems) [1], since it allows for a large flexibility in fossil fuel sources, and since most of the soot emissions and pollutants can be removed in the post-gasification process prior to combustion. Further investigations are needed to characterize the behaviour of syngas flames information relating on the position of the reaction zone shape, luminosity etc... and their consequences on the pollutant emissions.

The use of the mixture hydrogen - hydrocarbon fuels such as natural gas show considerable promise as a method to improve flame stability during the lean combustion and, through its potential effect on flame chemistry, with the fact that the reactivity of fuel mixture increases[2][3],[4]. While a significant amount of fundamental understanding of flame propagation and stability characteristics of lean premixed systems has been gained in conventionally fuel natural gas-air systems, little is known about these issues for alternate gaseous fuels, such as syngas.

Numerous authors have focused their studies on the combustion and emission characteristics of non-premixed syngas-air mixtures. - Drake and Blint [5] numerically investigated the effect of stretch on thermal NO in laminar,

* Corresponding author. e-mail: alibouziane@yahoo.fr

counterflow CO/H₂/N₂ diffusion flames, and observed that NO concentration decreases dramatically as the flame stretch is increased. - Jurgen et al. [6] modelled and measured a 16 KW turbulent non-adiabatic syngas diffusion flame in a cooled cylindrical combustion chamber. Their calculated CO, CO₂, O₂, and NO concentrations compared well with measurements. - Chung and Williams [7] analyzed the structure and extinction of a CO/H₂/N₂ diffusion flame using an asymptotic approach with the kinetic scheme systematically reduced to the two-step mechanism, the water-gas shift, and hydrogen oxidation. It was shown that a three-step mechanism is needed to obtain a reasonably accurate description of the water-gas freezing. - Recently, Giles et al. [8] studied the NOx emission characteristics of counterflow syngas diffusion flames with air-stream dilutions at p = 1 atm. The results indicated that addition of methane in syngas decreases the peak flame temperature but increases prompt NO significantly.

Combustion and emission characteristics of premixed syngas-air mixtures have also been studied. - Alavandi and Agrawal [9] investigated experimentally the lean premixed combustion of CO/H₂/CH₄/air mixture, and observed that at a given flame temperature, the presence of CH₄ in a CO-H₂ mixture increases CO and NOx emissions. - Charlston-Goch et al. [10] reported measurement and computation of NO concentrations in premixed CO/H₂/CH₄/air flames for a range of equivalence ratios, fuel compositions, and strain rates at high pressures (p<11.9 atm). GRI 2.11 mechanism was observed to uniformly overpredict NO concentrations, and failed to predict key experimental trends. - Huang et al. [11] computed the laminar flame speeds of primary reference fuels and syngas mixtures and observed that the flame speed of hydrocarbon/air mixtures increases with a small addition of syngas, and that of syngas/air mixtures decrease dramatically with a small addition of hydrocarbon fuel. Saxena and Williams [12] developed a relatively small mechanism for CO/H₂ combustion. The mechanism was tested against the available data and some rate parameters were modified to obtain a new reduced mechanism. Natarajan J et al [13] Also reported measurement and computation of laminar flame speeds of H₂/CO/CO₂ mixtures over a range of fuel compositions, lean equivalence ratios, and reactant preheat temperatures. - Natarajan et al. [14] have reported the effects of syngas addition on the laminar flame speeds and flammability limits of n-butane and iso-butane flames.

This paper deals with preliminary investigation and highlights the need for experimental investigation of syngas flames in order to provide well-characterized measurements that can be used for the development and validation of simulation models, and extrapolate the present results in a turbulent non-premixed swirling reactor similar to many industrial combustion systems to gas turbines applications.

2. Experimental set-up

Schematic of set-up facility is shown in figure 1. It comprised laboratory-scale swirl burner; operating at ambient pressure, fired vertically upwards with flame

stabilized at the end of two co-centric pipes with the annulus supplying swirled air and the central pipe delivering the fuel mixture. Radial injection was obtained by closing the axial exit and inserting eight holes symmetrically distributed on the periphery of the pipe, just below the burner exit plane. The holes have the same total exit area of the nozzle and are located 3 mm upstream from the exit throat of the burner. Figure 2

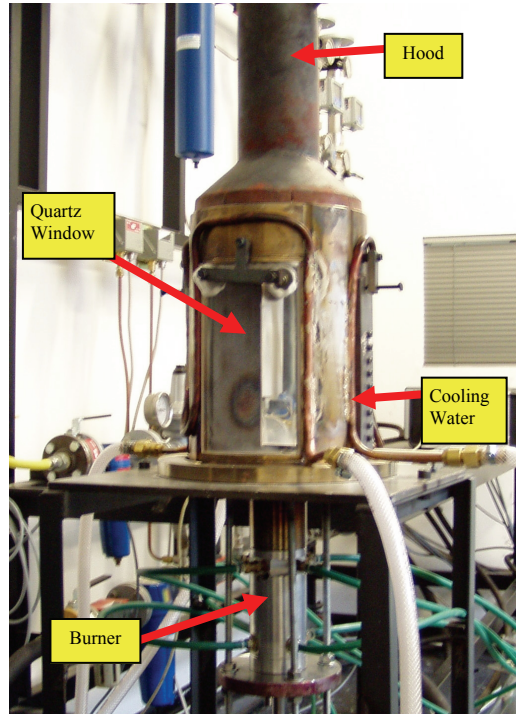


Figure 1: Burner – top view

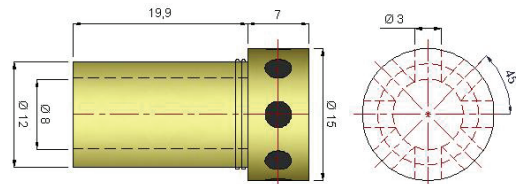
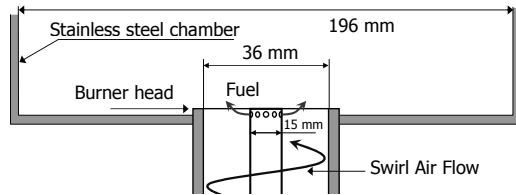


Figure 2: set-up facility

The co-flowing air stream was supplied through axial plus tangential inlet slots. The axial air entered through

four radial inlets in the cylindrical chamber and passed through a honeycomb flow straightener to produce a uniform axial stream. The tangential air was introduced through four tangential inlets to impart angular momentum, well upstream from the burner throat. The air was supplied by the laboratory air compressed line and was divided into two separately metered streams to allow continuous control and regulation of the swirl strength at the burner exit. The tangential and axial air and the fuel flow-rates were metered and stabilized by calibrated thermal mass flow-meters and controllers. Since syngas mixtures are mixed 300 mm upstream the combustion chamber inlet, the fuel manifold design ensures uniform mixing of the three fuels before the two mixtures is injected in the combustion chamber. Figure 3

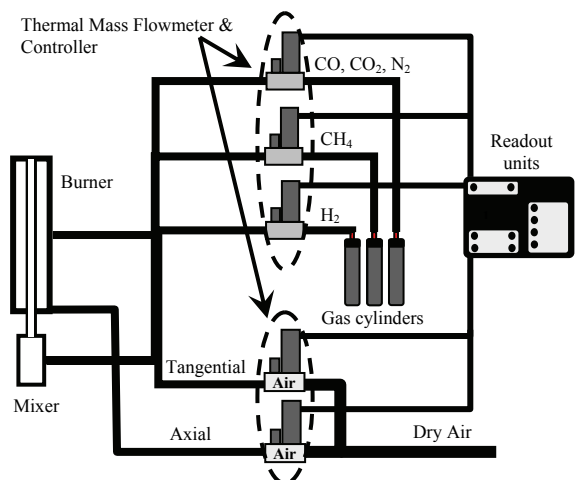


Figure 3: Schematic of fuel blending system

The fuel jet Reynolds number Re based on the fuel nozzle diameter (8 mm) was estimated at ambient temperature by using the dynamic viscosity calculated from a polynomial fit of the experimental data (at 300K) of Nabizadeh et al. [15]. Fuel mixture density, ρ_{fuel} , was computed by the weighted mean of natural gas and hydrogen densities with volumetric fractions as weights. The swirl number, S , of the air stream was estimated according to the definition of Gupta et al.[16] and neglecting the pressure and the turbulent stresses terms:

$$S = \left(\int_0^{r_{ext}} \rho_{air} U W r^2 dr \right) / r_{ext} \left(\int_0^{r_{ext}} \rho_{air} U^2 dr \right) \quad (1)$$

Where ρ_{air} is the air density, U and W , respectively, are the axial and tangential velocities, while r_{ext} is the outer radius of the burner air annulus. The values of Swirl number S , Reynolds number R , and all the other relevant experimental test conditions are listed in Table 1.

Table 1: Operating conditions of experimental tests

Air flow rate	(NL/min)	440
Swirl number:		0.82
Reynolds Number:		21000
Syngas flow rate	(NL/min)	11.4 ÷ 111.4
Global equivalence ratio:		0.06 ÷ 0.6
Input Thermal Power: (kW)		2.0 ÷ 19.5
NG+H2 flow rate	(NL/min)	32

H2 molar fraction	100 % - 0 %
Global equivalence ratio:	0.18 ÷ 0.72
Input Thermal Power: (kW)	5.4 ÷ 19.8

NG flow rate	(NL/min)	28 ÷ 44
Global equivalence ratio:		0.62 ÷ 0.98
Input Thermal Power: (kW)		17.3 ÷ 27.2

The burner was operated at atmospheric pressure and nominal inlet gas temperature of 300 K, in lean conditions. The syngas fuel composition is fixed mixtures as 80 % H_2 , 4 % CH_4 , 10 % CO_2 , 2 % CO and 1 % N_2 .

For temperature measurements at the exhaust of the combustion chamber, thermocouple mechanics are performed by using FLUKE 80PK-24. The measurements are based on Seebeck effect. A qualitative analysis of the flame structure is achieved by imaging the spontaneous flame by using Digitale Olympus Camedia C-720. Burned gases are sampled at the exhaust of the combustion chamber for analysis.

The sampling probe is placed in the center of the exhaust collection pipe, where the combustion products composition is invariant. The gas sample is exhausted through the probe and the sampling system by a pump. A dryer and filter remove the moisture and particles then a constant supply of clean dry combustion gases is delivered to each instruments through a manifold to give species concentrations on dry basis. A chemiluminescence analyser is used to measure the concentration of NO_x . The chemiluminescent method used in analyser is based upon the chemiluminiscent gas phase reaction between O_3 and NO . Then, two non-dispersive infrared (NDIR) analysers are used to measure CO. The technique is based on the infrared absorption characteristics of gases. The gas analyser is calibrated with certified standards mixtures of known composition. Zero and span calibration are performed before and after each test point measurements, to minimize the influence of instrument drift.

3. Results and Discussion

A specific parameter is introduced when swirl flame is considered, as we identify by strain parameter, designed by the ratio of air velocity to air tube diameter. When this parameter increases the air velocity increases too and the flame is destabilized. As we can observe on figure 4, the stability limit is more pronounced when hydrogen is added to the fuel. According to the work of Schefer et al [17] important quantities are affected when hydrogen is added to hydrocarbon fuels, both chemical and physical process occurring in flames are altered and attributed the stability improvement to the increase of OH level in the reaction zone. These changes affect flame stability, combustor acoustics, pollutant emissions and so on. Also, Feikema et al [18] noted that the blowout and the stability region are designed as function of global equivalence ratio ϕ and strain parameter and suggested that the increase in the laminar burning velocity as being responsible for the improved flame stability. Enhancement in flame stability is expected when hydrogen is added to a lean natural gas flame. Swirl burner operates at very lean equivalence ratio when fed with fuel mixture of Natural Gas + H_2 . - Figure 4 [19] points out for a wide stability region, expected when

burning Syngas mixture (80% H₂) at low global equivalence ratio ϕ .

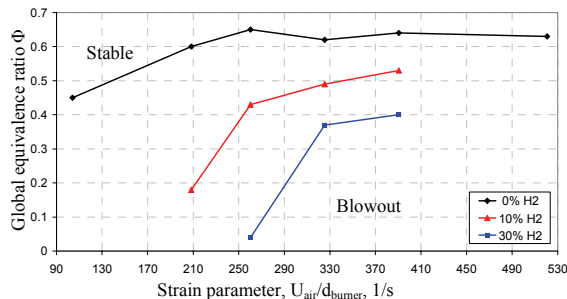


Figure 4: Stability regions for NG+H₂, taken from [16]

Direct luminous photographs of the flame were obtained to gain an understanding of the flame structure (location and size). All images on figures 5 show typical structure of confined swirl flames. With varying global equivalence ratio ϕ , the flame morphology looks different. However, the main flame structure and also brightness are governed by this parameter. - ϕ varying from 0.09 to 0.29, the flame size and shape were qualitatively similar figure 5 a - b. The visible flame emission is blue. - When $\phi = 0.39$ more brightness is apparent on the figure 5-c and 1-d and the flame emission became blue/violet, more luminous in direction of flux zone is noted, assent the incandescence to the gas gun; which indicates efficient mixing, as we observe the penetration of the fuel jet into the recirculation zone. The luminous part of the flame became brighter on figure 5-c. When fuel flow rate increases, flame size increases qualitatively seems to be mainly due to the increase of the global equivalence ratio and input thermal power figure 5, c-d. Flame appearance changes because of the higher fuel jets velocities. The transverse injection plays an important role on flame stabilization and on the flame shape. On previous work on NG + H₂ and NG flame, it was observed that in the case of transverse injection typology, as we recognized in swirling flow by central toroidal recirculation zone (CTRZ) engendered by the swirl motion, appears more pronounced; the penetration of the fuel jet into the recirculation zone is more efficient than the axial injection, assents to the flame to progress near the gas gun and to appear more compact and symmetric. The same behavior is observed on the syngas flame. A luminous blue region is apparent on the images indicating that the flame structure is characterized by two spatially separated reaction zones : - one is located downstream of the centerbody; an intense reaction zone probably due to the larger diffusivity and the higher laminar burning velocity of hydrogen. - The second one referred to the corner toroidal zone [20] with the higher luminous flame emission near the burner; could be due to hydrogen oxidation and enhances the natural gas oxidation. For the same condition, the location where both chemical reactions and heat release take place is indicated by the wide blue region; above this region and on the burner axis a weak yellow flame, synonym of soot trace, appearing on obvious work (axial injection typology in NG and NG + H₂) is not visible on these pictures. Reaction zone structures of turbulent hydrogen flames are different than those of hydrocarbon flames (NG).

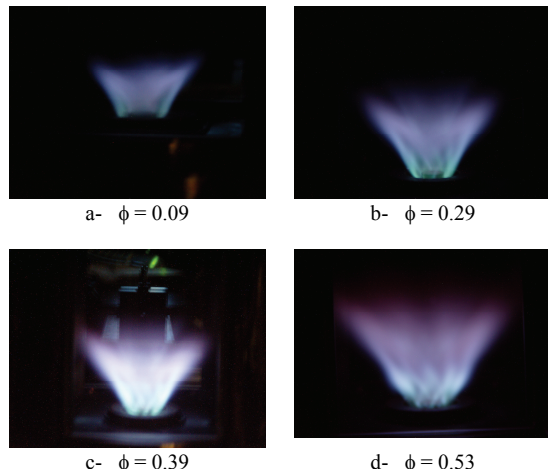


Figure 5: Direct flame luminosity photographs in swirl-stabilized burner

The measured adiabatic temperature profiles are shown in Figure 6. As we can see the temperature profile for each three fuels is quasi linear with increase of global equivalence ratio.

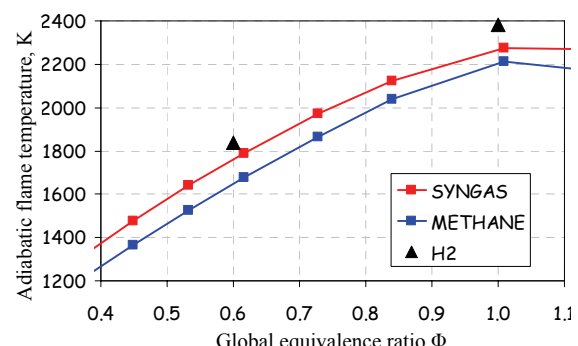


Figure 6: Measured adiabatic temperature of the three fuels

A peak temperature is clearly visible in the profile at stoichiometric condition for the NG + H₂ fuels. The results generally revealed a rapid temperature increase for all mixtures. The adiabatic temperature profiles are strongly affected by the equivalence ratio. The higher temperature is attributed to the hydrogen fuels and can be associated to the penetration of the fuel jet when hydrogen is added to the mixture combined to transverse injection.

3.1. 3.1. Pollutants Emission

To study the relation on the syngas flames and pollutants emissions, measurements are taken at the exhaust of the combustion chamber. Thus far, flame pictures evidence the disappearing of yellow luminous plume related to trace of soot; a phenomenon totally absent in the case of radial injection. Furthermore, in case of axial injection (not in this paper) it has been observed the intermittent formation of a central sooting luminous plume.

3.2. CO Emission

Figure 7 shows the comparison of CO emissions for the three fuels mixtures. For Natural Gas (NG), CO emissions has a minimum at $\phi = 0.85$, then increases when approaching blowout condition at $\phi \sim 0.6$. For Fuel mixture (NG/H₂), up to 75% of H₂, CO emissions increase as ϕ decreases (quenching of CO oxidation) and above 75% of H₂, the CO emissions decrease with ϕ (carbon fraction in fuel mixture decreases). When Syngas fuel mixture is expected, CO emissions increase as ϕ decreases. At increasing Hydrogen content in NG/H₂ fuel mixture, we noted that CO emissions increase and reach a maximum for 70 % of hydrogen in the mixture; after the maximum, CO emissions decrease. This behaviour is correlated to the quenching of CO oxidation to CO₂ stimulated by two phenomena: appropriate to the presence of hydrogen in the mixture, the reduction in the size of reaction zone is established, then reduction in residence time of combustion product. As reported in hydrocarbon oxidation when experimental consideration is designed, the oxidation of CO to CO₂ comes late in the reaction process; consequently the complete conversion of CO to CO₂ doesn't carry out. Then at low hydrogen percentage, CO concentration increase related to this phenomenon. When high hydrogen content is considered in the mixture, CO emissions decrease, due to the decrease in the total carbon input in the fuel mixture and permits increase in the excess of air.

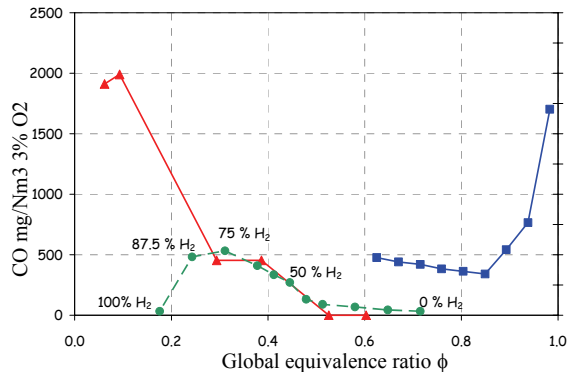


Figure 7: Carbon monoxide emissions as a function of equivalence ratio; ■ Natural Gas (NG), ▲ NG+H₂, ● SYNGAS

In the work of Schefer et al, a reduction in CO formation was also observed in a swirled stabilized premixed burner, whereas Choudhuri and Gollahalli [5] noted that a reduction in CO was observed on a diffusion turbulent flame when hydrogen was added to the fuel, relating that the OH and O radicals contribute to the pyrolysis of the carbon species. Then, the reduction in CO emissions with hydrogen addition was also attributed to the increased in radical pool. Higher OH concentrations are likely to promote completion of CO oxidation to CO₂ via the OH radical.

3.3. NO_x Emission

Figure 8 shows the comparison of the NO_x emissions for the three different fuels, at varying global equivalence ratio. In our burner, it was observed that NO_x and CO

fractions in the exhaust gases increased as the hydrogen content in the fuel increased. When the hydrogen content in the fuel mixture reached 80%, maximum emissions of CO and NO_x were attained.

A reduction of the equivalence ratio gives rise to decrease in NO_x emissions in NG, but an increase in syngas. The differences observed in the two profiles may be explained by NO_x emission in NG strongly influenced by swirl intensity and injection typology, radial burner at this case: the fluid dynamic approach is useful to explain this trend, the reverse flow is more pronounced in radial injection, carrying hot combustion products, then flame structure is more compact and very low in comparing to the axial injection, then enhances the mixing process, consequently the temperature is affected. When syngas fuel is considered, the flame stability parameter is preponderant related to the structure of the flame generated, decreasing the stability limit of the flame, allowed the increase in the co-centric air velocity and affected the flame size

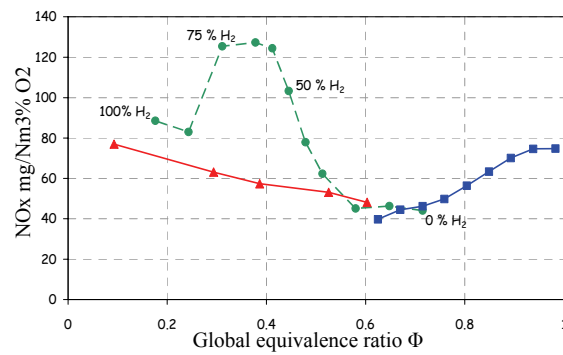


Figure 8: NO_x emissions as a function of equivalence ratio; ■ Natural Gas (NG), ▲ NG+H₂, ● SYNGAS

This condition verified by numerous authors, forced to reduce the residence times for the production of NO_x. At $\phi = 0.6$ (Pth ~ 20 kW) Syngas, NG+H₂ and NG have similar NO_x emission. To investigate possible reasons for this statement, response is given by the measurement of the adiabatic temperature profile; that exhibit at this point ($\phi = 0.6$) temperature is less similar to the three mixtures. In addition, it is known that thermal NO_x formation is temperature dependent; the increase in the thermal NO_x may justify the higher NO_x level measured. Non-monotonic trend is noted for the NO_x emission for NG+H₂ when the global ϕ decreases.

4. Conclusions and Future Work

Syngas combustion in a swirl stabilized burner was investigated, and the effect of burning was analyzed by carried out flame stability, (at overall lean condition) and pollutant emissions. Syngas Fuel mixtures containing a (4% CH₄, 4% CO, 10% CO₂, 2 %N₂, 80% H₂) have been burned at ambient pressure in a confined environment by transverse injection and direct photography was taken. The investigated turbulent flame with co-flow injection of the reactants revealed significant differences in NO_x and CO emissions comparing to other fuels, which may be ascribed to the observed changes in the flame structure. Though,

NOx emissions scale with adiabatic flame temperature; the main outcomes of the present preliminary investigation were the followings: the burner operates under very lean condition (below $\phi = 0.1$), NOx and CO emissions increases by decreasing the global equivalence ratio, lower CO emission as compared to burning NG alone (at $\phi = 0.6$) and lower NOx emissions as compared to burning NG+H₂. Thus, an important result from the present study pertains to the existence of an optimum syngas composition that yields the lowest amount of NOx in syngas. In order to get a deeper understanding of the above described phenomena a future work will focussed on: further investigation of lean conditions and their effect on CO and NOx emissions, investigate flow field and the influence of jets velocities and it will be interesting to test the syngas flame on different fuel injection typologies.

Acknowledgement

Algerian Government and Italian Ministry of University and Research supported this research. The experimental work has been performed at the Combustion laboratory at Politecnico di Milano- Italy.

References

- [1] Kay Damen, Martijn van Troost, Andre' Faaij, Wim Turkenburg, "A comparison of electricity and hydrogen production systems with CO₂ capture and storage." Part A: Review and selection of promising conversion and capture technologies. *Progress in Energy and Combustion Science*, Vol. 32, 2006, 215–246.
- [2] R.W. Schefer, "Hydrogen enrichment for improved lean flame stability." *International Journal of Hydrogen Energy*, Vol. 28, 2003, 1131 – 1141.
- [3] R.W. Schefer, W.G. Houfa, B. Bourneb, J. Coltonb, "Spatial, and radiative properties of an open-flame hydrogen plume." *International Journal of Hydrogen Energy*, Vol.31, 2006, 1332 – 1340.
- [4] F. Cozzi, A. Coghe, "Behavior of hydrogen-enriched non-premixed swirled natural gas flames." *International Journal of Hydrogen Energy*, Vol. 31, 2006, 669 – 677.
- [5] Drake MC, Blint RJ., "Thermal NOx in stretched laminar opposed flow diffusion flames with CO/H₂/N₂ fuel." *Combust Flame*, Vol.76, 1989, 151–167.
- [6] Jurgen JJL, Jim BWK, Sikke AK., "Modeling and measurements of a 16-kW turbulent nonadiabatic syngas diffusion flame in a cooled cylindrical combustion chamber." *Combust Flame*, Vol. 125, 2001, 1012–1031.
- [7] Chung SH, Williams FA, "Asymptotic structure, and extinction of CO-H₂ diffusion flames with reduced kinetic mechanisms." *Combust Flame*, Vol. 82, 1990, 389–410.
- [8] Giles DG, Som S, Aggarwal SK., "NOx emission characteristics of counterflow syngas diffusion flames with airstream dilution." *Fuel*, Vol. 85, 2006, 1729–1742.
- [9] Charlston-Goch D, Chadwick BL, Morrison RJS, Campisi A, Thomsen DD, Laurendeau NM., "Laser-induced fluorescence measurements and modelling of nitric oxide in premixed flames of CO + H₂ + CH₄ and air at high pressures: I. Nitrogen fixation". *Combust Flame*, Vol. 125, 2001, 729–743.
- [10] Huang Y, Sung CJ, Eng JA., "Laminar flame speeds of primary reference fuels and reformer gas mixtures." *Combust Flame*, Vol. 139, 2004, 239–251.
- [11] Saxena P, Williams FA., "Testing a small detailed chemical-kinetic mechanism for the combustion of hydrogen and carbon monoxide." *Combust Flame*, Vol. 145, 2006, 316–323.
- [12] Natarajan J, Lieuwen T, Seitzman JM., "Laminar speeds of synthetic gas fuel mixtures." Paper GT2005-68917. ASME-IGTI Turbo Expo, Reno, Nevada, 2005.
- [13] Sun HY, Yang SI, Jomaas G, Law CK., "High-pressure laminar flame speeds and kinetic modeling of carbon monoxide/hydrogen combustion. Proceedings of the Combustion Institute. Vol. 31. 2007, 439–446
- [14] Alavandi SK, Agrawal AK., "Lean premixed combustion of carbon monoxide–hydrogen–methane fuel mixtures using porous inert media." Paper GT2005-68586. ASME Turbo Expo 2005. Reno, Nevada, 2005.
- [15] Nabizadeh H, Mayinger F., "Viscosity of binary mixtures of hydrogen and natural gas (Hythane) in the gaseous phase." 15th European Conference on Thermo physical Properties. Würzburg, Germany, 1999.
- [16] Gupta AK, Lilley DG, Syred N. *Swirl flows*. Tunbridge Wells: Abacus Press; 1984.
- [17] R.W. ScheferW.G. Houfa, B. Bourneb, J. Coltonb, "Spatial and radiative properties of an open-flame hydrogen plume." *International Journal of Hydrogen Energy*, Vol. 31, 2006, 1332 – 1340.
- [18] Feikema D, Cheng RH, Driscoll JF., "Blowout of nonpremixed flames: maximum coaxial air velocities achievable, with and without swirl." *Combust Flame*, Vol.86, 1991, 347–358.
- [19] Andrea Olivani, Giulio Solero, Fabio Cozzi, Aldo Coghe, "Near field flow structure of isothermal swirling flows and reacting non-premixed swirling flames". Experimental 4th Mediterranean Combustion Symposium, Lisbon, Portugal 2005.
- [20] David R. Noble, Qingguo Zhang, Akbar Shareef, Jeremiah Tootle, Andrew Meyers, Tim Lieuwen. "Syngas Mixture Composition Effects upon Flaschback and Blowout". Proceedings of GT2006 ASME Turbo Expo 2006: Power for Land, Sea and Air May Barcelona, Spain, 2006.

Analysis of Longitudinal Aerodynamic Characteristics of an Aircraft Model with and Without Winglet

Altab Hossain ^a*, Prithvi Raj Arora ^b, Ataur Rahman ^c, Abdul Aziz Jaafar ^b,
 A.K.M. Parvez Iqbal ^a

^a*Department of Mechanical Engineering, University Industry Selangor, Jln Timur Tambahan, 45600 Batang Berjuntai, Selangor Darul Ehsan, Malaysia*

^b*Department of Aerospace Engineering, University Putra Malaysia, Malaysia*

^c*Department of Mechanical Engineering, International Islamic University Malaysia*

Abstract

This paper describes the influences of two pair of elliptical and circular shaped winglets with the wing of the aircraft model for the reduction of induced drag without increasing the span of the aircraft. Aerodynamic characteristics for the model aircraft wing with NACA section No. 65-3-218 with and without elliptical and circular winglets have been studied using a subsonic wind tunnel of $1\text{m} \times 1\text{m}$ rectangular test section. Lift and drag measurements are carried out using a six component external balance. Tests are carried out on the aircraft model with and without winglet at the Reynolds numbers 0.17×10^6 , 0.21×10^6 and 0.25×10^6 . The experimental results show that lift curve slope increases by 1-6% with the addition of certain winglet configurations and at the same time, the drag decreases by 20-28% as compared to the aircraft model with and without winglet for the maximum Reynolds number considered in the present study. The experimental approach and a summary of the main findings are presented.

© 2008 Jordan Journal of Mechanical and Industrial Engineering. All rights reserved

Keywords: Winglet; Induced drag; External balance; Lift curve slope;

Nomenclature

α	: Angle-of-attack
D	: Drag force
L	: Lift force
ρ_∞	: Air density
S	: Reference area
V_∞	: Free stream velocity
a_0	: Lift slope
C_D	: Drag coefficient
C_L	: Lift coefficient
d	: Diameter of sphere
$[K_{ij}]$: Coefficient matrix

1. Introduction

For a number of years many investigations have been carried out to prove the possible benefits of modifying wing tip flow. The aerodynamic performance of an aircraft can be improved by a wingtip device which diffuses the

strong vortices produced at the tip and thereby optimise the span wise lift distribution, while maintaining the additional moments on the wing within certain limits. For this purpose the researchers have been doing experiments to produce favorable effects of the flow field using wing tip and reducing the strength of the trailing vortex with the aid of wingtip devices, e.g., winglets, wing tips of complex plan-form, sails, and various modifications of the wingtip side edge. The winglet is cambered and twisted so that the rotating vortex flow at the wing tip creates a lift force on the winglet.

From the beginning of aviation era, designers were searching for methods and technologies for reducing the required fuel consumption of the commercial aircraft. Wingtip devices aimed at the reduction of induced drag, which was responsible for 30-40% of the total drag of a transport-aircraft at long-range cruise condition and for considerably downgrading the climb performance of an aircraft [1]. Winglet alongside with tip tanks, raked wingtips, and aligned fans are belonged to this class of devices.

Modern interest in winglets spans the last 25 years. In July 1976, Richard Whitcomb of NASA Langley Research Centre published a general design approach that

* Corresponding author. e-mail: altab75@unisel.edu.my

summarized the aerodynamic technology involved in winglet design. Small and nearly vertical fins were installed on a KC-135A and flights were tested in 1979 and 1980 [2-3]. Whitcomb showed that winglets could increase an aircraft's range by as much as 7% at cruise speeds. A NASA contract [4] in the 1980s assessed winglets and other drag reduction devices, and they found that wingtip devices (winglet, feathers, sails, etc.) could reduce induced drag by 10 to 15% if they are designed as an integral part of the wing.

The "spiroid" wingtip [5] produces a reduction in induced drag at the same time blended winglet [6] reduces drag by eliminating the discontinuity between the wing tip and the winglet. A smoothed version is used on the gently upswpt winglet of the Boeing 737-400. Boeing Business Jets and Aviation Partners, Inc. have embarked upon a cooperative program to market conventional winglets for retrofit to the Boeing 7xx series of jetliners. Flight tests on the Boeing Business Jet 737-400 resulted in a 7% drag reduction. Theoretical predictions had indicated that the configuration would have only a 1-2% improvement of drag reduction, and wind tunnel tests had shown only 2% drag reduction [7]. This indicates that wind tunnel test results of winglet configurations should be reviewed with some caution.

Jones [8] investigated the advantages of single winglets for small transport aircraft, on which they can provide 10% reduction in induced drag compared with elliptical wings. Winglets are being incorporated into most new transport aircraft, including the Gulf stream III and IV business jets [9], the Boeing 747-400 and McDonnell Douglas MD-11 airliners, and the McDonnell Douglas C-17 military transport. The first industry application of the winglet concept was in wingtip sail. The Pennsylvania State University (PSU) 94-097 airfoil has been designed for use on winglets of high-performance sailplanes [10]. To validate the design codes, as well as the design itself, the airfoil was tested in the Penn State Low-Speed, Low-Turbulence Wind Tunnel from Reynolds numbers of 0.24×10^6 to 1.0×10^6 . Performance predictions from two well-known computer codes are compared to the data obtained experimentally, and both are found to generate results that are in good agreement with the wind tunnel measurements.

J. J. Spillman at the Cranfield Institute of Technology in England [11] carried out another investigation on wing tip airfoils. He investigated the use of one to four sails on the wingtip fuel tank of a Paris MS 760 Trainer Aircraft. The flight test results confirmed the wind tunnel test results, demonstrated shorter takeoff rolls, and reduced fuel consumption [12]. Spillman later investigated wingtip vortex reduction due to wing tip sails, and found lower vortex energy 400-700 m behind the aircraft, although the rate of decay beyond that was somewhat lower [13].

There has been limited investigation of multiple winglets for aircraft. The split-tip design [14] by Heinz Klug for an aircraft wing is considered a primitive multiple winglets that was created to exploit the non-planar wake geometry by reducing induced drag and wing stress. A biologist with an aerodynamic background has done extensive investigation of the split wingtips of soaring birds and he demonstrated that the tip slots of soaring birds reduce induced drag and increase the span factor of the

wings [15]. He found remarkable improvements of slotted wingtips compared with conventional wing with a Clark Y airfoil and he investigated that with the same increase in angle of attack, the Clark Y airfoil tip increased the base wing drag by 25%, while the feathered tip actually reduced the drag by 6%.

To improve the performance of a wing, the multi-winglet [16] design was evaluated to demonstrate its advanced performance potential over the baseline wing and an equivalent single winglet. The results show that certain multi-winglet configurations reduced the wing induced drag and improved L/D by 15-30% compared with the NACA 0012 wing section. In Europe, an extension to the wing tip airfoils has been developed called Wing-Grid [17]. Wing-Grid is a set of multiple wing extensions added to the wing. These small wings are added at various angles so that their tip vortices do not interact to form a strong vortex. These smaller vortices dissipate the vortex energy so that the lift distribution is modified and the induced drag of the wing is reduced. However, this concept is limited, since it is not able to change configuration in flight to optimise drag reduction.

Aerodynamic characteristics for the aircraft model with and without winglet having wing with NACA section No. 65-3-218 has been presented in this paper. The study on the enhanced performance of the aircraft models is also given by incorporating elliptical and circular winglets. An interaction matrix method has also been presented to revalidate the calibration matrix data provided by the manufacturer of the six-component external balance. The calibration of free stream velocity and flow quality in the test section has been established and documented.

2. Methodology

2.1. Speed calibration

Subsonic wind tunnel of 2.5m length, 1m width and 1m height rectangular test section at the Aerodynamics Laboratory of the Aerospace Engineering Department, University Putra Malaysia is used for carrying out the experiments. The ambient pressure, temperature and humidity are recorded using barometer, thermometer, and hygrometer respectively for the evaluation of air density in the laboratory environment.

The RPM controller of the wind tunnel controls the airflow velocity. For the different Hz settings at the RPM controller, the flow velocities in wind tunnel test section are recorded using six-component external balance software. In addition to this dynamic pressure at the picot, tube is recorded with digital manometer and corresponding velocities are calculated [18] (see Table 1).

The validity of the digital manometer was confirmed by comparing the dynamic pressure measured through the digital manometer and through the tube manometer used along with the picot tube mounted in the test section. The flow velocity versus RPM controller speed curves is plotted for the data obtained through six components external balance software, digital manometer and tube manometer and are given in Fig. Least square fit lines are

drawn through the data and the corresponding lines are given in Fig.

Table 1: Speed calibration data

S. No.	Hz	Free stream flow velocity (m/s)		
		External balance software	Digital manometer	Manometer tube
1	0.0	0.00	0.00	0.00
2	3.0	1.93	2.21	2.70
3	5.0	3.87	3.69	4.04
4	7.5	6.40	6.72	6.67
5	10.0	9.07	9.42	9.30
6	12.5	11.60	12.06	12.07
7	15.0	14.03	14.76	14.77
8	17.5	16.50	17.35	17.42
9	20.0	18.83	20.08	20.15
10	22.5	21.17	22.65	22.82
11	25.0	23.50	25.17	25.45
12	27.5	25.80	27.65	28.00
13	30.0	27.93	30.20	30.41

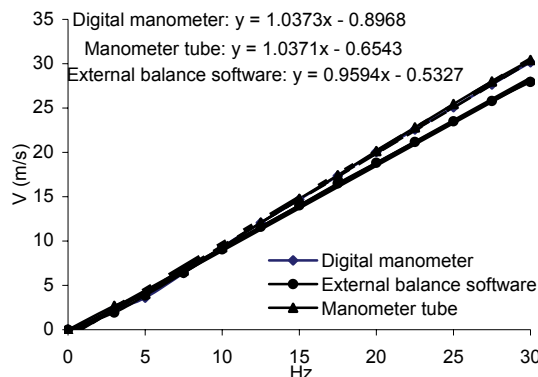


Figure 1: Free stream velocity versus RPM controller speed.

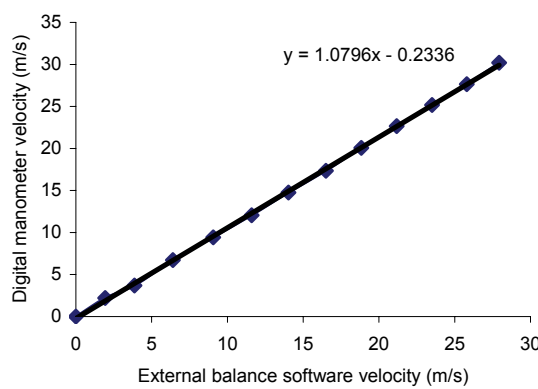


Figure 2: Flow velocity calibration for external balance

It is observed that the curves for the digital manometer and the tube manometer readings are practically the same whereas the curve for the data using six-component external balance software deviates a little from the other two curves. The experimental error using the external balance is nearly 6%. The flow velocity readings of the external balance are corrected through the following

calibration equation obtained through the data shown in Fig.,

$$y = 1.0796x - 0.2336 \quad (1)$$

Where x denotes external balance software velocity (m/s) and y denotes digital manometer velocity (m/s). Using the equation (1), the actual value of free stream air velocity will be 21.36 m/s for corresponding 20 m/s of air velocity from six-component external balance software.

2.2. Flow Uniformity

The dynamic pressure is measured using digital manometer at different locations in the test section (see Fig. 3) in YZ-plane by means of a picot tube for a RPM controller setting of 15 Hz. For different locations of the measurement grid, the experiments are repeated three times and the experimental data is given in Table 2. The average (mean) dynamic pressure is obtained from the measured dynamic pressure and is given in the last column of Table 2. The dynamic pressure variations from the mean are calculated in percentage at different locations of YZ-plane and are given in Table 3. Using these data, dynamic pressure variations from the mean (percentage) versus distance from wind tunnel floor (cm) are plotted in Figure 4. From figure-4 it is observed that the variation of dynamic pressure in the test section is within $\pm 0.5\%$ which indicates that the there is very good uniformity of flow in the test section of the wind tunnel.

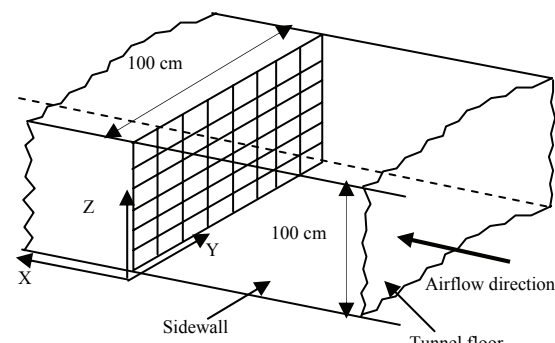


Figure 3: Schematic view of the wind tunnel test section

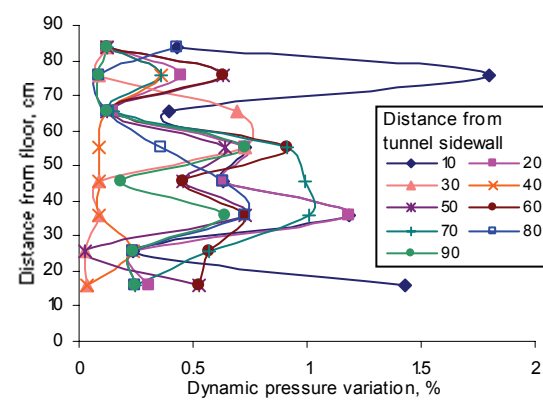


Figure 4: Dynamic pressure variation in the wind tunnel test section.

Table 2: Dynamic pressure at a cross section of the wind tunnel test section.

S. No	Z-axis (Down) [cm]	Dynamic pressure [Pa]									
		Distance from wall (Y-axis) [cm]									
		10	20	30	40	50	60	70	80	90	Mean
1	83.5	121.67	121.00	121.00	121.00	121.00	121.00	121.00	121.67	121.00	121.15
2	75.5	126.00	124.33	123.67	123.33	123.00	123.00	123.33	123.67	123.67	123.78
3	65.5	123.67	123.00	122.33	123.33	123.33	123.33	123.00	123.33	123.33	123.19
4	55.5	123.00	123.00	123.00	122.00	121.33	121.00	121.00	121.67	123.00	122.11
5	45.8	123.67	123.67	123.00	123.00	122.33	122.33	121.67	123.67	122.67	122.89
6	35.8	123.00	123.00	121.67	121.67	120.67	120.67	120.33	120.67	122.33	121.56
7	25.8	124.00	124.00	123.67	124.00	123.67	123.00	123.00	124.00	124.00	123.70
8	16.0	121.00	119.67	119.33	119.33	118.67	118.67	119.00	119.00	119.00	119.30

Table 3: Dynamic pressure variation at a cross section of the wind tunnel test section.

S. No	Z-axis (Down) [cm]	Dynamic pressure variation [%]									
		Distance from wall (Y-axis) [cm]									
		10	20	30	40	50	60	70	80	90	Mean
1	83.5	0.43	0.12	0.12	0.12	0.12	0.12	0.12	0.43	0.12	0.2
2	75.5	1.80	0.45	0.09	0.36	0.63	0.63	0.36	0.09	0.09	0.5
3	65.5	0.39	0.15	0.69	0.12	0.12	0.12	0.15	0.12	0.12	0.2
4	55.5	0.73	0.73	0.73	0.09	0.64	0.91	0.91	0.36	0.73	0.6
5	45.8	0.63	0.63	0.09	0.09	0.45	0.45	0.99	0.63	0.18	0.5
6	35.8	1.19	1.19	0.09	0.09	0.73	0.73	1.01	0.73	0.64	0.7
7	25.8	0.24	0.24	0.03	0.24	0.03	0.57	0.57	0.24	0.24	0.3
8	16.0	1.43	0.31	0.03	0.03	0.53	0.53	0.25	0.25	0.25	0.4

2.3. Wind Tunnel Model details and Instrumentation

The wind tunnel test aircraft model consists of rectangular wing with NACA section No. 65-3-218-aerofoil 0.66 m span and a 0.121 m chord. Two sets of elliptical and circular shaped winglets were designed of wood for the above wing. Figure-5 shows a photograph of the model aircraft with winglet, which is mounted horizontally in the test section of the wind tunnel.



Figure 5: Aircraft model check for 0° angle of attack.

The tests were carried out with free-stream velocities of 21.36 m/s, 26.76 m/s, and 32.15 m/s respectively with and without winglet of different configurations. The ambient pressure, temperature and humidity were recorded using barometer, thermometer, and hygrometer respectively for the evaluation of air density in the laboratory environment. Longitudinal tests were carried out at an angle of attack

ranging from zero degree to 14 degrees with an increment of 2 degrees. The coefficient of lift (Table 4), coefficient of drag (Table 5), the ratio of lift/drags (Table 6) and lift curve slopes data (Table 7) are obtained from the experimental results as per the procedure explained in [18-19].

2.4. Calibration of the Balance

Calibration of the six-component balance has been done to check the calibration matrix data provided by the manufacturer. Figure 6 shows a photograph of the calibration rig used for the validation of calibration matrix, which is mounted on the upper platform of the balance in place of model.

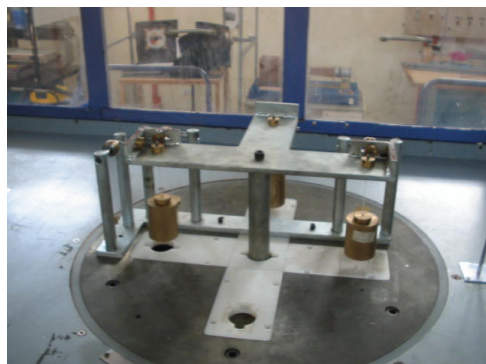


Figure 6: Calibration rig mounted on the floor of the wind tunnel test section

Table 4: Lift coefficients experimental data

S. No.	Winglet Configuration	Reynolds Number [10 ⁶]	Lift coefficient, C _L		
			Initial Angle of Attack [0°]	Stall Angle of Attack [8°]	Final Angle of Attack [14°]
1	Without Winglet	0.17	0.237	0.805	0.657
		0.21	0.259	0.817	0.584
		0.25	0.306	0.879	0.733
2	Elliptical Winglet, Configuration 1 (0° angle)	0.17	0.299	0.829	0.641
		0.21	0.327	0.889	0.700
		0.25	0.359	0.934	0.713
3	Elliptical Winglet, Configuration 2 (60° angle)	0.17	0.386	0.930	0.729
		0.21	0.394	0.934	0.815
		0.25	0.416	1.018	0.885
4	Circular Winglet, Configuration 1 (0° angle)	0.17	0.407	0.852	0.563
		0.21	0.429	0.908	0.7150
		0.25	0.430	0.967	0.775
5	Circular Winglet, Configuration 2 (60° angle)	0.17	0.436	0.939	0.775
		0.21	0.451	0.957	0.737
		0.25	0.487	0.985	0.823

Table 5: Drag coefficients experimental data

S. No.	Winglet Configuration	Reynolds Number [10 ⁶]	Drag coefficient, C _D		
			Initial Angle of Attack [0°]	Transition Angle of Attack [4°]	Final Angle of Attack [14°]
1	Without Winglet	0.17	0.085	0.104	0.249
		0.21	0.083	0.100	0.275
		0.25	0.065	0.085	0.211
2	Elliptical Winglet, Configuration 1 (0° angle)	0.17	0.053	0.058	0.136
		0.21	0.050	0.056	0.140
		0.25	0.049	0.053	0.128
3	Elliptical Winglet, Configuration 2 (60° angle)	0.17	0.070	0.078	0.166
		0.21	0.058	0.065	0.153
		0.25	0.047	0.060	0.134
4	Circular Winglet, Configuration 1 (0° angle)	0.17	0.057	0.063	0.186
		0.21	0.053	0.057	0.154
		0.25	0.052	0.055	0.130
5	Circular Winglet, Configuration 2 (60° angle)	0.17	0.075	0.092	0.192
		0.21	0.063	0.083	0.172
		0.25	0.050	0.069	0.158

Table 6: Lift/Drag Ratio experimental data

S. No.	Winglet Configuration	Reynolds Number [10 ⁶]	Lift/Drag ratio [L/D]			
			Initial Angle of Attack [0°]	Transition Angle of Attack [4°]	Transition Angle of Attack [6°]	Final Angle of Attack [14°]
1	Without Winglet	0.17	2.8	5.7	5.7	2.6
		0.21	3.1	6.1	5.9	2.1
		0.25	4.7	7.71	7.0	3.5
2	Elliptical Winglet, Configuration 1 (0° angle)	0.17	5.61	11.27	11.09	4.73
		0.21	6.53	12.30	11.84	5.02
		0.25	7.33	13.73	13.19	5.55
3	Elliptical Winglet, Configuration 2 (60° angle)	0.17	5.5	8.8	9.3	4.4
		0.21	6.7	10.8	11.4	5.3
		0.25	8.8	13.0	13.5	6.6
4	Circular Winglet, Configuration 1 (0° angle)	0.17	7.18	10.51	10.2	3.02
		0.21	8.02	11.96	11.6	4.65
		0.25	8.29	13.57	12.9	5.98
5	Circular Winglet, Configuration 2 (60° angle)	0.17	5.8	8.5	9.1	4.0
		0.21	7.1	9.5	10.1	4.3
		0.25	9.6	11.8	12.2	5.2

Table 7: Lift curve slopes data

S. No.	Free stream velocity [m/s]	Reynolds Number [10 ⁶]	Lift curve slopes				
			Without Winglet	Elliptical Winglet at [0°]	Elliptical Winglet at [60°]	Circular Winglet at [0°]	Circular Winglet at [60°]
1	21.36	0.17	3.72	3.83	3.85	3.77	3.76
2	26.76	0.21	4.01	4.09	4.13	4.03	3.96
3	32.15	0.25	4.11	4.15	4.36	3.93	3.67

The relationship between signal readings, L_i and the loads, F_i applied on the calibration rig are given by the following matrix equation, the detailed procedure of calibration is explained elsewhere [18-19]

$$\{L_{ij}\} = [K_{ij}] \{F_{ij}\} \quad (2)$$

Where $[K_{ij}]$ is the coefficient matrix, $\{L_i\}$ is the signal matrix, $\{F_i\}$ is the load matrix.

The calibration matrix is obtained by finding the inverse of K_{ij} , coefficient matrix and it compares well (2% error) with the calibration matrix data supplied by the manufacturer with six component external balance [19].

2.5. Verification of Wind Tunnel Measurements with Sphere

The force measurements, using a sphere model, were carried out in $1m \times 1m$ low speed open wind tunnel described in the previous section. Figure 7 shows the photograph of a sphere mounted through the strut over the platform of the six-component balance placed in the wind tunnel section. The tests were conducted for free-stream velocities of 5.16 m/s, 10.56 m/s, 15.96 m/s, and 21.36 m/s, respectively (Table 8).



Figure 7: Sphere model mounted in wind tunnel test section

Table 8: Experimental data with sphere

S. No.	Free stream velocity [m/s]	Reynolds number	Drag Force [N]	Drag Coefficient	
				Experimental Experiment	Experimental (Schlichting [20])
1	5.16	3.3×10^4	0.051	0.404	0.400
2	10.56	6.8×10^4	0.23	0.436	0.480
3	15.96	1.0×10^5	0.45	0.374	0.430
4	21.36	1.4×10^5	0.66	0.306	0.410

For each free stream conditions drag force was obtained using a computerized data acquisition system and coefficient of drag (Table 8) is calculated using the Eq. (3) [20] given below,

$$C_D = \frac{D}{\frac{1}{2} \rho_\infty V_\infty^2 S} \quad (3)$$

Where D is the drag force, ρ_∞ is the air density, V_∞ is the free stream velocity, and S is the frontal area of sphere

defined by $S = \frac{\pi d^2}{4}$, where d is the nominal diameter of the sphere.

The coefficient of drag for a sphere as a function of the Reynolds number obtained from the book [21] is given in Table 8. The drag coefficient characteristics for a sphere, as reported in [21], are presented with the drag coefficients under the test as a function of the Reynolds number in Figure 8. From the graph, it is observed that C_D variations are qualitatively similar; both with a decrease in C_D near a critical Reynolds number of 3×10^5 , coinciding with natural transition from laminar to turbulent flow. For the reference data of sphere, C_D is about 0.4 in the Reynolds number range below the critical value and drops to about 0.1 for Reynolds numbers above the critical value. When the critical Reynolds number (i.e., the boundary layer separation) is exceeded, transition takes place on the front face, the boundary layer around the sphere becomes turbulent and the coefficient of drag is significantly reduced as the separation point on the boundary layers moves back [22]. This experiment verifies the measurements in wind tunnel compared with the data as reported in [21].

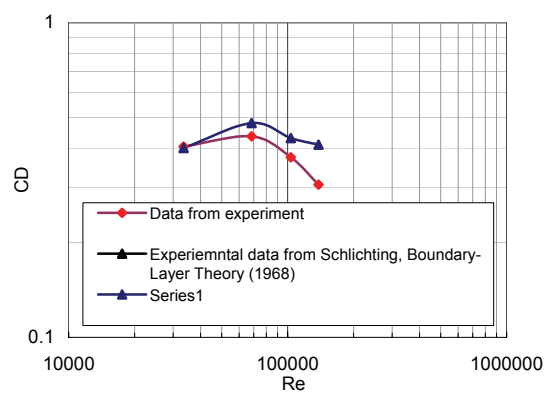


Figure 8: Drag coefficient versus Reynolds number for the sphere model

3. Results and Discussions

Wind-tunnel measurements using the aircraft model without winglet and with winglet of different configurations as configuration 1 (Winglet inclination at 0°), and configuration 2 (Winglet inclination at 60°) were done at Reynolds numbers 0.17×10^6 , 0.21×10^6 and 0.25×10^6 . The coefficient of lift and coefficient of drag are calculated from the experimental results as per the procedure explained in [18-19].

3.1. Lift Coefficient Characteristics

The coefficient of lift versus angle of attack for the aircraft model with and without winglet studied in the present investigation are shown in Figure 9 for the maximum Reynolds number of 0.25×10^6 . From Figure 9, it is observed that the lift increases with increase in angle of attack to a maximum value and thereby decreases with further increase in angle of attack. The initial values of lift coefficient occur at zero angle of attack and the maximum

values of the lift coefficient occur at an angle of attack of 8 degrees. Above this angle of attack, lift curve begins to decrease with further increase in angle of attack. The reason for a drop in lift coefficient beyond 8-degree angle of attack is probably due to the flow separation, which occurs over the wing surface instead of having a streamlined laminar flow there. The stalling angle happens to be approximately 8^0 for all the Reynolds numbers under the present study. The least square fit lines are drawn through the data obtained for different configurations until angle of attack of 8^0 and the lift curve slopes, $\frac{dC_L}{d\alpha}$ are found as 4.11, 4.15, 4.36, 3.93, and 3.67 respectively. It is observed that the $\frac{dC_L}{d\alpha}$ slope for all the configuration is

practically same with only a marginally high slope, a_0 for elliptical winglet of configuration 1 and 2 as compared to the circular winglet and without winglet configuration. The other details of the lift coefficients are given in Table 4.

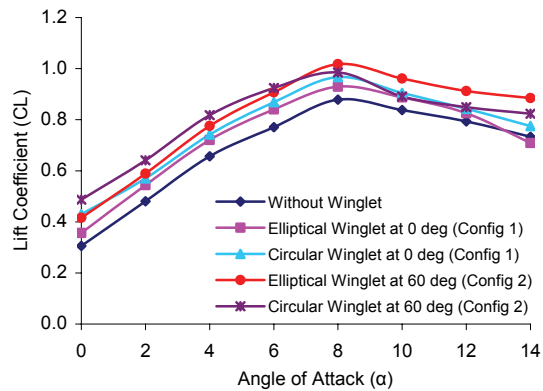


Figure 9: Lift Coefficients for the Aircraft Model

3.2. Drag Coefficient Characteristics

From Figure 10, it is observed that the drag coefficient for the aircraft model measured under all the configurations under this study shows an increasing trend with angle of attack for a Reynolds number 0.25×10^6 . The drag increases slowly with increase in angle of attack to a certain value and then it increases rapidly with further increase in angle of attack. The rapid increase in drag coefficient, which occurs at higher values of angle of attack, is probably due to the increasing region of separated flow over the wing surface, which creates a large pressure drag. From Figure 10 it is observed that the values of the minimum drag coefficients are 0.065, 0.049, 0.047, 0.052, and 0.050 respectively for different configurations for the maximum Reynolds number of 0.25×10^6 that occur at zero angle of attack. In particular, the measured drag against the angle of attack is minimum for the elliptical winglet of configuration 1 and 2 over the values of the range of angle of attack considered under this study. The measured drag values for the aircraft model with circular winglet of configuration 1 are also practically same as compared to the elliptical winglet. To establish the superiority of the elliptical winglet over the circular winglet experiments that are more detailed are required.

The other details of the drag coefficients are given in Table 5.

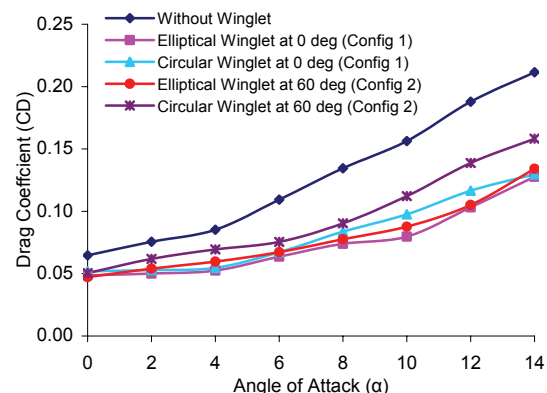


Figure 10: Drag Coefficients for the Aircraft model

3.3. Lift/Drag Ratio Characteristics

The lift/drag ratio is the outcome of the observations made in the two preceding sections. It is observed from Figure 11 that the lift/drag ratio for all the configurations considered increases with an angle of attack to its maximum value and thereby it decreases with further increase in angle of attack for a Reynolds number 0.25×10^6 . In particular, it is observed that the maximum lift/drag ratio for all the configurations considered in the study falls in the range of 4 to 6 degrees of angle of attack. The aircraft model without winglet gives a measured lift/drag ratio of 7.71 whereas the respective values of the lift/drag ratio for the different configurations are 13.73, 13.0, 13.57, and 11.77 respectively at an angle of attack of 4^0 . The lift/drag ratio values for the angle of attack of 6^0 are 7.0, 13.19, 13.48, 12.90, and 12.25 respectively for the different configurations. Practically it is observed that the lift/drag ratio versus angle of attack curve gives similar results for 4 to 8 degrees, for the elliptical winglet of configuration 1, elliptical winglet of configuration 2, and for circular winglet of configuration 1. The other details of the lift/drag ratio at other angle of attacks are given in Table 6 considered in the study.

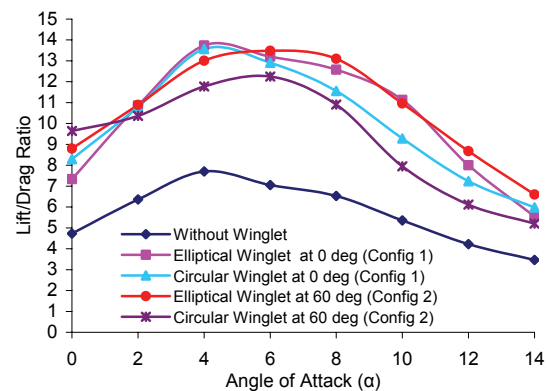


Figure 11: Lift/Drag Ratio for the Aircraft model

From Figure 9 and 10, it is observed that the lift curve slope increases with the addition of the winglet (Winglets

inclination at 60^0 and 0^0) ranging from 1% to 6% (Table 7) and at the same time the drag decreases for the addition of winglet ranging from 20% to 28% at the maximum Reynolds number of 0.25×10^6 . These experimental results can be explained by comparing with the results obtained at the Georgia Institute of Technology [16]. The tests were run in three configurations: winglets off (Configuration 0), winglets installed at zero degrees (Configuration 1), and winglets deployed at $+20^0$, $+10^0$, 0^0 , -10^0 , -20^0 (Configuration 2). They showed that flat plate winglets set at zero degrees (Configuration 1) increased lift curve slope by 10% for the maximum Reynolds number of 0.29×10^6 . They also showed that configuration 2 provided the largest increase of lift curve slope, ranging from 15% to 22% increases.

From this investigation it is observed that at the maximum Reynolds number of 0.25×10^6 elliptical winglet of configuration 1 and 2 (Figure 9) provides the largest increase of lift curve slope, ranging from 1% to 6% increases and at the same time drag decreases more for these two configurations ranging from 24.6% to 28% decrease, giving an edge over other configurations as far as

L/D for the elliptical winglet of configuration 1 and 2 (Figure 11) is considered. Decisively it can be said that the elliptical winglet of configuration 2 (Winglets inclination at 60^0) has the better performance giving about 6% increase of lift curve slope as compared to other configurations and it is giving the better lift/drag ratio (13.5). Full results of the studies on lift coefficient, drag coefficient and lift/drag ratio can be found in Reference [18].

4. Conclusions

Following are the conclusions drawn from this investigation. The calibration matrix obtained through the interaction matrix method compares well with the matrix data as supplied by the manufacturers of the six-component balance. Aerodynamic characteristics for the aircraft model with and without winglet having NACA wing No. 65-3-218 have been presented. Elliptical winglet at 60-degree incidence has the better performance giving about 6% increase in lift curve slope and thereby produces more lift and at the same time the drag decreases by 28% as compared to other configurations and it is giving the best lift/drag ratio for the maximum Reynolds number considered in the present study.

Acknowledgements

The authors are grateful for the support provided by grants from the IRPA (Project No: 09-02-04-0446-EA001), and the Aerodynamics Laboratory of Aerospace Engineering Department of the University Putra Malaysia for using the Wind Tunnel.

References

- [1] Bento, S.de, M.; Antonini P. Macedo and Dural H. da Silva F. "Considerations about Winglet Design". AIAA Paper 2003-3502.
- [2] Whitcomb, R. T. "A Design Approach and Selected Wind-Tunnel Results at High Subsonic Speeds for Wing-Tip Mounted Winglets". NASA TN D-8260, 1976.
- [3] Whitcomb, R. T. "Methods for Reducing Aerodynamic Drag". NASA Conference Publication 2211, Proceedings of Dryden Symposium, Edwards, California, 1981.
- [4] Yates, J. E., and C. Donaldson. "Fundamental Study of Drag and an Assessment of Conventional Drag-Due-To-Lift Reduction Devices". NASA Contract Rep 4004, 1986.
- [5] Louis, B. Gratzer. "Spiroid-Tipped Wing". U. S. Patent 5, 102068, 1992.
- [6] Reginald, V. French. "Vortex Reducing Wing Tip". U. S. Patent 4, 108403, 1978.
- [7] Clark, J. Aviation Partners, Inc., personal communication, 1999.
- [8] Jones, R. T. "Improving the Efficiency of Smaller Transport Aircraft". 14th Congress of the International Council of the Aeronautical Sciences, proceeding, Vol. 1, Toulouse, France, 1984.
- [9] Chandrasekharan, Reuben M., Murphy, William R., Taverna, Frank P., and Boppe, Charles W. "Computational Aerodynamic Design of the Gulfstream IV Wing". AIAA-85-0427, 1985.
- [10] Maughmer, M. D., S. S. Timothy., and S. M. Willits. "The Design and Testing of a Winglet Airfoil for Low-Speed Aircraft". AIAA Paper 2001-2478, 2001.
- [11] Spillman, J. J. "The use of wing tip sails to reduce vortex drag". Aeronautical Journal, Vol. 16, 1978, 387-395
- [12] Spillman, J. J., Ratcliffe, H. Y., and McVitie, A. "Flight experiments to evaluate the effect of wing-tip sails on fuel consumption and handling characteristics". Aeronautical Journal, Vol. 17, 1979, 279-281.
- [13] Spillman, J. J., and Fell, M. J. "The effects of wing tip devices on (a) the performance of the Bae Jetstream (b) the far-field wake of a Paris Aircraft". Paper 31A, AGARD CP No. 342, Aerodynamics of Vortical Type Flows in Three Dimensions, April, 1983 , 31A-1-11
- [14] Heinz G. Klug. "Auxiliary Wing Tips for an Aircraft". U. S. Patent 4722499, February 1988.
- [15] Vance A.T. "Gliding Birds: Reduction of Induced Drag by Wing Tip Slots between the Primary Feathers". Journal of Experimental Biology, Vol. 180, No.1, 1993, 285-310
- [16] Smith, M. J., N. Komérah, R. Ames., O. Wong., and J. Pearson. "Performance Analysis of a Wing with Multiple Winglets". AIAA Paper-2001-2407, 2001.
- [17] Roche La. U., and Palffy S., "WING-GRID, a Novel Device for Reduction of Induced Drag on Wings," Proceedings of ICAS 96, Sorrento, 1996.
- [18] Hossain, A. "Investigations of Longitudinal Aerodynamic Characteristics of Aircraft Model with and without Winglet". M.Sc. Thesis, Department of Aerospace Engineering, Faculty of Engineering, Universiti Putra Malaysia, UPM Serdang, Selangor DE, Malaysia, 2005.
- [19] Prithvi, R. A., A. Hossain, A. A. Jaafar, P. Edi, T. S. Younis, and M. Saleem. "Drag Reduction in Aircraft Model using Elliptical Winglet". Journal of IEM, Malaysia, Vol. 66, No. 4, 2005, 1-8.
- [20] Bertin, John. J., Aerodynamics for Engineers, Prentice-Hall, Inc, New Jersey, USA, 2002.
- [21] Schlichting, H. Boundary Layer Theory, McGraw-Hill Book Company, New York, USA, 1968.
- [22] Anderson, John. D, Introduction to Flight, McGraw-Hill Book Company, New York, USA, 2005.

Prediction of Friction Stir Welding Characteristic Using Neural Network

Y. K. Yousif^a*, K. M. Daws^b, B. I. Kazem^b

^aDepartment of Mechatronics Engineering, Baghdad University, Baghdad, Iraq
^bDepartment of Mechanical Engineering, Baghdad University, Baghdad, Iraq

Abstract

An artificial neural network (ANN) model was developed for the analysis and simulation of the correlation between the friction stir welding (FSW) parameters of aluminum (Al) plates and mechanical properties. The input parameters of the model consist of weld speed (Ws) and tool rotation speed (Rs). The outputs of the ANN model include property parameters namely: tensile strength, yield strength and elongation. Good performance of the ANN model was achieved. The model can be used to calculate mechanical properties of welded Al plates as functions of weld speed and Rs. The combined influence of weld speed and Rs on the mechanical properties of welded Al plates was simulated. Simulated annealing technique was used to prevent the network from getting stuck in local minima. A comparison was made between measured and calculated data. The calculated results were in good agreement with measured data.

© 2008 Jordan Journal of Mechanical and Industrial Engineering. All rights reserved

Keywords: Friction stir welding; Mechanical properties; ANN; Modeling;

1. Introduction

Recently, because of aluminum's light weight, it has been considered an energy-saving structural material in advanced applications. In addition, aluminum is an easily saved resource because it can be recycled, and thus can be expected to be an environmental friendly metallic material. One such application would be use in automobiles, which would facilitate transportation; numerous similar examples could be cited in support of employing aluminum as a structural material. Friction stir welding (FSW) was developed initially for aluminum alloys, by the welding institute (TWI) of United Kingdom [1]. Friction stir welding (FSW) is a relatively new method invented by The Welding Institute (TWI) in 1991. FSW is actually a solid-state joining process that is a combination of extruding and forging and is not a true welding process. Since the process occurs at a temperature below the melting point of the work piece material, FSW has several advantages over fusion welding. Some of the process advantages are given in the following list [2]:

1. FSW is energy efficient
2. FSW requires minimal, if any, consumables.
3. FSW produces desirable microstructures in the weld and heat-affected zones

4. FSW is environmentally "friendly" (no fumes, noise, or sparks)
5. FSW can successfully join materials that are "unweldable" by fusion welding methods.
6. FSW produces less distortion than fusion welding techniques.

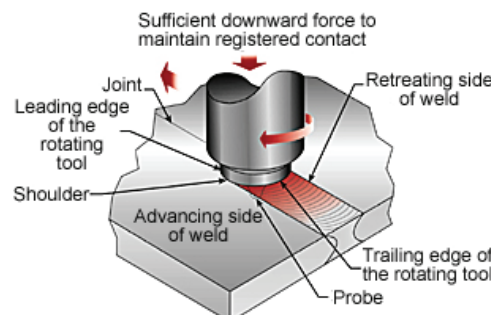


Figure (1) Schematic diagram of the FSW process

There are many research related to an applications of Artificial Intelligence (AI), especially Artificial Neural Networks (ANN) for engineering fields such as manufacturing processes prediction, monitoring and controlling. A. Bezazi , S. Gareth et al. (2006) [3]. An ANN model was developed to estimate fatigue lifetime of a sandwich composite material structure subjected to cyclic three-point bending loads. A total of 27 samples (three different loading levels for nine samples each) were

* Corresponding author. e-mail: yousifky@gmail.com

investigated to provide training and testing data for a series of multi-layer perceptron ANNs.

P. Dutta and D. K. Pratihar (2007) [4]. Conventional regression analysis was carried out on some experimental data of a tungsten inert gas (TIG) welding process, to find its input output relationships. One thousand training data for NNs were created at random, by varying the input variables within their respective ranges and the responses were calculated for each combination of input variables by using the response equations obtained through the above conventional regression analysis. Friction stir welding uses a cylindrical, shouldered tool with a profiled pin that is rotated and slowly plunged into the joint line between two pieces of sheet or plate material, which are butted together. Frictional heat is generated between the wear resistant welding tool and the work piece. This heat causes the work piece material to soften without reaching the melting point and allows the tool to traverse the weld line. As it does, the plasticized material is transferred from the leading edge of the tool to the trailing edge of the tool shoulder and pin. It leaves a solid phase bond between the two work pieces as shown in figure 1. [5]

In the field of biology, electronics, computer science mathematics and engineering, ANN is one of the most important research areas. ANN is a complicated system composed of numerous nerve cells. It is also a new type of computer system which is based on the primary understanding of the organization, structure, function and mechanism of the human brain. With the help of rapid progress in computers and material science, material design can now be carried out based on the knowledge and experience of the fabricated materials [6–7].

2. Experimental Work

Table 1 : The chemical composition of aluminum alloy

Element	Percentage	Element	Percentage
Al	-	Si	0.35%
Zn	4.2%	Cu	0.2%
Mg	1.26%	Zr	0.05%
Mn	0.09%	Ti	0.05%
Fe	0.22%	Cr	0.05%

The chemical composition of the material was given in table 1. Two hot rolled aluminum plates were clamped with a vice so that they would not be separated during welding process. A rotating tool which has a diameter of 20 mm was used.

Table (2) Measured data used as data sets

set No.	σ_t	NN Response	σ_b	NN Response	Elo. %	NN Response
1	78	77.973054	290.04	289.946098	2.4	2.3912949
2	248	248.010246	454.64	454.633699	5.64	5.6404608
3	281.88	281.865578	322.77	322.527211	9.2	9.1897045
4	336.96	336.936103	583.61	583.331025	22	21.987097
5	320	319.96774	322.7	322.630815	11.6	11.59386
6	320	320.011411	502.44	502.380949	11.6	11.598177
8	297.61	297.614452	345.4	345.537933	15.85	15.850173
9	189.48	189.480733	394.73	394.725282	4.34	4.3399821
10	246.25	246.250232	308.38	308.371768	11.07	11.06998

Plunged depth of the rotating tool was 2 mm. A schematic representation of the welding instrument is given in Fig. 1. Welding was carried out by rotating the tool at 710, 900 and 1400 rpm and by moving the plates at 70,40 and 140 mm/min. By using the predetermined welding parameters, different samples were welded for mechanical tests and metallographic examinations. For the tensile tests, FSW specimens were cut by using a slow speed diamond wheel saw through the transverse direction of the bonding interface of 5, 25, 72 mm³. Tensile strength and bending stress were measured to check the mechanical performance of the welding (Table 2). measured to check the mechanical performance of the welding (Table 2). Welded samples were characterized by means of tensile strength, hardness and elongation.. It is known that increasing the welding speed and decreasing the rotational speed of the tool reduces the heat input. Thus, increase in welding speed also increases the tensile strength while increasing Rs decreases the tensile strength. Tensile test gives an information about the elongation of the FSW samples. Here, again the amount of heat input plays an important role on the elongation properties of the FSW samples. The more heat input is the more elongation of the FSW samples. The sample welded with the 1400 rpm of the tool and 70 mm/min showed the largest elongation while the sample welded with the 710 rpm of the tool and 70 mm/min yielded the minimum elongation.

Welding with the fastest speed and slowest rotational speed gave a planar bonding surface while welding with lowest welding speed and fastest rotational speed of the tool gave well distinguished undulated joining edges of the plates.

3. Methodology of ANN Application and Modeling Data with Network

Since most manufacturing processes are complex in nature, highly non- linear and there are a large number of input variables, there is no close mathematical model which can describe the behavior of these processes. Artificial neural networks because they are cost - effective, easy to understand and because of their ability to learn from examples, have found many applications in process modeling for monitoring and control purposes, as intelligent sensors, to estimate variable that usually cannot be measured on - line, in dynamic system identification, in fault detection and diagnosis and, finally, in process control [8].

ANNs are computational models, which replicate the function of a biological network, composed of neurons and are used to solve complex functions in various applications. The system has four layers, which are input, two hidden and output layers. The input layer consists of all the input factors. Information from the input layer is then processed in the course of two hidden layers, following output vector is computed in the final (output) layer. Neural networks consist of simple synchronous processing elements that are inspired by the biological nerve systems. The basic unit in the ANN is the neuron. Neurons are connected to each other by links known as synapses; associated with each synapse there is a weight factor. Details on the neural network modeling approach are given in elsewhere [9,10]. In this work, the neural network model was trained using two different training algorithms:

1. Gradient Descent with Momentum Algorithm.
2. Levenberg - Marquardt Algorithm.

The performances of these two training algorithms are compared to decide which algorithm performs better than the other. The neural network may converge to a local minimum rather than a global one. Therefore, some sort of simulated annealing technique is used to find the best solution among many local minima [11]. The **simulated annealing** technique is as follows: once the network converges to a local minimum, the network state is perturbed in a random direction and by a random magnitude. Then the network dynamics are reactivated, and another local minimum is found. During this process, the algorithm keeps track of the best solution. After a predetermined number of local minima are found, the algorithm terminates and the solution with the lowest error is accepted as the best solution. The simulated annealing technique is used to capture the best solution (weights and biases) among several local minima. Thus, training algorithm is performed

five times for each network architecture, each time with different random initial weights and biases. After examining the performance of different architectures, a network with two hidden layers (include 3 neurons in the first and 6 in the second) trained by Levenberg Marquardt algorithm showed good performance indication. while figure (2) shows the resulted network architecture. Thus, the network architecture consists of two input neurons, 9 hidden neurons with nonlinear activation function.

(logarithmical sigmoid) and single output neuron with linear activation function. Tables (4,5 and 6) shows the trained network weights and biases. It is worth to note that the network training and simulation was performed on 2.8 GHZ, Pentium 4 PC using the MATLAB platform version 7 neural network toolbox.

4. Neural Network Simulation

Testing of neural network model required new independent (test sets) to validate the generalization capability of network. Table (3) shows testing data sets for the network and the response of the network to these data sets. The prediction accuracy for the testing patterns based on mean absolute percent error (APE) criteria [10]:

$$APE = \frac{|Predicted - Actual|}{Actual} * 100\%$$

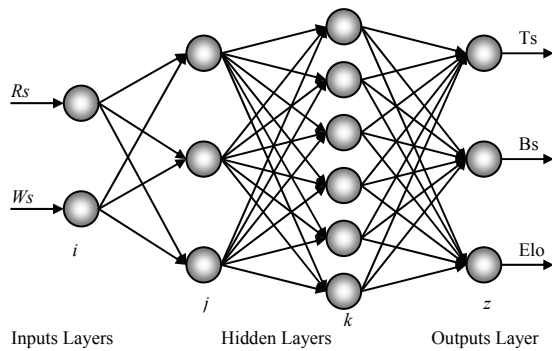


Fig (2) neural network architecture for FSW

Table (3) Test data sets and network response

Set No.	σ_t	NN Response	σ_b	NN Response	Elo. %	NN Response
3	330	327.125	389.8	373.634	8	6.87832
7	320	328.427	450.2	402.442	11.6	10.4471

The corresponding table above the mean error of:

- The Error of the Tensile Stress 1.7524 %.
- The Error of the Bending Stress 7.3777 %.
- The Error of the Elongation 11.98 %.

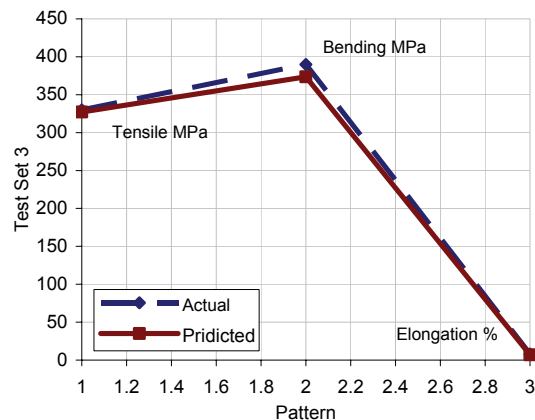


Figure (3) Predicted and measured data in test set 3

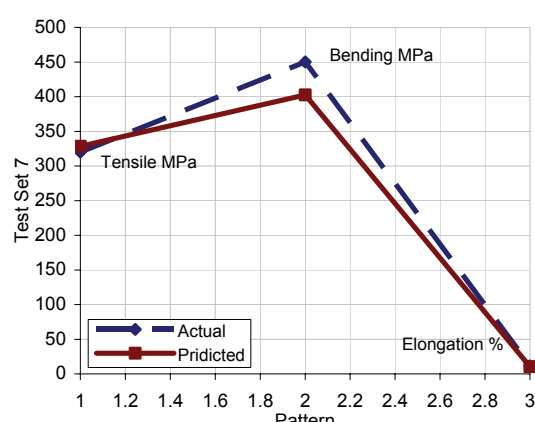


Figure (4) Predicted and measured data in test set 7

5. Evaluation of Results

Figures (3) and (4) show the measured and predicted output values were close to each other. In all the cases of the present work, feed-forward artificial neural networks were used. In present work, the following steps were developed:

1. Database collection.
2. Analysis and pre-processing of the data.
3. Training of the neural network.
4. Test of the trained network.
5. Postprocessing of data.
6. Use of the trained NN for simulation and prediction.

It's sufficient to take Rs and the welding speed to predict the mechanical properties such as tensile strength, bending stress and elongation of the bonded Al metal. In present study, Rs and the welding speed were used in the input layer and the tensile strength, bending stress and elongation were used in output. The transfer function log sigmoid used in this study is given by:

$$Y_i = \frac{1}{1+e^{-X_i}}$$

Where X_i is the input of the neuron in hidden layer and Y_i is the output of neuron while calculating X_i , Rs and Ws values must be normalize in rang [-1, 1] corresponding to the minimum and maximum of the actual values.

Table (4) Weights and bias between input layer and first hidden layer

i	1		2	b ₁
j	w ₁	w ₂		
1	-4.133123671	-5.808140227		2.940544626
2	16.46260301	-11.33170622		-3.74267169
3	-6.151224848	7.846399395		0.18585865

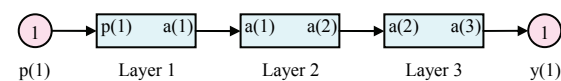


Figure (5) Three layers of neural network (predictor model)

Table (5) Weights and bias between first and second in hidden layer

j	1	2	3	b ₂
k	w ₃	w ₄	w ₅	
1	-14.735	5.86886	-4.4835	3.28278
2	-5.5828	-7.8937	-2.8578	8.20656
3	-5.5647	-16.739	-9.4099	12.5084
4	0.50508	-0.6692	-12.961	4.71296
5	-0.4468	8.57969	-14.071	2.45288
6	-4.7725	8.02553	3.35714	-5.4787

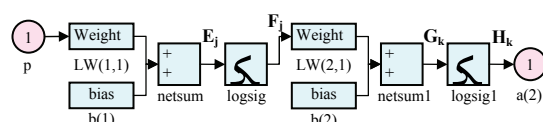


Figure (6) Two hidden layers simulation

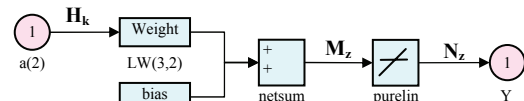


Figure (7) Output layer simulation

$$G_k = w_{k_3} * F_1 + w_{k_4} * F_2 + w_{k_5} * F_3 + b_{k_1}$$

where

$$k = 1, 2, 3, 4, 5, 6$$

$$H_k = \frac{1}{1+e^{-(G_1+G_2+G_3+G_4+G_5+G_6)}}$$

Table (6) Weights and bias between second hidden layer and outputs

k z	Weights						Bias
	1	2	3	4	5	6	b3
1	-1.9641	0.0739	0.6339	-5.9474	6.18	1.694	0.2263
2	4.04	-9.5196	7.3865	-13.046	9.1743	-5.8381	3.78
3	-2.3636	-5.8093	4.8388	-7.7474	6.2868	2.4715	1.5288

Then the final result of network (mechanical properties) are:

Tensile strength =

$$H_1 * w_{11} + H_2 * w_{12} + H_3 * w_{13} + H_4 * w_{14} + H_5 * w_{15} + H_6 * w_{16} + b_{13}$$

Bending Stress =

$$H_1 * w_{21} + H_2 * w_{22} + H_3 * w_{23} + H_4 * w_{24} + H_5 * w_{25} + H_6 * w_{26} + b_{23}$$

Elongation % =

$$H_1 * w_{31} + H_2 * w_{32} + H_3 * w_{33} + H_4 * w_{34} + H_5 * w_{35} + H_6 * w_{36} + b_{33}$$

And must transform the result value to real value by Post processing.

6. Conclusion

The aim of this paper was to show the possibility of the use of neural networks for the calculation of the mechanical properties of welded Al plates using FSW method. Results showed that, the networks can be used as an alternative way in these systems. For the proposed NN model the Levenberg – Marquardt algorithm shows better performance than gradient descent with momentum because it use 2nd order Taylor series approximation of performance index rather than 1St order approximation as with gradient descent algorithm. It is found that the correlations between the measured and predicted values of tensile strength, bending stress were better than those of elongation.

References

- [1] Tomotake Hirata et al."Influence of friction stir welding parameters on grain size and formability in 5083 aluminum alloy" Graduate School of Engineering, Osaka Prefecture University, 2006.
- [2] Nicholas, ED, "Developments in the friction stir welding of metals". ICAA-6: 6th International Conference on Aluminum Alloys, Japan, 1998.
- [3] Bezazi , S. Gareth et al." Fatigue life prediction of sandwich composite materials under flexural tests using a Bayesian trained artificial neural network" International Journal of Fatigue, Vol. 29, 2007, 738–747.
- [4] P. Dutta and D. K. Pratihar " Modeling of TIG welding process using conventional regression analysis and neural network-based approaches", Journal of Materials Processing Technology, Department of Mechanical Engineering, Indian Institute of Technology, Vol. 184, 2007, 56-68.
- [5] M. Abbasi Gharacheh, A.H. Kokabi, G.H. Daneshi, B. Shalchi, R. Sarrafi "The influence of the ratio of "rotational speed/traverse speed" (o/v) on Mechanical properties of AZ31 friction stir welds" International Journal of Machine Tools & Manufacture, Vol. 46, 2006,
- [6] Zeng Qingfeng, Zu Jiakui, Zhang Litong, Dai Guanzhong Mater, Vol. 23, 2002, 287–290.
- [7] Marmey P, Porte' MC, Baquey C. Nucl Instrum Meth Phys Res Sect B: Beam Interact Mater Atoms, Vol. 208, 2003, 429–433.
- [8] Hang and Chen," neural network based tool breakage monitoring system for end milling", Journal of Industrial Technology, Vol.16, No.2, 2000.
- [9] Massie DD. ECOS 2001. In: Gogus YA, Ozturk A, editors. First International Conference on Applied Thermodynamics, Istanbul, Turkey, 2001.
- [10] Malinov S, Sha W, McKeown JJ, "Modelling the correlation between processing parameters and properties in Titanium alloys using artificial neural network", Computational Materials Science, Vol. 21, 2001, 375-394.
- [11] Tania Binos "Evolving Neural Network Architecture and Weights Using An Evolutionary Algorithm" MSc Thesis, Department of Computer Science, RMIT University, Australia, 2003.
- [12] R. Azouzi and M. Guillot "On-line optimization of the turning process using an inverse process neurocontroller", Journal of Manufacturing Science and Engineering, Vol. 120, 1998, 101-108.

Mathematical Modeling for Pump Controlled System of Hydraulic Drive Unit of Single Bucket Excavator Digging Mechanism

Juma Yousuf Alaydi *

Industrial Eng. Dept., IUG, Palestine

Abstract

Industrial robots have turned out to be an everyday occurrence for engineers during the last twenty years. Increasing efficiency is one of the hottest research topics in hydraulic system. The comparison between two types of hydraulic control systems, which are the valve, controlled system and the pump-controlled system is essential area of researching. Hydraulic actuator with pump-controlled system is equipped in high power mining excavators and forestry equipment in order to increase efficiency. The purpose of this paper is to build a mathematical model for a hydraulic actuator with pump-controlled system. The boom of single bucket excavator is modeled and simulated as an example. The scheme of this system is presented and itemized. The model of these items is simulated and the control circuits are presented as well as the simulation results.

© 2008 Jordan Journal of Mechanical and Industrial Engineering. All rights reserved

Keywords: Hydraulic system; Pump controlled system; Valve controlled system; hydraulic drive unit; single bucket excavator; mathematical modeling; and simulation;

1. Introduction

Hydraulic actuation devices may be linear or rotary and are usually referred to as pistons or motors, respectively. A pump or a valve giving four basic hydraulic power elements and two basic over-all systems may control these two actuation devices: pump controlled and valve controlled. Such hydraulic power elements is simply a combination the of principal power device in all hydraulic systems [1].

The pump-controlled system consists of a variable delivery pump supplying fluid to an actuation device. The fluid flow is controlled by the stroke of the pump to vary output speed and the pressure generated matches the load. It is usually difficult to closely couple the pump to the actuator and this causes large contained volumes and slow response [2].

The valve-controlled system consists of a servo valve controlling the flow from a hydraulic power supply to an actuation device. The hydraulic power supply is usually a constant pressure type (as opposed to constant flow) and there are two basic configurations. One consists of a constant delivery pump with a relief valve to regulate pressure whereas the other is much more efficient because

it uses a variable delivery pump with a stroke control to regulate pressure.

The features of each system tend to complement the other so that application requirements would dictate the choice to be made. Generally, there is not a cost advantage to either because the need for a replenishing arrangement and a stroke servo for the pump controlled system offset the costly servo valve and heat exchangers required for the valve controlled system. However the faster response capability of valve controlled systems both to valve and load inputs makes this arrangement preferred in the majority of applications in spite of its lower theoretical maximum operation efficiency of 67% in low power applications where the inefficiency is comparatively less important, use of valve controlled system is nearly universal. Applications, which require large horsepower for control purposes usually, do not require fast response so that a pump-controlled system is preferred because of its superior theoretical maximum operating efficiency of 100% [3].

The pump-controlled actuator represents a further alternative. A simplified structure is depicted in Figure 1. This actuator uses a servo pump as a final control element in the actuator closed loop control. Similar to the classical circuit of a hydrostatic transmission, a closed hydraulic circuit design is employed for the realization of a four-

* Corresponding author. e-mail: jalaydi@mail.iugaza.edu

quadrant operation. This makes the utilization of brake energy in case of aiding loads generally possible. The pump controller adjusts the pump displacement according to the demanded volumetric flow, which depends on the actuator velocity. The pressure difference between the high pressure and the low-pressure line is automatically given by the actuator load. Mostly, the low pressure is set constant with the help of an external pump, which can also be employed for the supply of the pump control system. Thereby the hydraulic output power of the pump is simultaneously adapted to the required mechanical output power of the actuator. Due to its simple design characterized by small number of parts, and excellent achievable dynamic performance, the swash plate of the axial piston pump would be usually the best choice for the servo pump [4].

The application of the displacement control principle for actuators of heavy-duty mobile manipulators has the following three important advantages:

- The improved utilization of primary energy due to the omitted valves,
- The possibility of the additional use of brake energy in case of aiding loads,
- The reduction of total system weight due to the replacement of one or two large pumps by a number of smaller pumps [5].

The realization of pump control is uncomplicated for rotary actuators and linear actuators with double rod cylinders. Several industrial applications have been developed recently. The kinematics and the whole machine design of mobile manipulators require very often the use of differential cylinders. The unequal areas of the differential cylinder have to be compensated, if the differential cylinder may run within a pump-controlled actuator in a closed hydraulic circuit as shown in Figure 1B. The closed hydraulic circuit permits the four-quadrant operation of the pump-controlled actuator. Different circuit solutions allowing the compensation of the unequal cylinder areas were developed recently. The first solution shown in Figure 1A was developed by Lodewyks at the University of Aachen in 1993. A hydraulic transformer (5) serves as a flow compensator. The servo pump (2) has been used as a final control element in the closed loop position control of the linear actuator. The second solution is shown in Figure 1B characterized by two variable displacement pump units (1, 2) for one cylinder. This concept requires a multi-variable control concept for the simultaneous pressure and position control of the actuator to guarantee the required flow compensation.

A third solution showed that in Figure 1C represents an enlargement of the solution with two servo pumps. The circuit is supplemented by a third variable displacement pump (3) and a proportional pressure valve allowing the adjustment of the pressure level. This solution requires a high number of components but does not need a multi-variable control concept. These actuator solutions were developed for special industrial applications. For the majority of applications in mobile machines, the replacement of a valve controlled actuator by a displacement-controlled actuator, which requires two and more variable displacement pumps and perhaps even further elements, which increase the cost [4].

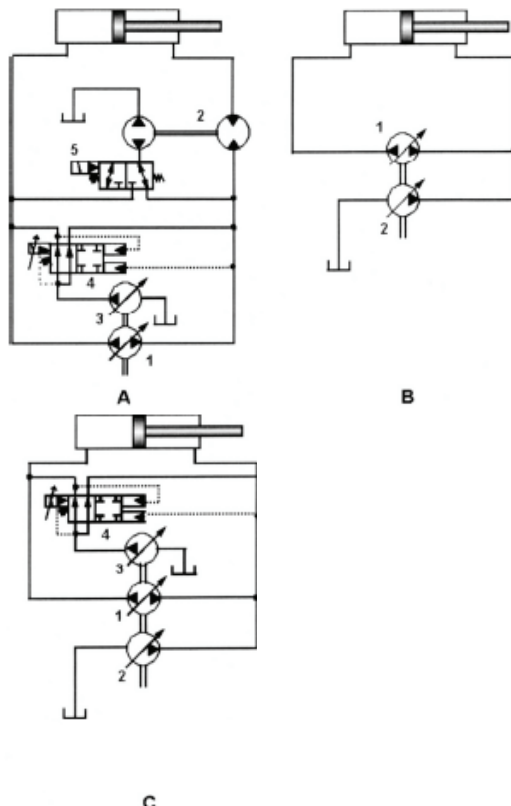


Figure 1. Circuit solutions for pump controlled actuator with differential cylinder

The purpose of this paper is to build a mathematical model for a hydraulic actuator with pump-controlled system. The scheme of this system is presented and itemized. Models of items and simulation of control circuits are also presented as well as the result of the simulation

2. Hydraulic Drive Unit of Single Bucket Excavator Digging Mechanism

Kinematics and hydraulic circuit diagram of the hydraulic excavator digging mechanism is shown in Figure 2 and Figure 3. The hydraulic excavator digging mechanism consists of four links, boom 'S', connecting element 'V', stick 'R', and bucket 'K'; each is set in motion by its own hydraulic cylinder. A variable displacement pump controls the velocity of the piston rod of the cylinder.

After investigating the load of each cylinder, it was shown that the boom cylinder is carrying the highest load [1]. Each element has its own mass, which in turn has its own reaction on the boom

cylinder. Kinematics of digging mechanism and structure design show that the reaction of the mass of each digging element changes with the stroke of boom cylinder. As shown in Figure 2, it is clear that any change in the mechanism element position will result in substantial changes in the position of the mass center consequently this will cause changes in inertia and the equivalent mass as well as the total contained oil volume.

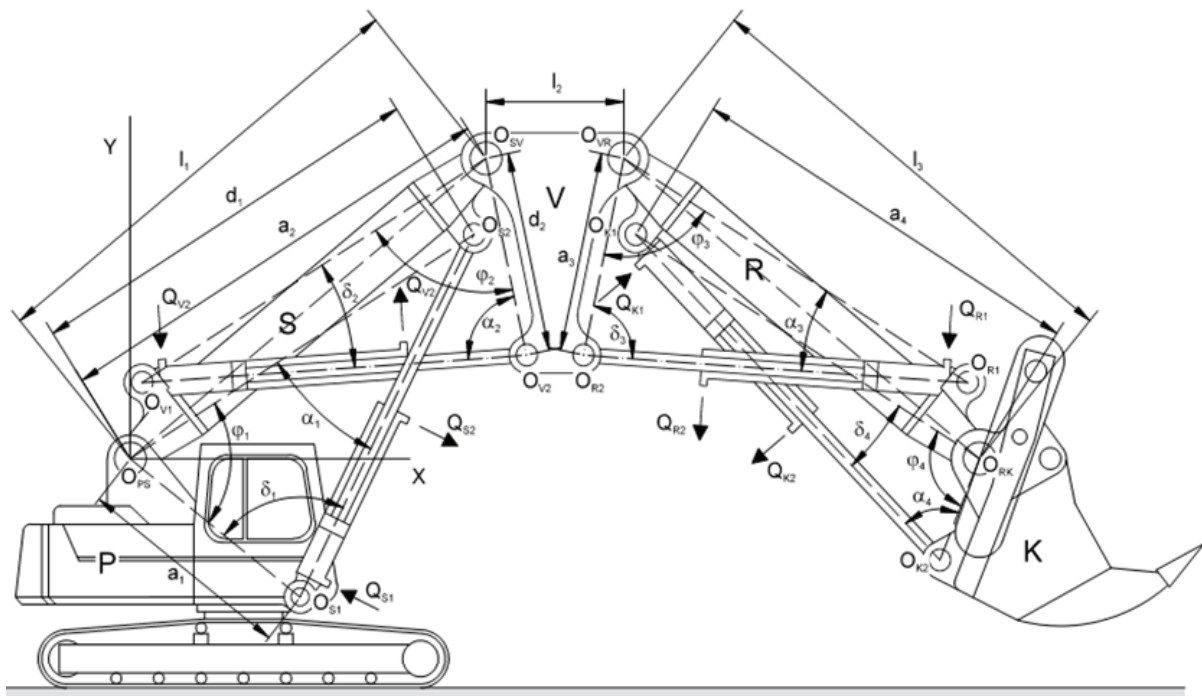


Figure 2 Excavator Digging Mechanism, (Boom S, Connecting element V, Stick R, and Bucket K) [1].

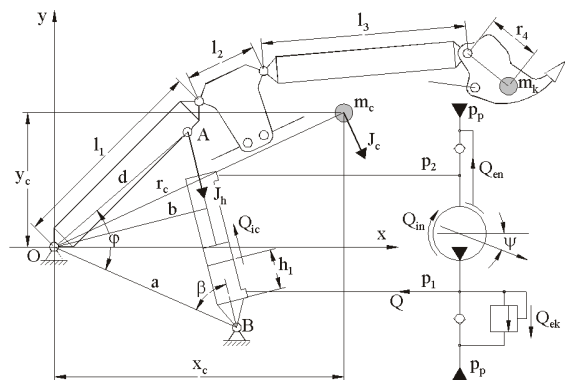


Figure 3. Hydraulic Unit and cinematic circuit diagram of the boom mechanism

Thus, this system is characterized by variable parameters depending on the elements position. The control system with dynamic characteristics requires designing a control algorithm structure (dynamic controller), which must be efficient to compensate the dynamic variation of the controlled object parameters.

The following assumptions were made during this paper:

The friction force at the hinges and the seals are neglected. The link of each mechanism is considered as a rigid body. The return pressure is constant and equal the replenishing pressure $P_2=0$.

The parameters changing range of the boom mechanism can be computed from its mathematical model. The mathematical model of the boom hydraulic cylinder is set up for forward stroke movement since digging process and consequently the highest load occurs during forward stroke.

3. Mathematical Modeling of the Hydraulic Drive Unit with Pump Controlled System

Mathematical model describes in details the boom hydro cylinder forward stroke and displays all-important characteristics of the investigated object. The schematic diagram of the model is shown in Figure 4.

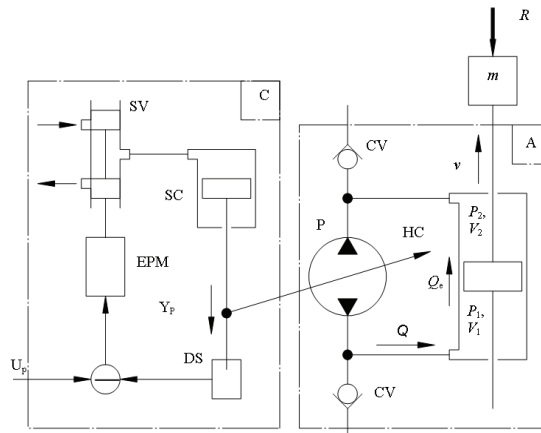


Figure 4. Model of the hydraulic actuator with pump controlled system

The model incorporates:

- Control object cylinder HC and speed sensor SS to measure the rod speed. The cylinder is loaded by active force R (h) and mass m (h), since these parameters are a function of the cylinder stroke position h.
- Power supply unit, which is represented by the variable displacement, pump P.

- c) Servo valve unit, which converts input signal ' U_p ' and feedback signal from sensor displacement sensor 'DS' into a control signal ' Y_p '.

3.1. Model Description

The model consists of Electro hydraulic Servo valve 'C' to control the flow of variable displacement pump 'P'. An input signal ' U_p ' is activated by the excavator operator which enters the amplifier 'EPM', and then the servo valve spool starts to move. Oil enters into the servo valve hydro cylinder piston chamber 'SC' forcing the rod, which is linked to the pump swash plate forward and thus changing the pump flow. The rod displacement ' Y_p ' will keep changing until the electric signal of displacement sensor 'DS' balances the control signal ' U_p '. Oil flow from the pump 'P' enters into the cylinder chamber, creating force enough to move the mass against external force 'R'. Check valves 'CV' prevent stagnation, compensate the shortage of the flow from the replenishing flow, and allow the excess flow to pass through the pressure relief valve to the tank.

3.2. Mathematical Modeling of the Actuator

Equation of movement

$$m(h) \frac{dv}{dt} = A \cdot P_1 - R \quad (1)$$

Continuity equation of the oil in the cylinders chambers

$$\frac{V_1}{E} \frac{dp_1}{dt} = k \cdot y_p - C_e \cdot P_1 - A \cdot v \quad (2)$$

Servo valve equation

$$T_p \frac{dy_p}{dt} + y_p = K_p \cdot U_p \quad (3)$$

Where: $m(h)$ is the mass as a function of the digging element position (h), v is the velocity of piston rod measured by speed sensor SS, A area of the piston, R external force, V_1 volume of hydro cylinder chamber, E oil bulk modulus, k pump coefficient (which can be computed experimentally from the relationship of the pump flow Q and the servo valve displacement Y_p), K_p controller coefficient (which can be computed experimentally from the relationship of the servo valve displacement Y_p and input signal U_p), t time.

Combining equations 1, 2, and 3, the mathematical model will have the following form:

$$m_{eq}(h) \frac{dv}{dt} = A_1 P_1 - A_2 P_2 - R(h) \quad (4)$$

$$\frac{V(h)}{E} \frac{dP_1}{dt} = k\psi - (C_e + C_i)(P_1 - P_2) - A_1 v, \quad (5)$$

Where: m_{eq} is the equivalent or the effective mass of the digging mechanism elements acting on the cylinder piston rod, kg.

Equivalent mass acting on hydro cylinder rod changes depending on digging mechanism element positions as shown in equation a below.

It is assumed that all digging mechanism elements are joint rigidly as one unit and rotating as solid body with mass m_c around axis through O. $m_c = m_1 + m_2 + m_3 + m_4$. $m_{eq}(h)$ can be computed from the kinematics and dynamics analysis of the system given in [1]. h is the vector of digging mechanism state position characterized by cylinder stroke, h_1 boom, h_2 insert, h_3 stick and h_4 bucket.

In addition, from [2] the equivalent mass will have the following relationship:

$$m_{eq}(\bar{h}) b \frac{d^2 h_1}{dt^2} = m_c r_c(\bar{h}) w_\tau, \quad (a)$$

Kinematics of Fig. 3 gives

$$b = \frac{a d \sin \varphi}{\sqrt{a^2 + d^2 - 2a d \cos \varphi}}, \quad (b)$$

$$\varphi = \arccos \frac{a^2 + d^2 - (h_{01} + h_1)^2}{2ad} \quad (c)$$

Then the angular acceleration can be computed as:

$$w_\tau = r_c \frac{d^2 \varphi}{dt^2} = \frac{2r_c(h_{01} + h_1)}{\sqrt{4a^2 d^2 - [a^2 + d^2 - (h_{01} + h_1)^2]^2}} \frac{d^2 h_1}{dt^2} \quad (e)$$

From equation (b), (c) and (e), it is possible to compute the maximum and minimum limits of equation (a) which can be rewritten as:

$$m_{eq} = \frac{a^2 + d^2 - 2a d \cos \varphi}{a^2 d^2 \sin^2 \varphi} \cdot r_c^2 m_c. \quad (d)$$

Where:

- r_c is the radius of rotation around hinge O,
- w_τ is the angular acceleration of the center of mass,
- m_c is the mass of the system.
- A_1, A_2 are the areas of forward and return stroke of the piston, m^2 .
- P_1, P_2 are the pressure at the piston and rod chambers, Pa.
- P_2 equals the replenishing pressure $P_2=0$ (assumed).
- k is the pump control element (swash plate) gain coefficient $m^3/rad/deg$.
- v is the piston rod velocity, m/s.
- V is the total contained volume including the chambers and the connecting hoses and manifolds.
- E is the liquid bulk modulus of elasticity (constant).
- ψ is the swash plate parameter ($0 \leq \psi \leq 1$).
- C_e, C_i is the lumped external and internal leakage coefficients respectively.
- h_{01} distance from cylinder hinge B to the piston return stroke position.

Equations 4 and 5 can be Lap laced and written in the general form as:

$$\left(\frac{m_{eq}(\bar{h})V(h_1)}{EA_1^2}s^2 + \frac{m_{eq}(\bar{h})(C_e + C_i)}{A_1^2}s + 1 \right) \cdot \delta v = k \cdot \delta \psi \quad (6)$$

Where: δ deviation from steady state value, s Laplace operator.

The dynamic behavior of this second order system can be then described in terms of two parameters, T which is the characteristic time, and ξ which is the damping ratio. The system characteristic equation can be rewritten to give:

$$\frac{m_{eq}(h)V(h_1)}{EA_1^2} = T^2 \quad (7)$$

$$\frac{m_{eq}(h)(C_e + C_i)}{A_1^2} = 2T\xi \quad (8)$$

4. Simulation Example.

The given analysis allows computing the important parameters of the controlled object at any digging mechanism position resulting from changing vector h .

All the data are collected from real mining excavator. The calculations were performed for the following real dimensions collected from 15-m³ single bucket excavator in [1].

Pump leakage coefficients were evaluated based on lab experiment from [1] as follow:

$$C_{ep}=2.24 \cdot 10^{-11} m^5/(N \cdot s); \quad C_{ip}=5.22 \cdot 10^{-11} m^5/(N \cdot s)$$

The following coefficients were collected from manufacturers catalogues for the boom cylinder and the pressure relief valve.

Relief valve external leakage coefficient $C_{er}=0.026 \cdot 10^{-11} m^5/(N \cdot s)$, no internal leakage coefficient was considered. Hydraulic cylinder internal leakage coefficient $C_{ic}=0.137 \cdot 10^{-11} m^5/(N \cdot s)$, no external leakage coefficient was considered.

The lumped leakage coefficients are:

Total external leakage coefficient $C_e=C_{ep}+C_{er}$; and Total internal leakage coefficient $C_i=C_{ip}+C_{ic}$. For MEXZ 4AP112M-5 mining excavator shown in Fig.1.

$l_1=l_3=6.5m; \quad l_2=1.9m; \quad r_4=1.4m; \quad a=3.0m; \quad d=5.54m;$
 $h_1=3.3m; \quad m_1=m_3=12.5 \cdot 10^3 kg; \quad m_2=8.5 \cdot 10^3 kg;$
 $m_4=40 \cdot 10^3 kg$ (mass bucket with full load);
 $A_1=2 \cdot 0.125 m^2; \quad E=1.2 \cdot 10^3 MPa;$

Simulation of the system of equations 6,7 and 8 for T and ξ were accomplished with step $\Delta h_1=0.1H$ for the boom digging mechanism element (H is the maximum stroke of the boom cylinder).

In Figure 5 the result of simulation of the pump controlled system which have been made for the given data from real mining excavator, the pump Hytos MLPD/G217D, the proportional valve Bosch NG6, the linear hydraulic actuator Mannesmann Rexroth CYW 160 B 63/45-120, volume of the pipe 0.002 m³ and the dynamical load described above.

Maximum and minimum values of T and their corresponding ξ , m_{eq} , V , were obtained as follows:

$$T_{max}=0.102; \quad \xi=0.015; \quad m_{eq}=1.25 \cdot 10^6; \quad V=0.628;$$

$$T_{min}=0.0066; \quad \xi=0.012; \quad m_{eq}=0.066 \cdot 10^6; \quad V=0.050;$$

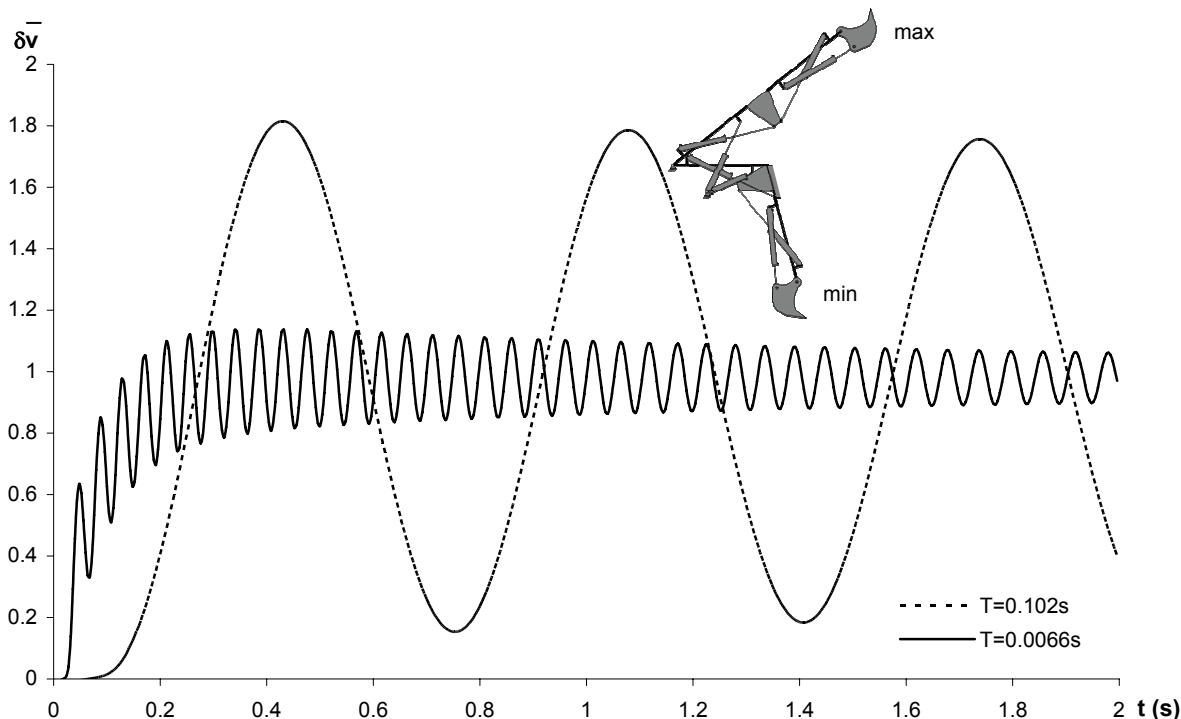


Figure (5) Transient response for hydraulic drive

5. Discussion And Conclusion

The transient response for two extreme boom positions in compliance with actuator mathematical model was resolved and analyzed to give the following results:

The digging mechanism load acting on the boom cylinder rod was changed from $0.32 \times 10^6 \text{ N}$ to $2.38 \times 10^6 \text{ N}$.

The value of the characteristic time of the linearized model of the control object was changed from $T_{\min} = 6.6 \times 10^{-3} \text{ s}$ to $T_{\max} = 102 \times 10^{-3} \text{ s}$.

The damping coefficient was also changed from $\xi_{\min} = 0.012$ to $\xi_{\max} = 0.015$.

The dynamic behavior of the load, the characteristic time, and the damping coefficient would greatly affect the transient process parameters thus, for each piston movement, a new transient process with different parameters would appear.

The digging mechanism and hydraulic unit mathematical model represents a dynamic system with variable parameters because the coefficients are determined by the digging mechanism position.

The simulation of the hydraulic actuator with pump controlled model shown in Fig.5 were obtained without correction for two extreme digging mechanism positions and it was clearly shown the weak damping of hydraulic unit resulted in sustained vibration.

The simulation of the model is employed to show that hydraulic actuator with open loop control system is not relevant for hydraulic unit with pump controlled system. It is necessary to construct a rational dynamic regulator to control the pump flow in order to stabilize the system.

The next step is to look for a suitable controller for the hydraulic drive digging mechanism to eliminate the vibration resulting from the weak damping.

References

- [1] Juma Y. Alaydi. 'Optimization of Pump Controlled System of Hydraulic Unit of Single Bucket Excavator Digging Mechanism'. PhD thesis Kharkov Polytechnic University, Kharkov Ukraine, 2000.
- [2] Gladky P.M., Alaydi J.Y. 'Application of hydraulic actuators with pump controlled system in hydraulic excavators'. Vestnic Journal of National Technology, University of Ukraine, Machine building, Kiev Polytechnic Institute, Kiev. Ukraine, 2000.100-103.
- [3] Herbert E. Merritt, 'Hydraulic Control Systems', J. Wiley, and Sons1967.
- [4] Backe W. Trends in Mobile Hydraulics, Fourth International Conference on Fluid Power, Temper, Finland, 1995.
- [5] Oshina M., 'The tendency of servo control for hydraulic excavator'. Fifth Scandinavian International Conference on Fluid Power, Linkoping, Sweden, 1997.

Experimental Investigation of Heat Transfer Enhancement in Radiating Pin Fin

Ganesh Murali J. ^a*^{*}, Subrahmanyam S. Katte ^b

^a Department of Automobile Engineering, K.L.N. College of Engineering, Pottapalayam - 630 611, India

^b School of Mechanical Engineering, Sastra University, Thanjavur - 613 402, India

Abstract

A literature review shows that much of work on radiating fins has been carried out analytically and numerically. Presently, a radiating pin fin with grooves and threads on its outside surface is investigated experimentally. A test facility with a vacuum chamber and instrumentation is fabricated. The heat input to the fin is varied such that the base temperature is maintained constant under steady state. Based on a study of effect of vacuum, using available resources, the chamber is designed for a vacuum of 80 mm Hg such that the contribution of convection to the total heat transfer could be ignored. The study shows that there exist optimum angle of grooves and number of threads per inch for which the heat loss per unit mass is a maximum. The grooved / threaded radiating fin loses 1.4 and 1.2 times greater heat per unit mass, respectively, compared to the bare pin fin.

© 2008 Jordan Journal of Mechanical and Industrial Engineering. All rights reserved

Keywords: Radiating fin; Cavity effect; Threaded fin; Effect of Vacuum; Optimization;

1. Introduction

Since radiation is the only possible mode of heat transfer in space, radiating fins are used in spacecraft for waste heat rejection. The radiating fin or a space radiator is generally optimized with respect to mass, since mass is at a premium on spacecraft.

A review of literature shows that various researchers have attempted to improve the design and provide the mass optimized space radiators. Wilkins [1] studied the problem of designing a thin fin which transfers a given rate of heat from a base at a temperature and which has the smallest mass. Sunil Kumar and Venkateshan [2] optimized tubular radiator with annular fins on a non-isothermal base. The presence of an optimum fin outer diameter for a given pipe diameter has been brought out. A set of useful correlations which will enable the designer to quickly evaluate the performance of the system is developed for different profiles. Krishnaprasas [3] presented mass optimized design of a straight rectangular plate fin array extending from a plane wall. Ramesh and Venkatesan [4] used a two dimensional finite difference method of analysis to observe the thermal performance characteristics of a tubular space radiator with attached fins. A wide range of thermal and geometrical parameters is considered for the analysis and a new dimensionless

heat dissipation parameter has been defined for the designer's usage. Krikis and Razelos [5] presented the correlations for optimum dimensions of longitudinal rectangular and triangular radiating fins with mutual irradiation. Chung, B. T. F.; Nguyen, L. D.,[6] analyzed various radiating spines to determine the general relationships for spine dimensions, the heat transfer characteristics and a least material profile under the optimum condition. Razani, A.; Zohoor, H. [7] studied a conducting-radiating spine with an arbitrary profile to find the optimum dimensions of the spine. Schnurr, N. M.; Townsend, M. A.; Shapiro, A. B. [8] optimized the radiating fin arrays with respect to weight. A non linear optimization approach was used to determine the minimum weight design for radiating fin arrays used in space applications. Black and Schoenhals [9], and Black [10] studied the directional radiation properties of specially prepared V groove cavities and also optimized the directional emission from V groove and rectangular cavities. Gorchakov and Panarin [11] & [12] obtained a numerical solution of the system of equations describing the thermal state of the fin. Schnurr, N. M [13] optimized the design of longitudinal and triangular radiating fins with respect to weight. Dhar, P. L.; Arora, C. P. [14] developed a method of carrying out the minimum weight design of finned surfaces of various types. Tanaka, S.; Kunitomo, T. [15] analyzed numerically the radioactive and convective heat transfer from longitudinal and rectangular fin array in

* Corresponding author. e-mail: ganeshmurali_973@yahoo.com

a plane surface by applying the Monte Carlo method. Optimization of the heat transfer performance of the finned plate system has been examined for various combinations of parameters. Karam, R. D.; Eby, R. J. [16] presented temperature optimized design of a rectangular fin under constant heat flux condition. Venkateshan, S. P.; Gopinath, Ashok,[17] studied the problem of a uniform area radiating fin for large values of the radiation conduction interaction parameter and developed for improving the previously known asymptotic solution to make it applicable for relatively smaller values of radiation conduction interaction parameter. Razani, A., Zohoor, H. [18] presented suitable methods for parametric studies and design analysis of optimum spines. Zaulichnyi, E. G [19] analyzed the problem of heat transfer by means of radiators with finned heat pipes with one-dimensional approximation and proposed an algorithm to design radiators of a specified capacity with constraints on their weight and dimension.

Love, T. J., Francis, J. E. [20] analyzed longitudinal radiating fins equally spaced around a cylindrical heat source. Eslinger, R. G.; Chung, B. T. F. [21] presented a finite element solution for the heat transfer from a radiating and convecting fin or fin arrays. Karam, R. D [22] presented a method, which optimizes the selection of linearization parameters to obtain a best approximate solution to radiation problems. Truong, H. V.; Mancuso, R. J[23] presented One-dimensional steady-state solutions for radiation from front and rear surfaces of an annular fin having different front and rear emissivities. Chang, H. V [24] developed a computer model of a heat pipe radiator based on two correlations for the rectangular radiating fin efficiency. Chung, B. T. F, Nguyen, L. G [25] presented a systematic study on optimum dimensions and the associated heat transfer characteristics for radiating longitudinal fins. Badari Narayana, K., Uma Kumari, S, Narayana Murthy, H. [26] presented an analysis to optimize both mass and area of radiating fin based on the design calculations with uniform heat flux applied to the fin. Torikoshi, K., Kawazoe, M., Fujiwara, M., Kurosaki, Y[27] studied theoretically and experimentally the Heat transfer augmentation due to surface radiation in an annulus with fins. Nguyen, H. T.; Lehtinen, A. M [28] analyzed numerically Conduction and radiation heat transfer between two stationary arrays of interleaving gray fins of rectangular profile are parametrically analyzed for a wide range of fin emissivity, dimensionless fin base temperatures, and pertinent dimensionless ratios relating the fin dimensions and fin material properties. Lee, Ron C. [29] presented an analytical treatment of radiation fin effects in cryogen systems. Bhise et al. [30] investigated a corrugated fin structure for space radiator applications and presented correlations for the optimum corrugation angle and maximum heat loss to space. Srinivasan and Katte [31] proposed a grooved radiator with higher heat loss per unit mass compared to the flat radiator. Deiveegan and Katte [32] Proposed a hollow conical radiating fin, which radiates 5 times greater heat per unit mass than the corresponding solid pin fin, and showed that an optimum angle, thickness and emissivity exist for mass optimized performance.

The review of literature shows that much of work on space radiators has been carried out analytically and

numerically. There have been a very few attempts to experimentally study the effect of modification of geometry of a radiating pin fin on its heat transfer characteristics. Presently, a radiating pin fin with threads and grooves on its outside surface are investigated experimentally. A test facility with a vacuum chamber and instrumentation is fabricated. The heat input to the fin is varied such that the base temperature is maintained constant under steady state. The study shows that there exist optimum angle of grooves and number of threads per inch for which the heat loss per unit mass is a maximum.

2. Experimental Setup and Procedure

A test facility, as shown in Fig. 1, consisting of a vacuum chamber, control panel and instrumentation for measuring the vacuum, temperature and heat supplied is fabricated. The low cost vacuum chamber of size 0.3×0.45 m is constructed using 4 mm thick GI sheet. One of the walls is made detachable such that the radiating fin to be tested could be changed easily. The radiating fin to be tested is fitted to this detachable wall. Four passages at the top and one passage at the bottom of the chamber are provided. Three passages at the top are used for the electrical and thermocouple connections. These three passages are sealed with epoxy resin compound, which is used to mold the broken underground electric cables. Fourth passage at the top is fitted with a valve for controlling the vacuum in the chamber. The passage at the bottom is used for sucking air from the chamber, using the suction line of an air compressor. A reciprocating compressor of capacity 10 kg/cm^2 is used to for this purpose. The interior surfaces of chamber as well as the radiating fin are painted with black-board paint.

A vacuum gauge is provided to measure the vacuum inside the chamber. The control panel consists of an ammeter, voltmeter, temperature indicator and a dimmer-stat to vary the input power supply to the heater. A heating element, operating through the dimmer-stat, is connected to one end of the pin fin. Ten K-type thermocouples are connected along the length of fin at equidistance. The vacuum chamber is designed for a maximum vacuum of 80 mm Hg such that the contribution of convective heat transfer to the total heat transfer could be ignored. This value is chosen based on a study of effect of vacuum on the total heat transfer by the fin.

The pin fin chosen in the present study is made of aluminum, with a length of 150 mm and a diameter of 19.05 mm. All experiments are carried out under steady state, for a root temperature of 40°C . The power input to the heater is controlled such that, the root of fin is maintained constant at the desired temperature, after attaining steady state, which is observed by the variation of temperatures with time.

3. Geometries of the Fin Used in the Experiment

The geometry, which is proposed in the present work, is shown in the Fig. : 2, 3, and 4. Threads and grooves are provided for the radiator surface, instead of the conventional flat surface.

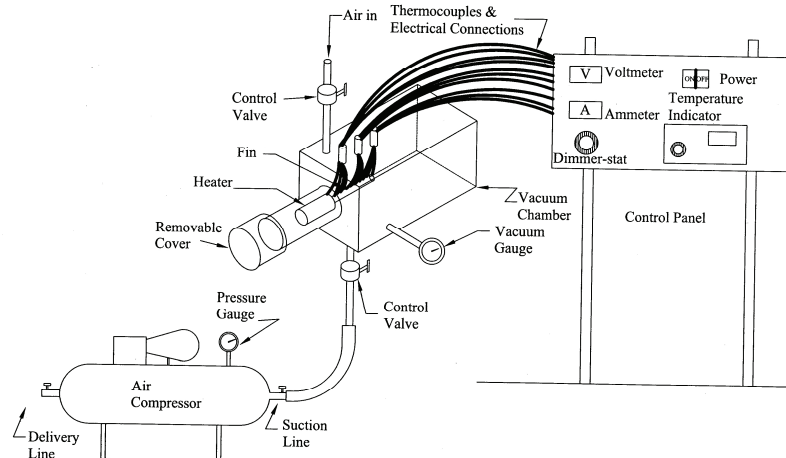


Fig. 1: schematic of experimental set up

Conduction of heat takes place along x direction. This geometry has applications in solar panels and fin-tube radiators. The proposed space radiator is supposed to be placed in between the bank of tubes carrying coolant.

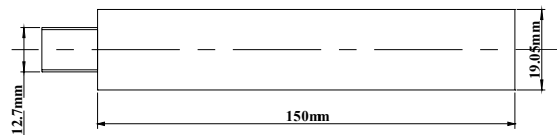


Fig.2: pin fin

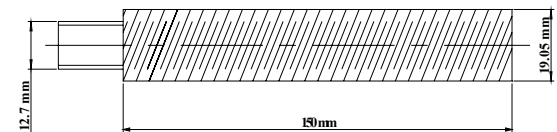


Fig.3: pin fin with threads

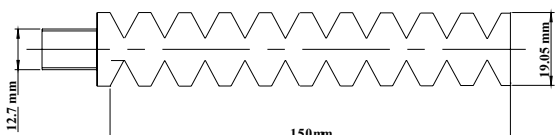


Fig.4: Pin Fin With "V" Grooves

4. Experimental Uncertainty

The current input, voltage, total heat supplied to the heater and surface temperature of the fin are four major parameters in this study. The uncertainty analysis for the derived quantities was carried out following the procedure given in the book *Experimental methods for Engineers* by Holman. The uncertainty of the Voltage measurement was estimated to be maximum 16.1%. The uncertainty in the measurement of current was found to be 2.33% max. The uncertainty in heat flow measurement was 16.1 %. The percentage of error associated with temperature measurement is 1% up to 70°C.

5. Results and Discussion

5.1. Effect of Vacuum on Heat Loss

The effect of vacuum on the total heat loss by the fin is studied first, in order to minimize the effect of convective heat transfer from the fin. Fig. 5 shows the effect of variation of absolute pressure on the total heat loss by the fin, which includes the effects of convective as well as radioactive losses. The vacuum in the chamber is controlled by adjusting the air flow into the chamber using the valve. For an absolute pressure of 0.2133 bars, the total heat loss is 4.4 W, which is 43.14 % of the total heat loss corresponding to the atmospheric pressure. For an absolute pressure of 0.1066 bars, the total heat loss is 3.78 W, which is 37.06 % of the total heat loss corresponding to the atmospheric pressure. For these two values of absolute pressures, the difference in the contributions of radiation to the total heat transfer is only about 6 %. Hence an absolute pressure of 0.1066 bar (80 mm Hg) is chosen as the chamber pressure for subsequent experiments.

5.2. Effect of Angle of "V" Threads

Heat transfer characteristics are studied for a radiating fin with "V" threads on its outside surface, having a depth of 1.3 mm. The effect of angle of threads on heat loss and heat loss per unit mass is shown in Fig. 6. For a given depth of threads, the surface area available for radiation decreases as the thread angle increases. However, the heat loss by radiation not only depends on the surface area, but also on the cavity effect. Hence, with increase in the thread angle, the heat loss and heat loss per unit mass vary non-monotonically. An optimum angle of threads for which the heat loss and heat loss per unit mass are high

For the chosen fin, the optimum thread angle is about 40°, and the threaded fin loses about 1.4 time's greater heat per unit mass than the corresponding pin fin. With further increase in the thread angle, the effect of decrease of surface area is dominant, and hence the heat loss does not vary significantly.

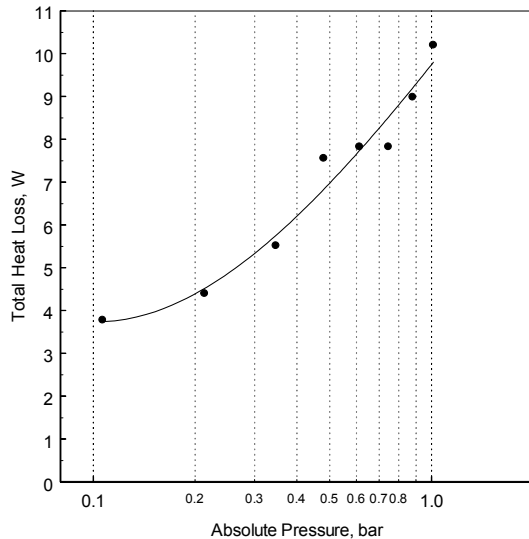


Fig. 5: effect of variation of vacuum on heat transfer

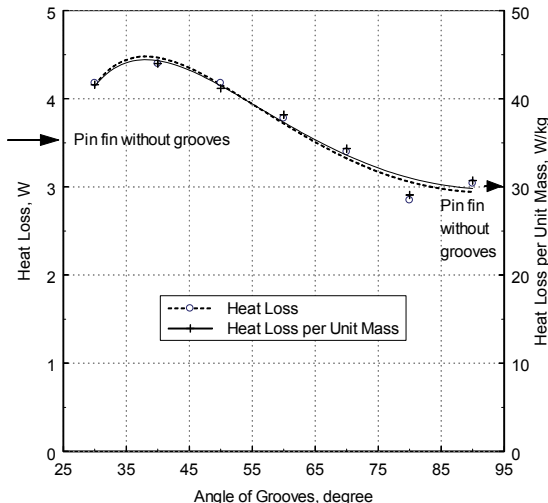


Fig. 6: effect of angle of grooves on heat transfer

When the thread angle is decreased from 90° to 40° , the heat loss or heat loss per unit mass increases by about 1.5 times, which is significant. Further, the provision of threads is beneficial if the angle of threads is less than 60° , because, if the thread angle is greater, the heat loss for the threaded fin would be less than the corresponding pin fin without threads. However, from heat loss per unit mass point of view, the threaded fin would be beneficial if the thread angle is less than 75° .

5.3. Effect of Threads Per Inch on Heat Loss

Finally, the heat transfer characteristics are studied for a radiating fin with standard metric "V" threads on its outside surface. The effect of number of threads per inch on heat loss and heat loss per unit mass is shown in Fig. 7. For a given number of threads per inch, there will be a corresponding depth of threads. Hence, as the number of threads per inch varies, the surface area available for radiation, the cross sectional area available for conduction of heat and the cavity effect would vary. Hence, with increase in the number of threads per inch, the heat loss and heat loss per unit mass vary non-monotonically.

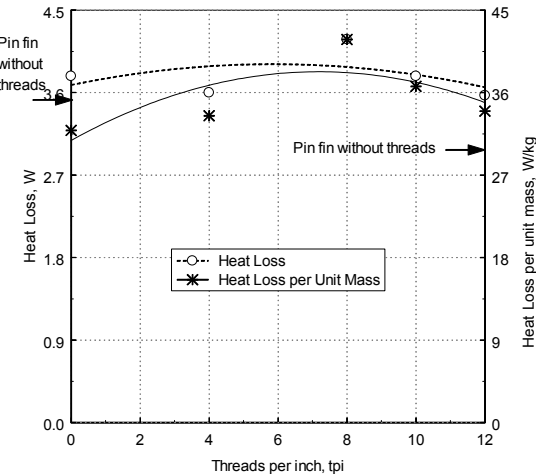


Fig. 7: effect of thread per inch

There exists an optimum number of threads per inch for which the heat loss or heat loss per unit mass are maximum. For the chosen fin, as seen from Fig. 7, the optimum number of threads per inch lies between 6 and 8. There exists a range of number of threads per inch for which the heat loss and heat loss per unit mass for the threaded fin are greater than those for the corresponding unthreaded pin fin. For the chosen fin, for the optimum number of threads per inch of eight, the threaded fin loses about 1.2 time's greater heat per unit mass than the corresponding pin fin. The heat loss per unit mass varies significantly with the number of threads per inch compared to the heat loss.

6. Conclusion

The effect of modification of surface geometry for a radiating pin fin has been investigated experimentally. A test facility consisting of a vacuum chamber, control panel and instrumentation for measuring the temperature, vacuum and heat supplied is fabricated. The vacuum chamber is designed for a maximum vacuum of 80 mm Hg such that the contribution of convective heat transfer to the total heat transfer could be ignored. For a given base temperature, the effect of vacuum, angle of grooves and number of threads per inch are studied. The study shows that there exist optimum angle of grooves and number of threads per inch for which the heat loss per unit mass is a maximum. Corresponding to the optimum groove angle and number of threads per inch, the grooved / threaded fin loses 1.2 to 1.4 time's greater heat per unit mass compared to the radiating pin fin.

References

- [1] Wilkins J.E., Jr., "Minimizing the Mass of Thin Radiating Fins", *J. Aerospace Science*, Vol. 27, 1960, 145-146.
- [2] S. Sunil Kumar and S.P.Venkateshan, "Optimized Tubular Radiator with Annular Fins on a Non-Isothermal Base", *Int. J. Heat and Fluid Flow*, Vol.15, 399-409, 1994.
- [3] Krishnaprasas C. K., "Optimum Design of Radiating Rectangular Plate Fin Array Extending From a Plane Wall", *J. Heat Transfer*, Vol. 118, 490-493, 1996.

- [4] Ramesh N. and S. P. Venkateshan, "Optimum Finned Tubular Space Radiator", Heat Transfer Engineering, Vol. 18, 69-87, 1997.
- [5] Krikis R.N. and Panagiotis Razelos, "Optimum Design of Spacecraft Radiators with Longitudinal Rectangular and Triangular Fins", J. Heat Transfer, Vol.124, 805-811, 2002.
- [6] Chung, B. T. F.; Nguyen, L. D., "Thermal analysis and optimum design for radiating spine of various geometries, Heat transfer science and technology"; Proceedings of the International Symposium, Beijing, People's Republic of China, Oct. 15-18, 1985 (A87-33101 13-34). Washington, DC, Hemisphere Publishing Corp., 510-517, 1987.
- [7] Razani, A.; Zohoor, H. , "The optimum dimensions of radioactive spines", Proceedings of Space 90, the Second International Conference, Albuquerque, NM, Apr. 22-26, 1990. Vol. 2 (A91-27576 10-12). New York, American Society of Civil Engineers, p. 1316-1325, 1990.
- [8] Schnurr, N. M.; Townsend, M. A.; Shapiro, A. B., "Optimization of radiating fin arrays with respect to weight", ASME, Transactions, Series C - Journal of Heat Transfer, Vol. 98, 1976, 643-648.
- [9] Black W.Z. and Schoenhals R.J., "A Study of Directional Radiation Properties Specially Prepared 'V'-Groove Cavities", J. Heat Transfer, Vol. 90, 1968, 420-428.
- [10] Black W.Z., "Optimization of the Directional Emission from V-Groove and Rectangular Cavities", J. Heat Transfer, Vol. 95, 1973, 31-36.
- [11] Gorchakov V.S., and Panevin I.G., Effectiveness of Radiating Fins Covered with V shaped Grooves, <http://techreports.iarc.nasa.gov/egi-in/NTRS>, 1975.
- [12] Gorchakov V.S., and Panevin I.G, "Efficiency of Radiating Fins Covered with V shaped Grooves", J.High temperature, Vol.13,No.4, 1976, 733-738.
- [13] Schnurr, N. M., "Radiation from an array of longitudinal fins of triangular profile", AIAA Journal, Vol. 13, 1975, 691-693.
- [14] Dhar, P. L.; Arora, C. P. "Optimum design of finned surfaces", Franklin Institute, Journal, Category: Fluid Mechanics and Heat Transfer, Vol. 301, 1976, 379-392.
- [15] Tanaka, S.; Kunitomo, T., "Numerical analysis of radioactive-convective heat transfer from an extended surface by the Monte Carlo method," JSME, Bulletin, Vol. 21, 1978, 258-265.
- [16] Karam, R. D.; Eby, R. J., "Linearized solution of conducting-radiating fins," AIAA Journal (Fluid Mechanics and Heat Transfer), Vol. 16, 1978, 536-538.
- [17] Venkateshan, S. P.; Gopinath, Ashok, "Asymptotic analysis of a uniform area radiating fin", Canadian Society for Mechanical Engineering, Transactions, Vol. 11, No. 2, 1978, 103-108.
- [18] Razani, A., Zohoor, H. "Optimum dimensions of convective-radioactive spines using a temperature correlated profile", Franklin Institute, Journal (ISSN 0016-0032) Category: Fluid Mechanics and Heat Transfer, Vol. 328, No. 4, 1991, 471-486.
- [19] Zauchnyi, E. G. "Possibilities for improving the characteristics of a radiator cooler through the use of finned heat pipes as radiating elements", Sibirskii Fiziko-Tekhnicheskii Zhurnal (ISSN 0869-1339) , Category: Fluid Mechanics and Heat Transfer, 1991, 20-26.
- [20] Love, T. J., Francis, J. E. "A linearized analysis for longitudinal fins with radioactive and convective exchange" Thermo physics and Heat Transfer Conference, Palo Alto, Calif., AIAA, 1978.
- [21] Eslinger, R. G.; Chung, B. T. F. "Periodic heat transfer in radiating and convecting fins or fin arrays", American Institute of Aeronautics and Astronautics and American Society of Mechanical Engineers, Thermo physics and Heat Transfer Conference, Palo Alto, Calif., AIAA ,1978.
- [22] Karam, R. D "Optimum solution of linearized radiation equations," Proceedings of the First International Conference , Swansea, Wales, 1979.
- [23] Truong, H. V.; Mancuso, R. J. "Performance predictions of radiating annular fins of various profile shapes", American Society of Mechanical Engineers and American Institute of Chemical Engineers, Joint National Heat Transfer Conference, Orlando, Fla., ASME 5, 1980.
- [24] Chang, H. V "Optimization of a heat pipe radiator design," Thermo physics Conference, Snowmass, CO, 1984.
- [25] Chung, B. T. F, Nguyen, L. G. "Optimization of design parameters for radiating longitudinal fins of various geometries", AIAA, Aerospace Sciences Meeting, Reno, NV, 1986.
- [26] Badari Narayana, K, Uma Kumari, S, Narayana Murthy, H., "Analysis of circular tapering radiator plates", Proceedings of the Eighth International Heat Transfer Conference, San Francisco, CA, Volume 2 (A87-30676 12-34). Washington, DC,1986.
- [27] Torikoshi, K, Kawazoe, M, Fujiwara, M, Kuroski, Y, "Heat transfer augmentation due to surface radioactive exchange effect of internal fins in an annulus, Proceedings of the Twenty-fourth National Heat Transfer Conference and Exhibition, Pittsburgh, PA, 1987
- [28] Nguyen, H. T.; Lehtinen, A. M, "Radiation and conduction between interleaving fins - Numerical and linearized solutions," AIAA, Aerospace Sciences Meeting, Reno, NV, 1988.
- [29] Lee, Ron C., "Radiation fin effects in cryogen systems." AIAA, Thermo Physics Conference, Buffalo, NY, 1989.
- [30] Navin V. Bhise, Subrahmanyam S. Katte and Venkateshan, S. P., A Numerical Study of Corrugated Structure For Space Radiators, 16th National and 5th ISHMT-ASME Heat and Mass Transfer Conference, Kolkotta, 2002.
- [31] Srinivasan, K., and Subrahmanyam S.Katte, Analysis of Grooved Space Radiator, 17th National and 6th ISHMT- ASME Heat and Mass Transfer Conference, Kalpakkam, India, 2004.
- [32] M. Deiveegan and Subrahmanyam S. Katte, "One Dimensional Analysis of Hollow Conical Radiating Fin", J. Thermo Physics and Heat Transfer, Vol. 18, 2004, 277-279.



الجامعة الهاشمية



المملكة الأردنية الهاشمية

المجلة الأردنية
للهندسة الميكانيكية والصناعية

JJMODE

مجلة علمية محكمة

<http://jjmie.hu.edu.jo/>

ISSN 1995-6665

المجلة الأردنية للهندسة الميكانيكية والصناعية

مجلة علمية عالمية محكمة

المجلة الأردنية للهندسة الميكانيكية والصناعية: مجلة علمية عالمية محكمة أستنها اللجنة العليا للبحث العلمي، وزارة التعليم العالي والبحث العلمي، الأردن، وتصدر عن عمادة البحث العلمي والدراسات العليا، الجامعة الهاشمية، الزرقاء، الأردن.

هيئة التحرير

رئيس التحرير

الأستاذ الدكتور موسى محسن

قسم الهندسة الميكانيكية، الجامعة الهاشمية، الزرقاء، الأردن.

الأعضاء

الأستاذ الدكتور أيمن المعايطه

الأستاذ الدكتور نسيم سواعد

الأستاذ الدكتور محمد النمر

الأستاذ الدكتور بلال العكش

الأستاذ الدكتور عدنان الكيلاني

الأستاذ الدكتور علي بدران

فريق الدعم

سكرتير التحرير

خالد الزيود

تنفيذ وإخراج

المهندس سلطان عمرو

المحرر اللغوي

الدكتورة زينب أبو سmek

ترسل البحث إلى العنوان التالي:

رئيس تحرير المجلة الأردنية للهندسة الميكانيكية والصناعية

عمادة البحث العلمي والدراسات العليا

جامعة الهاشمية

الزرقاء - الأردن

هاتف : 4147 3903333 فرع 00962 5

Email: jjmie@hu.edu.jo

Website: www.jjmie.hu.edu.jo